



Thèse de doctorat de l'Université Sorbonne Paris Cité

Préparée à l'Université Paris Diderot

Ecole doctorale STEP'UP - ED 560

Laboratoire Astroparticule et Cosmologie / Equipe de recherche Gravitation

Graphes d'ondelettes pour la recherche d'ondes
gravitationnelles: application aux binaires excentriques de
trous noirs

Wavelet graphs for the detection of gravitational waves:
application to eccentric binary black holes

Par Philippe Bacon

Thèse de Physique de l'Univers

dirigée par Éric Chassande-Mottin

Présentée et soutenue publiquement à Paris le

28 septembre 2018

devant un jury composé de :

Sylvain Chaty	Professeur, Université Paris Diderot	<i>Président du jury</i>
Didier Verkindt	Chargé de recherche, Université de Haute-Savoie	<i>Rapporteur</i>
Ik Siong Heng	Professeur, Université de Glasgow	<i>Rapporteur</i>
Archana Pai	Assistant professeur, IIT Bombay	<i>Examineur</i>
Marta Volonteri	Directrice de recherche, IAP	<i>Examineur</i>
Danièle Steer	Professeur, Université Paris Diderot	<i>Invitée</i>
Éric Chassande-Mottin	Directeur de recherche, Université Paris Diderot	<i>Directeur de thèse</i>

Contents

Acronyms	4
Acknowledgements	6
Abstract	7
Résumé	8
Introduction	13
1 Gravitational wave theory	15
1.1 Linearised theory of general relativity	15
1.2 Lorenz gauge	17
1.3 Solution in vacuum and transverse-traceless gauge	17
1.4 The multipole expansion	18
1.5 Energy radiated by gravitational wave sources	20
2 Astrophysical sources of gravitational waves	21
2.1 Gravitational wave and multi-messenger astronomy today	21
2.1.1 Gravitational wave detections	21
2.1.2 The era of Multi-messenger astronomy	23
2.2 An overview about compact objects	24
2.2.1 Stellar evolution in brief	24
2.2.2 Formation of compact objects	27
2.2.3 How do compact binaries form ?	29
2.2.4 GW emission from compact object binaries	32
2.3 Gravitational waves from eccentric binaries	33
2.3.1 Formation channels	34
2.3.2 GW emission from eccentric binaries	35
3 Gravitational wave interferometric detectors	39
3.1 Basics of interferometry and main noise contributions	39
3.1.1 Laser interferometry in a nutshell	39
3.1.2 Limiting noises	41
3.2 Network of detectors	41
3.2.1 On the importance of detector networks	41
3.2.2 Second generation detectors	43
4 Gravitational wave transient searches	45
4.1 Searches for continuous GW sources	45
4.1.1 Continuous waves	45
4.1.2 Stochastic GW background	46
4.2 Searches for GW transient sources	47
4.2.1 Known signal model: matched filtering	47
4.2.2 Unmodeled signals: generic transient searches	51
4.2.3 Event significance	57
4.2.4 Limitations of current searches	58

5	Wavegraph	59
5.1	Computation of time-frequency patterns	59
5.1.1	Stationary phase approximation	59
5.1.2	Sparse time-frequency representation and WDM transform	62
5.2	Graph computation	63
5.3	Search the observational data using the graph	65
5.4	Comparison study: Gaussian noise case	66
5.4.1	Time-frequency graphs	67
5.4.2	Simulated data sets	68
5.4.3	Results	68
5.5	Comparison study: real noise case	71
5.5.1	cWB gating and vetoes	72
5.5.2	A glitch rejection algorithm for Wavegraph	73
5.5.3	Running Wavegraph with consistency test in O1 data	75
6	Searching for eccentric black hole binaries with Wavegraph	78
6.1	Eccentric binary black hole signals	78
6.1.1	Approximant and time-frequency representation	78
6.1.2	Time-frequency graphs	79
6.2	Population model	81
6.3	Comparison study	83
6.3.1	Preliminary study	84
6.3.2	Results with the "fully eccentric" graph	87
7	Conclusion	93
7.1	Lesson learned and perspectives with Wavegraph	93
7.1.1	Lessons learned and possible improvements	93
7.1.2	Extensions and future prospects	94
7.2	The futures of gravitational wave experiments	95
	Appendix	98

Acronyms

LIGO Laser Interferometer Gravitational Wave Observatory. 32

LISA Laser Interferometer Space Antenna. 47

AGB *asymptotic giant branch*. 26

BBH *binary black hole*. 21

BH *black hole*. 28

BNS *binary neutron star*. 22

CT *consistency test*. 73

cWB *Coherent WaveBurst*. 45

cWB+WG *Coherent WaveBurst with Wavegraph*. 66

DPF dominant polarisation frame. 56

eBBH *eccentric binary black hole*. 33

EFE *Einstein field equation*. 15

EM electromagnetic. 23

FAR *false-alarm rate*. 57

GC globular cluster. 34

GCN Gamma-ray Coordinate Network. 23

GR *general relativity*. 15

GRB *gamma-ray burst*. 21

GW *gravitational wave*. 15

HMXB *high-mass X-ray binary*. 30

HR *Hertzsprung-Russel*. 24

MCMC *Markov Chain Monte Carlo*. 50

MLR maximum likelihood ratio. 56

MP *matching pursuit*. 62

MS *main sequence*. 24

NGC New General Catalogue of nebulae and clusters of stars. 23

NS	<i>neutron star.</i>	28
PP	<i>proton-proton.</i>	25
PSD	<i>power spectrum density.</i>	47
RLOF	<i>Roche lobe overflow.</i>	29
SASI	<i>standing accretion shock instability.</i>	94
SG	<i>Sine-Gaussian.</i>	59
SMBH	<i>supermassive black hole.</i>	34
SMBHB	<i>supermassive black hole binary.</i>	34
SNR	<i>signal to noise ratio.</i>	48
SPA	<i>stationary phase approximation.</i>	60
TF	<i>time-frequency.</i>	53
TT	<i>traceless-transverse.</i>	18
UMP	<i>updating matching pursuit.</i>	79
WDM	<i>Wilson-Daubechies-Meyer.</i>	52
WG	<i>Wavegraph.</i>	59
WR	<i>Wolf-Rayet.</i>	30

Acknowledgements

Je tiens tout d'abord à remercier Eric Chassande-Mottin pour m'avoir guidé pendant ces trois années de thèse. Ses conseils m'ont beaucoup apporté. A ses côtés, j'ai découvert le travail à l'échelle d'une collaboration et celui en équipe. Il a su me communiquer une rigueur de tous les instants dans mes recherches. Je lui en suis très reconnaissant.

Great thanks to Gayathri V. and Archana Pai for the friendly and fruitful exchange we had during our weekly teleconferences. It was a pleasure to visit the IISER-TVM institute and discover the Kerala.

I would like to express my deepest gratitude to the members of my jury and more specifically to Ik Siong Heng and Didier Verkindt for accepting to be the reviewers of this work. They played a major role in the improvements brought to this thesis.

Many thanks to the coherent WaveBurst team for their precious help in understanding the pipeline and running the analyses: Sergei Klimenko, Gabriele Vedovato and Shubhanshu Tiwari. A special thank to Francesco Salemi for its close collaboration to the Wavegraph project and its invitations to the Max Planck Albert Einstein Institute in Hanover.

Le présent travail a aussi été réalisé grâce au groupe Gravitation du laboratoire APC : Matteo Barsuglia, Stanislav Babak, Hubert Alloin et Antoine Petiteau. Je voudrais remercier plus spécialement Ed Porter pour sa patience et les échanges fructueux que nous avons eus sur des questions d'astrophysique.

Merci au personnel administratif de l'APC pour leur rapidité et leur efficacité malgré un contexte difficile: Vanessa Amoi, Francois Carré, Béatrice Silva et Ludovic Davila.

Un grand merci aux doctorants et post-doctorants du laboratoire avec qui j'ai eu l'occasion d'échanger et de passer de bon moments : Matteo Tacca, Eleonora Capocasa, Donatella Fiorucci, Yann Bouffanais, Agata Trovato, Marc Arène, Timothée Grégoire, Calum Murray, Marion Spir-Jacob and Dimitri Chuard. Leur soutien n'a pas été pour peu dans ma capacité à mener à bien ce travail de thèse. Merci et pardon à mes collègues de bureau que j'ai dérangé avec mes nombreuses questions : Ileyk El Mellah, Davide Poletti, Fangchen Feng, Dominic Beck et Clara Verges.

Merci aussi à Douglas Marshall, Julien Girard et Julien Derr pour les bons moments que nous avons passé à enseigner et discuter autour d'un bon café.

Enfin je tenais à remercier ma famille et mes proches pour leur présence au cours de ces trois années. C'est aussi auprès d'eux que je dois excuser mes trop longues absences. Ils ont été présents (eux) dans les moments les plus difficiles et je les en remercie chaleureusement. Merci Sophie pour ton soutien indéfectible et ta présence constante à mes côtés (...et merci aussi pour les figures !).

Abstract

In december 2015 the LIGO detectors have first detected a gravitational wave emitted by a pair of coalescing black holes 1.3 billion years ago. Many more observations have been realised since then and have heralded gravitational waves as a new messenger in astronomy. The latest detection is the merge of two neutron stars whose electromagnetic counterpart has been followed up by many observatories around the globe. These direct observations have been made possible by the developpement of advanced data analysis techniques. With them the weak gravitational wave inprint in detectors may be recovered. The realised work during this thesis aimed at developping an existing gravitational wave detection method which relies on minimal assumptions of the targeted signal. It more precisely consists in introducing an information on the gravitational wave signal phase depending on the astrophysical context. The first part is dedicated to a presentation of the method. The second one presents the results obtained when applying the method to the search of stellar mass binary black holes in simulated Gaussian noise data. The study is repeated in real instrumental data collected during the first run of LIGO. Finally, the third part presents the method applied in the search for eccentric binary black holes. Their orbit exhibits a deviation from the quasi-circular orbit case considered so far and thus complicates the signal morphology. This third analysis establishes first results with the proposed method in the case of a poorly modeled signal.

Mots-clés: *gravitational wave, binary black hole, wavelet transform, graph, time-frequency analysis, waveform, eccentricity*

Résumé

Avant même le début de cette thèse les détecteurs LIGO ont pour la première fois détecté une onde gravitationnelle émise lors de la coalescence d'une paire de trous noirs situés à 1.3 milliards d'années-lumière. Cette première de la toute nouvelle astronomie gravitationnelle a été suivie par plusieurs autres observations. La dernière en date est la fusion de deux étoiles à neutron dont la contrepartie électromagnétique a pu être observée par plusieurs observatoires à travers le monde, commençant ainsi l'astronomie multi-messager. Ces observations ont été rendues possibles par des techniques avancées d'analyse de données. Grâce à elles, la faible empreinte laissée par une onde gravitationnelle dans les données de détecteurs peut être isolée. Le travail de cette thèse est dédié au développement d'une technique de détection d'ondes gravitationnelles ne reposant que sur une connaissance minimale du signal à isoler. Le développement de cette méthode consiste plus précisément à introduire une information sur la phase du signal d'onde gravitationnelle selon un contexte astrophysique déterminé. La première partie de cette thèse est consacrée à la présentation de la méthode. Dans une seconde partie cette méthode est appliquée à la recherche de signaux d'ondes gravitationnelles en provenance de systèmes binaires de trous noirs de masse stellaire dans du bruit Gaussien. Puis l'étude est répétée dans du bruit instrumental collecté pendant la première période de prise de données de LIGO. Enfin la troisième partie est dédiée à la recherche de binaires de trous noirs dont l'orbite montre un écart à la géométrie circulaire, ce qui complexifie la morphologie du signal. De telles orbites sont qualifiées d'excentriques. Cette troisième analyse permet d'établir de premiers résultats quant à la méthode proposée lorsque le signal d'intérêt est peu connu.

Les ondes gravitationnelles sont une prédiction de la théorie de la relativité générale d'Einstein publiée en 1916. Dans ce cadre, l'interaction gravitationnelle est comprise comme un changement de géométrie de l'espace-temps, *i.e.* une modification dans la mesure des distances et des durées pour différents observateurs. La dynamique de l'espace-temps met en équilibre la géométrie de l'espace-temps encodée par la métrique $g_{\mu\nu}$ avec son contenu en énergie/matière au travers des équations d'Einstein :

$$G_{\mu\nu} = R_{\mu\nu} - \frac{1}{2}Rg_{\mu\nu} = \frac{8\pi G}{c^4}T_{\mu\nu} \quad (1)$$

Les ondes gravitationnelles apparaissent naturellement comme une conséquence de la linéarisation des équations d'Einstein. En effet, si on perturbe la métrique plane de Minkowski $\eta_{\mu\nu}$ par une perturbation $h_{\mu\nu}$ avec $|\eta_{\mu\nu}| \gg |h_{\mu\nu}|$, et que l'on choisit de manière pertinente les jauges (*i.e.* en fixant le système de coordonnées), alors les équations d'Einstein s'écrivent comme une équation d'onde pour la perturbation :

$$\square \bar{h}_{\mu\nu} = -\frac{16\pi G}{c^4}T_{\mu\nu} \quad (2)$$

où $\square = \partial_\mu \partial^\mu$ est l'opérateur d'Alembertien sur l'espace-temps de Minkowski, $\bar{h}_{\mu\nu} = h_{\mu\nu} - \frac{1}{2}h\eta_{\mu\nu}$ et h est la trace de $h_{\mu\nu}$. Cette équation d'onde prédit que les ondes gravitationnelles se déplacent à la vitesse de la lumière. Dans le cas où cette onde se propage dans le vide, les solutions sont des ondes planes dont les perturbations agissent dans un plan perpendiculaire au sens de propagation de l'onde. Le choix de jauge permet de mettre en évidence deux modes de polarisation des ondes gravitationnelles qui sont les seuls degrés de libertés physiques (*i.e.* non inhérents au choix de jauge). *In fine*, l'amplitude de l'onde gravitationnelle atteignant un observateur situé à une distance r ne dépend que de la dynamique interne de la source au travers de la distribution de masse. A l'ordre quadrupolaire, l'amplitude de l'onde gravitationnelle est donnée par

$$[h_{ij}^{TT}(t, \vec{x})]_{quad} = \frac{4G}{rc^4} \ddot{Q}_{ij} \left(t - \frac{r}{c} \right) \quad (3)$$

où Q_{ij} est le moment quadrupolaire de masse de la source. Si on considère deux objets supposés ponctuels de masses m_1 et m_2 décrivant une orbite excentrique d'excentricité e , alors la perturbation à l'ordre quadrupolaire est:

$$h_+(t) = \frac{G^2 m_1 m_2}{ac^4 D_L (1 - e^2)} \left\{ \left(\frac{1 + \cos^2 \iota}{2} \right) [\zeta(e, \phi) \cos 2\Phi + \Xi(e, \phi) \sin 2\Phi] - \sin^2 \iota \Psi(e, \phi) \right\} \quad (4)$$

$$h_\times(t) = \frac{G^2 m_1 m_2}{ac^4 D_L (1 - e^2)} \cos \iota [\zeta(e, \phi) \sin 2\Phi - \Xi(e, \phi) \cos 2\Phi] \quad (5)$$

où a est le demi-grand axe de l'ellipse, D_L est la distance de luminosité de la source, ι est l'angle d'inclinaison du plan orbital par rapport à l'axe de visée de l'observateur, Φ est l'angle entre la projection de la ligne de visée sur le plan orbital et le demi grand axe de l'ellipse et ϕ est la phase orbitale. Les fonctions $\Xi(e, \phi)$, $\zeta(e, \phi)$ et $\Psi(e, \phi)$ contiennent la modulation de phase conférée par une géométrie excentrique. Ces fonctions traduisent le fait que contrairement au cas d'une orbite circulaire, la fréquence de l'onde gravitationnelle n'est plus la moitié de la fréquence orbitale mais le tiers. On remarque que les deux équations ci-dessus se réduisent à l'émission en onde gravitationnelle attendue pour une binaire avec une orbite circulaire lorsque $e = 0$.

Les sources d'ondes gravitationnelles sont très variées mais toutes impliquent des objets astrophysiques qualifiés de compacts. Ces derniers sont les vestiges d'étoiles massives après l'épuisement de leur combustible nucléaires et regroupent les naines blanches, les étoiles à neutrons ou encore les trous noirs. La principale source d'ondes gravitationnelles est celle liée à la coalescence d'objets compacts. Pour les observatoires terrestres, seules les binaires incluant des étoiles à neutron et/ou des trous noirs importent. Les étoiles à neutron se forment lorsqu'une étoile massive explose lors du phénomène de supernova et lorsque le résidu de l'explosion n'est plus supporté que par la pression de dégénérescence des neutrons qui composent alors le noyau. Les trous noirs de masse stellaire se forment lorsque l'étoile est si massive que rien ne peut contrebalancer les effets dû à la gravité. La matière en chute libre est alors concentrée en une singularité qui modifie profondément la courbure de l'espace-temps. Lorsque ces objets orbitent l'un autour de l'autre, le moment quadrupolaire du système binaire s'en trouve modifié tout le long de l'orbite et l'ensemble des deux corps émet des ondes gravitationnelles. Après ou bien pendant leur formation ces objets sont susceptibles de former des systèmes binaires composés d'astres orbitant l'un autour de l'autre. Selon le milieu dans lequel s'est produit la formation et dans lequel la binaire évolue, il se peut que l'orbite montre une déviation plus ou moins prononcée par rapport à une orbite circulaire. C'est, par exemple, le cas lorsqu'une binaire d'objets compacts entre en résonance avec un troisième objet ou lorsque deux trous noirs situés dans les alentours du centre galactique se rencontrent et forment une binaire à l'occasion d'une émission d'ondes gravitationnelles. Les canaux de formations des binaires excentriques de trous noirs impliquent tous des environnements stellaires denses tels que les amas globulaires ou les noyaux de galaxie.

Une fois émise par sa source, une onde gravitationnelle se propage jusqu'à la Terre en interagissant très peu avec la matière. Là, des détecteurs sont susceptibles de la détecter, et ce, grâce au principe de l'interférométrie laser. Lors du passage de l'onde, celle-ci engendre une très faible modification de la distance entre deux masses tests. En mesurant cette modification provoquée par le passage de l'onde entre une paire de masses tests (miroirs) situées au bout des deux bras d'un interféromètre de Michelson, il est possible de détecter le passage d'une onde gravitationnelle grâce à l'évolution temporelle de la figure d'interférence. Cette même figure traduit l'évolution de phase caractéristique du signal gravitationnel. Comme toute onde sphérique, une onde gravitationnelle voit son amplitude décroître de façon inversement proportionnelle à la distance à la source. Une fois arrivée au niveau des détecteurs, celle-ci a donc une très faible amplitude. Typiquement, deux trous noirs de 10 masses solaires chacun et localisé à 100 Mpc donnent une amplitude de $h \sim 10^{-21}$. Pour des interféromètres dont la longueur des bras est de l'ordre du kilomètre, la variation de distance à mesurer est de 10^{-18} m. Il faut donc isoler les détecteurs d'onde gravitationnelle des sources de bruit environnantes : activités anthropiques, vent, séismes, ... tout en améliorant leur sensibilité. Idéalement, les instruments sont limités par des bruits qualifiés de fondamentaux : à faible fréquence, les perturbations sismiques ainsi que les perturbations locales du champ de gravité de nature atmosphérique induisent un mouvement indésirable des miroirs; à haute fréquence, les fluctuations dans le temps d'arrivée des photons provoquent un bruit de nature quantique; et dans une gamme de fréquence intermédiaire, les fluctuations thermiques des miroirs et des pendules au bout desquels les miroirs sont suspendus contribuent eux aussi à une perte de sensibilité de l'instrument.

Au cours des dernières décennies, plusieurs observatoires d'ondes gravitationnelles ont été construits puis assemblés afin de former un réseau de détecteurs. Trois détecteurs sont actuellement en mesure de prendre des données : les deux interféromètres américains LIGO localisés à Handford et Livingston et l'interféromètre européen VIRGO situé à Cascina en Italie. Après plusieurs années, ces instruments ont subi des améliorations permettant de les isoler de plus en plus des différentes sources de bruit. Les détecteurs de seconde génération fonctionnent dans leur version avancée : ADVANCED LIGO et ADVANCED VIRGO. ADVANCED LIGO a été

le premier à prendre des données dès décembre 2015 et a été rejoint pendant la seconde période de données par ADVANCED VIRGO en août 2017. D'autres instruments sont en préparation à travers le monde : LIGO INDIA qui est prévu pour rejoindre le réseau actuel de détecteurs vers 2025 et KAGRA, un instrument japonais situé non loin de Tokyo qui pourrait devenir opérationnel en 2020. Une troisième génération de détecteurs est à l'étude, à la fois du côté américain avec COSMIC EXPLORER et européen avec EINSTEIN TELESCOPE. Ceux-ci auront une sensibilité encore accrue par rapport aux instruments de seconde génération déjà cités. En parallèle, un projet d'interféromètre spatial nommé LISA dont le lancement est prévu pour 2034, sondera la partie basse fréquence du spectre d'onde gravitationnelle (entre 0,1 mHz et 100 mHz). La technologie prévue pour LISA a été testée avec succès lors de la mission LISAPATHFINDER qui s'est achevée en juillet 2017.

Avec des instruments de sensibilité croissante, il est possible de chercher des signaux d'ondes gravitationnelles de plus en plus faibles dans les données interférométriques. Toutefois, la présence de bruit instrumental et environnemental rend nécessaire d'analyser les données bruitées avec des méthodes permettant de détecter le signal et d'estimer les paramètres physiques de la source. Deux méthodes d'analyse sont couramment utilisées à cette fin. Une première méthode nommée *filtre adapté* consiste à comparer le signal observé à un modèle théorique du signal attendu nommé *patron d'onde*. Ce modèle théorique est établi par une résolution numérique ou perturbative des équations d'Einstein. Le patron d'onde est une fonction des paramètres physiques de la source, ce qui rend la méthode du filtre adapté dépendante d'un modèle physique. De tels patrons sont calculés afin d'assurer une couverture raisonnablement uniforme de l'espace des paramètres de la source (masses, spins, excentricité, ...). À des fins de détection, une statistique de détection est calculée afin de quantifier objectivement la confiance dans la détection d'un événement. L'avantage de disposer d'un modèle est aussi d'estimer directement les paramètres du modèle. Par le biais de l'inférence bayésienne, on obtient alors les distributions de probabilité *a posteriori* sur les paramètres. Celles-ci contiennent toute l'information sur l'incertitude de l'estimation. Une seconde méthode de détection consiste à analyser le signal observé par un réseau de détecteurs dans le domaine temps-fréquence à l'aide de transformée en ondelettes. En effet, une simple transformée de Fourier contient toute l'information sur le contenu fréquentiel du signal, mais ne donne aucune information sur l'évolution temporelle du contenu en fréquence. Ainsi la transformée de Fourier, appliquée à des signaux de fréquence variable, ne permet pas d'étudier la phase du signal. Au contraire, les ondelettes sont une base de fonctions à la fois localisées en temps et en fréquence qui autorise une étude de la phase du signal. Dans un second temps, la méthode identifie les excès d'énergie dans le plan temps-fréquence. Une statistique de détection mesure l'intensité et la cohérence en phase du signal sur l'ensemble du réseau de détecteurs. Contrairement aux détections basées sur le filtre adapté, ces recherches dites de tranistories "génériques" (aussi appelées recherches temps-fréquence) ne reposent pas sur un modèle de source proprement dit. Cette méthode rend possible la détection de sources d'ondes gravitationnelles encore inconnues.

C'est sur le principe de la seconde méthode de détection que repose un algorithme de détection nommé *Coherent WaveBurst* (cWB), largement utilisé dans cette thèse. cWB est capable de détecter des signaux transitoires d'ondes gravitationnelles grâce à la transformée de Wilson-Daubechies-Meyer (WDM). Cette famille d'ondelettes a l'avantage d'être bien localisée dans le domaine temps-fréquence. cWB décompose le signal en provenance de chacun des détecteurs sur plusieurs résolutions temps-fréquences afin que cWB puisse capter toute la variabilité de phase. Puis, cWB utilise une statistique de maximum de vraisemblance afin de déterminer la position de la source dans le ciel. En effet, le temps d'arrivée d'un signal à chaque détecteur du réseau dépend de la position de la source dans le ciel et aussi à cause de la disposition des détecteurs sur la surface de la Terre. Ainsi, on peut calculer le temps de vol du signal d'un instrument à l'autre. La détermination de la position de la source permet alors de savoir comment combiner les cartes temps-fréquence. cWB identifie ensuite un ensemble d'ondelettes ou de pixels sur la carte temps-fréquence combinée qui appartient au signal. Cet ensemble de pixels est appelé *cluster*. Enfin, cWB évalue si le cluster correspond à un événement d'onde gravitationnelle en calculant plusieurs quantités comme la force du signal, sa cohérence ou son facteur de qualité. La confiance dans une détection est estimée à partir de l'analyse de bruit de fond. De cette façon, on estime la fréquence à laquelle une réalisation de bruit peut donner lieu à un signal tel que celui observé. cWB n'impose aucune contrainte sur la morphologie du cluster qu'après que celui-ci ait été calculé.

Au contraire, la méthode développée au cours de cette thèse, nommée *Wavegraph* (WG), introduit une connaissance *a priori* du signal dès l'étape de groupement des pixels. L'idée derrière Wavegraph est d'orienter la sélection des pixels temps-fréquence, qui est faite par cWB, en ayant recours à des patrons d'ondes. En ce sens, Wavegraph peut être perçu comme une approche intermédiaire entre les recherches de type filtre adapté et les recherches génériques. De la même façon, Wavegraph utilise aussi des banques de patrons d'ondes qui couvrent une région déterminée de l'espace de paramètre de la source. Avec la transformée WDM de cWB, Wavegraph

décompose chaque signal de la banque en un ensemble de pixels. L'étape de groupement des pixels spécifique de Wavegraph est accomplie par un algorithme permettant d'assurer une décomposition parcimonieuse du signal : le cluster final doit agglomérer un nombre minimal de pixels pour approximer un signal avec une erreur donnée. Wavegraph utilise le *matching pursuit* pour décomposer le signal. Le principe du matching pursuit est d'itérativement sélectionner le pixel qui couple le mieux avec le signal initial (celui avec le coefficient WDM maximal), de soustraire l'ondelette correspondante du signal initial (le signal résultant est nommé *résidu*) et de calculer la transformée WDM du résidu. Ces trois étapes sont répétées jusqu'à ce qu'un critère de terminaison soit vérifié (par exemple : la norme du résidu est inférieure à une fraction de la norme du signal initial). Chaque itération du matching pursuit extrait un pixel qui est présent dans le cluster final. Ces pixels sont ensuite reliés un à un dans le plan temps-fréquence, de sorte à former une chaîne de pixels. La manière de relier les pixels dépend de l'évolution de phase du signal. Par exemple, l'évolution de phase associée à une coalescence d'objets compacts selon une trajectoire quasi-circulaire est un "chirp", *i.e.* une évolution monotone croissante de la fréquence avec le temps. Dans ce cas, la règle d'ordonnancement tend à suivre l'évolution de phase du modèle. Les deux étapes de sélection et d'assemblage des pixels sont répétées pour chaque patron d'onde dans la banque. Autant de clusters sont récoltés. A cause de la taille finie du maillage temps-fréquence, plusieurs clusters peuvent partager un ou plusieurs pixels en commun. Du fait des liens entre les pixels, ce(s) pixel(s) crée(nt) des connexions entre les clusters. Ainsi, l'ensemble des clusters crée un graphe dont les nœuds sont les pixels/ondelettes et les arêtes sont les liens. C'est avec ce graphe construit à partir de modèles de signaux (sans bruit donc) que l'on cherche dans les données interférométriques. Concrètement, les données blanchies de détecteurs sont transformées dans le plan temps-fréquence avec la transformée WDM et les coefficients WDM de chaque pixel sont stockés dans le graphe. Un dernier algorithme cherche finalement le chemin dans le graphe orienté qui contient le plus d'énergie. Ce cluster final subit finalement les mêmes étapes que les clusters extraits par cWB.

Au cours de cette thèse, Wavegraph est utilisé conjointement à cWB dans plusieurs contextes. D'abord, Wavegraph avec cWB (cWB+WG) est comparé à cWB seul dans les recherches de binaires de trous noirs de masse stellaire en orbite quasi-circulaire dans un bruit simulé. L'étude consiste en une estimation de la sensibilité au bruit de fond puis en une simulation Monte-Carlo avec un graphe donné. La simulation consiste à injecter des signaux d'ondes gravitationnelles dans un bruit Gaussien simulé. Les injections sont choisies de sorte que leurs paramètres physiques concordent avec l'espace de paramètres du graphe. Dans un second temps, les segments de données simulées sont analysés par cWB ou cWB+WG. En procédant de la sorte, on peut estimer les apports de Wavegraph par rapport à l'algorithme de groupement de cWB. L'analyse du bruit de fond révèle que cWB+WG est d'avantage affecté par les fluctuations de bruit que cWB seul. Il en résulte que des contraintes plus fortes doivent être placées sur la force du signal afin d'être assez confiant dans la détection d'une onde gravitationnelle. Pour ce qui est de la simulation, Wavegraph est capable d'extraire plus efficacement les pixels appartenant au signal par rapport à cWB seul. Cela est permis par le matching pursuit et par conséquent par la parcimonie de la représentation du signal. Un autre point fort de Wavegraph avec cWB est que l'ensemble des deux méthodes permet de détecter d'avantage d'injections que cWB seul. Cela montre que malgré une plus forte sensibilité au bruit, Wavegraph peut détecter plus de signaux. De plus, d'avantage d'injections à grande distance sont détectées en incluant Wavegraph. Cela signifie que l'ajout de Wavegraph à cWB permet de sonder une plus grande fraction d'Univers. Quantitativement, cWB avec Wavegraph augmente de 20 – 25% le volume relatif d'Univers exploré.

Dans un second temps, l'analyse précédente a été répétée avec du bruit réel collecté pendant la première prise de données d'*Advanced LIGO*. C'est une étape vers une étude plus réaliste des performances de Wavegraph puisque le bruit inclut des non gaussianités. Il s'agit de bruits transitoires peu ou non modélisés. Il est par conséquent difficile de les soustraire des données. La structure de graphe a aussi l'avantage de pouvoir servir de modèle pour l'évolution de l'amplitude. Autrement dit, on peut utiliser l'information sur l'amplitude du signal observé pour distinguer les signaux d'origine astrophysique des bruits transitoires. Ce nouveau *test de consistance* inhérent à Wavegraph s'ajoute aux contraintes déjà imposées par cWB. L'étude du bruit de fond indique que cWB avec Wavegraph donne de moins bons résultats que cWB seul, et ce, avec l'application du test de consistance. Cela montre que ce test échoue pour le moment à rejeter les transitoires. Un si grand écart se répercute lors des simulations car Wavegraph ne parvient pas à améliorer la sensibilité de cWB. Plusieurs raisons sont suspectées : le manque de parcimonie dans le matching pursuit et un test de consistance encore en développement.

Comme expliqué plus haut, les recherches de type filtre adapté utilisent l'information de phase prodiguée par des patrons d'ondes. Par conséquent, ces recherches sont très sensibles aux écarts de phase avec le modèle.

A titre d'exemple, les patrons d'ondes associés à des orbites excentriques montrent un écart d'autant plus important aux modèles d'orbites circulaires que l'excentricité de l'orbite est plus grande. Autrement dit, pour de faibles valeurs d'excentricité, les recherches de filtre adapté restent robustes. Mais pour des déviations plus importantes, l'efficacité de ces méthodes décroît très rapidement. Toutefois, les recherches temps-fréquences ne nécessitent pas un accord de phase qui soit continu sur toute l'étendue du signal. Le cas des signaux excentriques est pertinent car il n'existe pour le moment pas de modèles de signaux couvrant l'ensemble des valeurs possibles d'excentricité. Ce simple fait met en défaut les recherches de filtre adapté. Le fait de travailler avec des ondelettes fait que des méthodes comme Wavegraph ont besoin d'un accord local (et non plus global) de phase avec le modèle. En cela, Wavegraph est plus robuste quand il s'agit de chercher des signaux dont la phase est encore mal connue. De plus, la méthode peut être étendue à plusieurs classes de signaux : émission en onde gravitationnelle de supernovæ ou instabilité de disque d'accrétion.

C'est ce qu'on propose d'étudier dans une dernière étude. L'analyse de bruit de fond et la simulation sont répétées sur des segments de données réels dans lesquels sont injectés des signaux excentriques (de relative-ment faible excentricité $e < 0.6$). Encore une fois, un graphe est calculé qui couvre l'espace de paramètre des injections. Le "graphe excentrique" montre une grande complexité de part le nombre de connexions dans le graphe. Le plus grand nombre de patrons d'ondes nécessaires pour couvrir un espace de paramètre avec une dimension supplémentaire et la complexité de l'évolution de phase des signaux excentriques. En effet, la morphologie du signal excentrique dans le plan temps-fréquence montre l'existence de plusieurs harmoniques en accord avec l'expression des polarisations donnée plus haut. De fait, le graphe excentrique est encore plus sensible au bruit qu'avec un graphe circulaire. Les coupes à appliquer sur les clusters sélectionnés par Wavegraph sont alors plus drastiques que celles de cWB seul. A l'occasion de cette étude, un jeu de coupes différents des coupes standard de cWB est utilisé. Ces coupes sont construites de manière heuristique et utilisent des non-linéarités entre les grandeurs calculées par cWB afin de départager au mieux les populations d'événements injectées des réalisations de bruit. On montre que ces coupes non-linéaires profitent à Wavegraph puisque le nombre d'événements détectés par cWB avec Wavegraph est plus élevé qu'avec les coupes standard. Les deux effets combinés de la grande complexité du graphe et des coupes expliquent les résultats obtenus lors de cette étude. La sélection des pixels avec Wavegraph n'est plus autant corrélée sur l'ensemble du réseau, la reconstruction du signal est de fait moins bonne et enfin la sensibilité de Wavegraph en terme de distance est moins marquée. Il suit que les résultats de la méthode sont imputables à des défauts de la méthode elle-même qu'il est nécessaire de corriger. Plusieurs solutions peuvent être envisagées : réduire la connectivité du graphe (les nombreuses connexions du graphe sont d'autant plus d'opportunités pour le cluster d'énergie maximale de dévier d'une "route physique" à cause de fluctuations de bruit), choix d'une autre règle d'ordonnancement des pixels pour le cas des binaires excentriques (en optant pour une décomposition temps-fréquence calculée harmonique par harmonique, on conserve un ordonnancement qui est celui d'un chirp pour chaque harmonique), adapter les résolutions temps-fréquences de cWB (dans le cas des binaires excentriques, les niveaux de résolution sont différemment peuplés selon les valeurs d'excentricité), utiliser une coupe de cWB qui porte sur la polarisation du signal en vue de réduire le bruit de fond ou encore utiliser des techniques de *machine learning* toujours dans le but de rejeter les événements de bruit (cette approche peut-être vue comme une continuité des coupes non-linéaires utilisées dans l'avant-dernier chapitre).

En conclusion, ce travail de thèse a permis de développer puis d'appliquer une méthode d'analyse temps-fréquence de signaux transitoires d'onde gravitationnelle. Wavegraph a pu être appliqué dans différents contextes de signaux émis par des coalescences de trous noirs et différents contextes de bruit. Des analyses de bruit de fond et de la sensibilité de la méthode par rapport à cWB ont pu être menées puis interprétées dans chaque cas. Le dernier cas des binaires excentriques a été l'occasion d'apprécier le comportement de Wavegraph dans le cas de signaux astrophysiques encore mal modélisés. Cette dernière étude a permis de mettre en évidence certaines limites de la méthode pour lesquelles des solutions potentielles sont proposées afin d'étudier plus avant notre Univers.

Mots-clés: *onde gravitationnelle, trou noir binaire, transformée en ondelettes, graphe, analyse temps-fréquence, patron d'onde, excentricité*

Introduction

Since their prediction by Albert Einstein in 1916 gravitational waves (GW) raised interest among scientists. Those ripples of space-time are emitted through the bulk motion of very massive astrophysical objects. Compact binary coalescences are GW sources of primary importance. Those are binaries of stellar remnants (neutron star and/or black holes) that orbit each other and lose gravitational potential energy through GW radiation, thus leading to the decay of their orbital separation till they merge and form a new object.

Detecting GW requires high-precision metrology experiments capable of measuring the very small deformation of space induced by the wave. Kilometric scale laser interferometers have been designed to measure a GW strain amplitude $h \sim 10^{-21}$, sufficient to make first direct observations of GW from distant astrophysical sources.

At the beginning of this thesis work, in September 2015, the two US-based ADVANCED LIGO detectors made the first direct observation of GW from a binary black hole (BBH) merger GW150914. Since then, the French-Italian ADVANCED VIRGO detector began operations as well and five more BBH mergers have been detected by those instruments, as well as a binary neutron star merger GW170817. The latter was observed jointly in GW and with conventional telescopes observing the electromagnetic spectrum from radio to γ -ray wavelengths.

GW astronomy will develop in the future as more detectors come online such as Kagra in Japan and LIGO India. A third generation of instruments is planned with the EINSTEIN TELESCOPE in Europe and the COSMIC EXPLORER instruments in the US. A space interferometer LISA is also expected to be launched around 2034.

Many more sources are expected from the future observations. It is possible that future discoveries will come from less standard and perhaps unexpected astrophysical scenarios.

Data analysis methods are a central piece of this science. Efficient algorithms are required for the reliable extraction of the gravitational wave strain signal from noisy measurements. Two main search strategies (“modeled” and “un-modeled”) are currently used to detect the GW transient signals.

The first approach takes advantage of the *a priori* knowledge of the GW waveform, obtained by solving for the dynamics of the source. For compact binary coalescences, the inspiral and merger phases are resolved using a mix of relativistic approximations. The search consists in finding the signal that best matches with the observations by correlating the interferometric data with a large set of templates to covers the high-dimensional source parameter space. The phase accuracy of the templates is of paramount importance for this type of search.

A second approach consists in analysing the GW observations in the time-frequency domain, and identify excess of energy in the time-frequency plane that are coincident and coherent in phase in all observations of the detector network. Contrary to modelled searches, time-frequency searches rely on minimal assumptions on the targeted signals.

Here, we explore an intermediate route that can prove useful when the available GW waveform models are incomplete, or with limited phase accuracy. This is for instance the case for compact binary coalescences when the binary interact gravitationally with its environment leading to a non-standard elliptic or “eccentric” orbital motion. These systems are investigated in the thesis.

This thesis studies a data analysis method named *Wavegraph* which is a modification of the un-modeled GW

transient search pipeline Coherent WaveBurst (cWB) developed and applied to LIGO and VIRGO data. Wavegraph revisits the pattern matching idea underlying in matched filtering searches, and apply this idea to the time-frequency pattern rather than the time- or frequency-domain waveform. To do so, the method uses a “wavelet graph” that collect all targetted time-frequency patterns motivated by an astrophysical waveform model. The goal is to improve the sensitivity of un-modeled searches to the model described in the graph.

In Chapter 1 we present the basics of gravitational wave theory, how GW emerge from the linearized master equations of general relativity and what are their fundamental properties.

In Chapter 2 we do a comprehensive review of the formation scenarios for the compact binaries mergers observed by LIGO and Virgo from stellar evolution, to compact object and compact binary formation. We also discuss the formation channels for compact objects binaries with a non-zero orbital eccentricity.

In Chapter 3 we describe the physics of gravitational wave detectors and their fundamental noises, with a special focus on the second generation of detectors in operation now. We also explain the advantages of a multiple detector network.

In Chapter 4 we introduce the main GW searches performed by the LIGO and VIRGO collaborations. A special emphasis is put on compact binary coalescence and burst sources which constitute the main target of the detection techniques developed here. We describe the cWB pipeline in detail as it has a central role in this thesis.

In Chapter 5 Wavegraph is introduced as a potential solution for the poorly explored regions of the compact binary coalescence search parameter space. We describe the main steps of the algorithm from the wavelet graph computation to the clustering scheme, and explain how it fits in the cWB pipeline. The second part of the chapter is about a proof-of-concept for Wavegraph. We show the gain in sensitivity for the detection of stellar-mass binary black hole signals in simulated Gaussian noise. This part of the thesis has been published in a journal publication [1]. The final part of the chapter reviews the techniques used to deal with the transient noise component and shows the performance of the algorithm in real noise conditions. A publication [2] is in preparation.

In Chapter 6 Wavegraph is applied in the context of eccentric binary black hole searches during the first observing run of LIGO. A set of preliminary remarks are formulated upon the time-frequency representation of eccentric waveforms. The available eccentric models are discussed. We introduce a variant of the sparse approximation algorithm of Wavegraph presented in [3]. We present an astrophysically-motivated population model of stellar mass binary black holes segregating towards the galactic nuclei of a Milky-Way-like galaxy and gaining in eccentricity at the occasion of runaway encounters. These encounters are favoured by the steep density cusp formed by the central supermassive black hole inhabiting the core of the galaxy. Three searches are compared to detect the previous population of eccentric mergers: cWB alone, cWB with Wavegraph using a graph computed with a circular bank of templates and cWB with Wavegraph with an eccentric template bank. Their respective figure-of-merits are compared and interpreted.

In Chapter 7 we conclude with an outlook and perspective for the presented method.

Chapter 1

Gravitational wave theory

Contents

1.1	Linearised theory of general relativity	15
1.2	Lorenz gauge	17
1.3	Solution in vacuum and traceless-transverse gauge	17
1.4	The multipole expansion	18
1.5	Energy radiated by gravitational wave sources	20

In the 17th century Sir Isaac Newton presented a first description of the gravitational interaction as the result of forces applying on systems. From there the motion of bodies and celestial objects became describable and permitted first observational tests (moon, planets and asteroids orbits). Together with the theory of electromagnetism, the laws of mechanics in constant speed frames have been unified in the same theory of special relativity by Einstein [4]. Ten years later, Albert Einstein refined his theory by including accelerated frames (located far from a gravitational source) and showed that they are equivalent to an inertial frame plunged inside a gravitational field. This effect is known as the equivalence principle and constitutes the underlying key idea behind the general theory of relativity [5]. Two years later Einstein demonstrated that *Gravitational wave* (GW) naturally arise from a linearisation of general relativity equations [6].

In this first chapter we present how gravitational waves arise from the linearisation of *General relativity* (GR) master equations, then their basic properties and finally we express the low order expression for the energy and momentum they radiate.

1.1 Linearised theory of general relativity

A common framework in modern theories is the least action principle or Lagrangian approach. Such a framework unifies the description of physical laws. A theory is described as the consequence of the minimization of a functional called the *action*. Its main advantage is to easily establish a parallel with other classical field theories (Maxwell theory). In the case of general relativity, the *Hilbert-Einstein action*

$$\mathcal{S}_{HE} = \frac{c^4}{16\pi G} \int \sqrt{-g} R d^4x \quad (1.1)$$

describes the gravitational interaction. In Eq (1.1) $g = \det(g_{\mu\nu})$ is the determinant of the *metric* $g_{\mu\nu}$ which describes the local geometry of space-time and R is the Ricci scalar. The integral is carried over the whole space-time. We denoted Newton's gravitational constant G and the speed of light in vacuum c . In presence of matter, an additional term is included in the integrand so as to get:

$$\mathcal{S} = \mathcal{S}_{HE} + \mathcal{S}_m \quad (1.2)$$

with the matter-dependent action term:

$$\mathcal{S}_m = \int \sqrt{-g} \mathcal{L}_m d^4x \quad (1.3)$$

where \mathcal{L}_m is the Lagrangian associated to matter. Putting the action Eq (1.3) in the Euler-Lagrange equations evidences the relation between the stress energy-momentum tensor $T_{\mu\nu}$ and \mathcal{L}_m . The variation of the action also yields to the *Einstein field equation* (EFE).

$$G_{\mu\nu} = R_{\mu\nu} - \frac{1}{2}Rg_{\mu\nu} = \frac{8\pi G}{c^4}T_{\mu\nu} \quad (1.4)$$

On the left hand side, $R_{\mu\nu}$ is the Ricci tensor and $R = R^\mu{}_\mu$ is again the Ricci scalar defined as the contraction of the Ricci tensor. On the right hand side, $T_{\mu\nu}$ is the stress energy-momentum tensor encoding the space-time content in matter, energy, and/or momentum. The left hand side of Eq (1.4) is purely geometric while the right hand side describes space-time content. In Wheeler's terms: "*Spacetime tells matter how to move; matter tells space-time how to curve*" [7]. This citation encapsulates the non-linearity of efe. From the mathematical point of view EFE consists in a set of 10 non-linear coupled partial derivative equations and are hence difficult to solve.

The quantity of interest in the EFE is the space-time metric. Few solutions are known in some specific cases where space-time geometry shows an important degree of symmetry. When the gravitational field is weak (*ie.* far away from massive objects) one can approximate the metric $g_{\mu\nu}$ at the first order around a point in space-time denoted x^λ .

$$g_{\mu\nu}(x^\lambda) = \eta_{\mu\nu} + h_{\mu\nu}(x^\lambda) + \mathcal{O}(h^2) \quad (1.5)$$

where the $\eta_{\mu\nu} = \text{diag}(-, +, +, +)$ tensor is the Minkowski metric describing a flat/Newtonian spacetime. Let us see now how the perturbed metric in Eq (1.5) evolves according to the EFE. For this we need to go through intermediate computations until getting a first order approximation of the Einstein tensor $G_{\mu\nu}$. This begins with the so called Christoffel symbols (or metric connexion)

$$\Gamma^\alpha{}_{\mu\nu} = \frac{1}{2}g^{\lambda\alpha}(\partial_\mu g_{\lambda\nu} + \partial_\nu g_{\lambda\mu} - \partial_\lambda g_{\mu\nu}) \quad (1.6)$$

which relate how a given 4-vector changes when parallel transported along a given closed line. Said differently, it quantifies how much the local system of coordinates will change under a small displacement $x^\lambda \rightarrow x^\lambda + \delta x^\lambda$. At first order we have:

$$\Gamma^\alpha{}_{\mu\nu} = \frac{1}{2}(\eta^{\lambda\alpha} - h^{\lambda\alpha})(\partial_\mu h_{\lambda\nu} + \partial_\nu h_{\lambda\mu} - \partial_\lambda h_{\mu\nu}) \quad (1.7)$$

$$= \frac{1}{2}\eta^{\lambda\alpha}(\partial_\mu h_{\lambda\nu} + \partial_\nu h_{\lambda\mu} - \partial_\lambda h_{\mu\nu}) + \mathcal{O}(h\partial h) \quad (1.8)$$

where $\eta^{\alpha\beta}h_{\alpha\beta} = h$ is the perturbation trace. In the first line we use the fact that the Minkowski metric is flat everywhere and thus do not vary over space and the expression of the perturbed inverse metric. On the second line we neglect second-order terms in $h_{\mu\nu}$. We then obtain the first order approximation of the Riemann tensor defined as:

$$R^\mu{}_{\nu\alpha\beta} = \partial_\alpha \Gamma^\mu{}_{\nu\beta} - \partial_\beta \Gamma^\mu{}_{\nu\alpha} + \Gamma^\mu{}_{\alpha\sigma} \Gamma^\sigma{}_{\nu\beta} - \Gamma^\mu{}_{\beta\sigma} \Gamma^\sigma{}_{\nu\alpha} \quad (1.9)$$

The two last terms can be neglected as they are a product of Christoffel symbols and are hence of order 2 in h . We can then linearise the Ricci tensor $R_{\alpha\beta} = R^\mu{}_{\alpha\mu\beta}$ defined as the contraction of the Riemann tensor on its first and third indices. Its expression at first order in $h_{\mu\nu}$ is

$$R_{\nu\beta} = \frac{1}{2}(\partial_\sigma \partial_\nu h^\sigma{}_\beta + \partial_\sigma \partial_\beta h^\sigma{}_\nu - \square h_{\nu\beta} - \partial_\nu \partial_\beta h) + \mathcal{O}(h^2) \quad (1.10)$$

where $\eta^{\alpha\beta}\partial_\alpha\partial_\beta = \square$ is the d'Alembertian operator on a flat spacetime. Finally we introduce the trace of the Ricci tensor $R = R^\mu{}_\mu = \partial^\nu \partial^\beta h_{\nu\beta} - \square h + \mathcal{O}(h^2)$. From here one can write the linearised expression of the Einstein tensor $G_{\alpha\beta} = R_{\alpha\beta} - \frac{1}{2}Rg_{\alpha\beta}$ as

$$G_{\nu\beta} = \frac{1}{2}(\partial_\sigma \partial_\nu h^\sigma{}_\beta + \partial_\sigma \partial_\beta h^\sigma{}_\nu - \eta_{\nu\beta} \partial^\sigma \partial^\lambda h_{\sigma\lambda} - \square h_{\nu\beta} - \partial_\nu \partial_\beta h + \eta_{\nu\beta} \square h) + \mathcal{O}(h^2) \quad (1.11)$$

The increasing number of terms for the geometric part of EFE can be simplified by introducing the *trace-reversed metric perturbation* $\bar{h}_{\alpha\beta} = h_{\alpha\beta} - \frac{1}{2}\eta_{\alpha\beta}h$ in the previous equation as it creates vanishing terms in Eq (1.11). In the end one arrives to the linearised EFE

$$\partial_\nu \partial^\gamma \bar{h}_{\beta\gamma} + \partial_\beta \partial^\gamma \bar{h}_{\nu\gamma} - \eta_{\nu\beta} \partial^\lambda \partial^\sigma \bar{h}_{\lambda\sigma} - \square \bar{h}_{\nu\beta} = \frac{16\pi G}{c^4}T_{\nu\beta} \quad (1.12)$$

In the next section we reduce Eq 1.12 to a wave equation whose source resides in space-time content.

1.2 Lorenz gauge

The previous section left us with a wave-like equation for the trace-reversed perturbation metric. But the metric tensor components are not all fixed by the gauge choice or said differently the system of coordinates (x^λ) has not totally constrained the remaining degrees of freedom. We can greatly simplify Eq (1.12) by fixing non-physical degrees of freedoms.

An infinitesimal change of coordinates is the transformation $x^\mu \rightarrow x'^\mu = x^\mu + \xi^\mu$ where the four functions $\xi^\alpha = \xi^\alpha(x^\beta)$ remain to be determined. The metric transforms according to

$$g'_{\alpha\beta} = g_{\mu\nu} \frac{\partial x^\mu}{\partial x'^\alpha} \frac{\partial x^\nu}{\partial x'^\beta} = g_{\mu\nu} \left(\delta_\alpha^\mu - \frac{\partial \xi^\mu}{\partial x^\alpha} \right) \left(\delta_\beta^\nu - \frac{\partial \xi^\nu}{\partial x^\beta} \right) \quad (1.13)$$

$$= g_{\alpha\beta} - g_{\alpha\nu} \frac{\partial \xi^\nu}{\partial x^\beta} - g_{\beta\mu} \frac{\partial \xi^\mu}{\partial x^\alpha} + \mathcal{O}(\xi^2) \quad (1.14)$$

$$= \eta_{\alpha\beta} + h_{\alpha\beta} - \frac{\partial \xi_\alpha}{\partial x^\beta} - \frac{\partial \xi_\beta}{\partial x^\alpha} + \mathcal{O}(\xi^2) \quad (1.15)$$

where we dropped the short-cut notation for the partial derivatives to evidence the system of coordinates. The first equation above is the tensor transformation law applied to the space-time metric. On the second line only first order terms in ξ have been kept. Hence the metric perturbation $h_{\alpha\beta}$ transforms as

$$h'_{\alpha\beta} = h_{\alpha\beta} - \partial_\beta \xi_\alpha - \partial_\alpha \xi_\beta + \mathcal{O}(\xi^2) \quad (1.16)$$

and the trace-reverse metric perturbation $\bar{h}_{\alpha\beta}$ transforms as

$$\bar{h}'_{\alpha\beta} = \bar{h}_{\alpha\beta} - \partial_\beta \xi_\alpha - \partial_\alpha \xi_\beta + \eta_{\alpha\beta} \partial_\mu \xi^\mu + \mathcal{O}(\xi^2) \quad (1.17)$$

In the end this shows the infinitesimal variation of coordinates leave the Riemann tensor components unchanged. As a result space-time geometry remains unchanged under an infinitesimal change of coordinates and one can arbitrarily choose a set of functions ξ^α or equivalently a system of coordinate where Eq (1.12) simplifies. In what follows we will use the so-called *Lorenz*¹ or *harmonic gauge* characterised by

$$\partial^\mu \bar{h}_{\mu\nu} = \square \xi = 0 \quad (1.18)$$

In this way the $\partial^\mu \bar{h}_{\mu\nu}$ quantity is left invariant under the infinitesimal change of coordinates considered so far. Finally Eq (1.12) reduces to a pure wave equation

$$\square \bar{h}_{\alpha\beta} = -\frac{16\pi G}{c^4} T_{\alpha\beta} \quad (1.19)$$

with a source term linked to space-time content $T_{\alpha\beta}$. This equation shows that the space-time perturbation propagates at the speed of light and are called *gravitational waves* (GW). It is worth emphasizing we have reduced the number of degrees of freedom from 10 (number of independent metric components since $g_{\mu\nu}$ is symmetric) to 6 (since we uniquely defined the four equations ξ^α).

1.3 Solution in vacuum and transeless-transverse gauge

We dedicate the end of this chapter to vacuum solutions for the wave equation, that is when $T_{\mu\nu} = 0$. Due to the well known nature of Eq.(1.19) it is natural to look for plane wave solutions

$$\bar{h}_{\alpha\beta}(x^\lambda) = A_{\alpha\beta} e^{ik_\lambda x^\lambda} \quad (1.20)$$

where $A_{\alpha\beta}$ is a constant matrix amplitude and $k_\lambda = (\omega, \vec{k})$ is the wave 4-vector composed of the wave pulsation ω and the wave vector \vec{k} . Combining Eq (1.20) with $\square \bar{h}_{\alpha\beta} = 0$ it is evident k^λ is a light-like 4-vector since one arrives to the following dispersion relation

$$k^\lambda k_\lambda = 0 \quad (1.21)$$

¹Not to be confounded with the Dutch physicist Hendrik Antoon Lorentz (1853-1928) known for the Lorentz transform of special relativity. We are talking about the Danish physicist Ludvig Valentin *Lorenz* (1829-1891) [8]

Also, if we suppose that the wave is moving along the z axis then we have $k_\lambda = (\omega/c, 0, 0, -\omega/c)$ so that $k_\lambda x^\lambda = \omega(t - z/c)$. In this situation the Lorenz condition (1.18) is equivalent to

$$A_{\alpha\lambda}k^\lambda = 0 \quad (1.22)$$

This tells us that the wave solution we are looking for is transverse, *ie.* it has an effect on the plane orthogonal to the propagation direction of the wave. Let us place ourselves in the Lorenz gauge and make an infinitesimal change of coordinates in order to cancel some of the components of $A_{\alpha\beta}$. For this we pose

$$\xi^\alpha(x^\lambda) = B^\alpha e^{ik_\lambda x^\lambda} \quad (1.23)$$

where B^α are four constants to be determined. By construction ξ^α is a solution of Eq (1.18) and it generates an infinitesimal change of coordinates that preserves the Lorenz gauge. Applying Eq (1.17) we deduce that the amplitude components transform as

$$A'_{\alpha\beta} = A_{\alpha\beta} - iB_\alpha k_\beta - iB_\beta k_\alpha + \eta_{\alpha\beta} B^\sigma k_\sigma + \mathcal{O}(\xi^2) \quad (1.24)$$

If we now impose $\eta^{\alpha\beta} A'_{\alpha\beta} = 0$ and $A'_{0i} = 0$ then we get $\bar{h} = 0$ and $\bar{h}_{0\alpha} = 0$ thanks to the previously derived transformation laws. A direct consequence is that $h_{\alpha\beta} = \bar{h}_{\alpha\beta}$ with these new constraints. Naturally we can write them as

$$h = 0 \quad (1.25)$$

$$h_{0\alpha} = 0 \quad (1.26)$$

These conditions entirely fix the degrees of freedom and the additional gauge is called the *Traceless-transverse* (TT) gauge. The *traceless* part comes from the relation Eq (1.25) and the *transverse* part comes from Eq (1.26). Applying the TT gauge constraints is equivalent to specifying four B^α functions which decreases again the number of degrees of freedom from 6 to 2. The remaining degrees of freedom correspond to the *physical gravitational wave polarization modes*. By symmetry the z propagating wave has only four non-vanishing components and can thus be written as

$$h_{\alpha\beta} = \begin{pmatrix} 0 & 0 & 0 & 0 \\ 0 & h_+(t - z/c) & h_\times(t - z/c) & 0 \\ 0 & h_\times(t - z/c) & -h_+(t - z/c) & 0 \\ 0 & 0 & 0 & 0 \end{pmatrix} \quad (1.27)$$

with

$$h_+(t - z/c) = a_+ e^{i\omega(t - z/c)} \quad (1.28)$$

$$h_\times(t - z/c) = a_\times e^{i\omega(t - z/c)} \quad (1.29)$$

and where we denoted $a_+ = A_{xx}$ and $a_\times = A_{xy}$. Fig 1.1 shows the effect of the two polarisations on a ring of test masses located at $z = 0$. The distance between two test masses changes at the GW frequency and with opposite signs in orthogonal directions. Modern GW detection experiments rely on the measurement of this differential effect as we will see in Chapter 3.

1.4 The multipole expansion

The previous section evidences the existence of plane wave solutions to the linearised EFE in the vacuum (away from source). Here we propose to solve Eq (1.19) with a non-zero source term and to relate the expressions of h_+ and h_\times to the physics of the source.

The results derived in this section will be applicable to weak self-gravitating sources *ie.* when GW sources are located far from the observer and be considered as point-like sources. From the mathematical point of view Eq (1.19) is a linear partial derivative equation with constant coefficients. It also satisfies the Lorenz gauge. The stress-energy tensor satisfies the conservation law, $\partial_\mu T_{\mu\nu} = 0$. A natural way of finding a solution is the formalism of *Green's functions*. We look for a function $\mathcal{G}(x)$ that verifies

$$\square \mathcal{G}(x^\lambda - x'^\lambda) = \delta^4(x^\lambda - x'^\lambda) \quad (1.30)$$

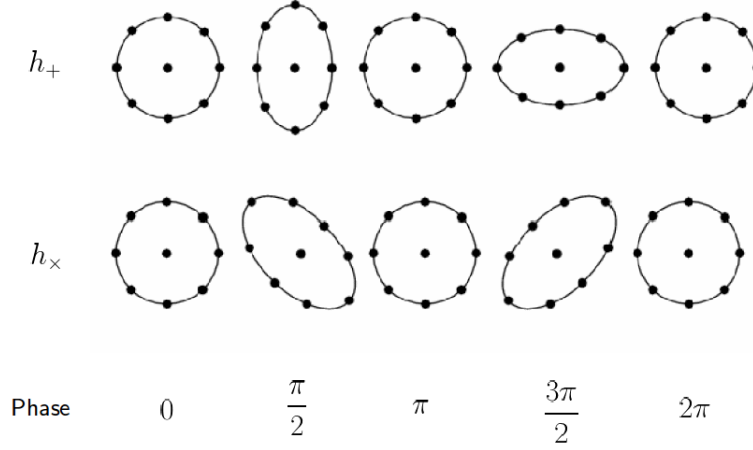


Figure 1.1: Effect of a GW on a ring of test mass particles for the two GW polarisations h_+ and h_\times . The direction of propagation is assumed to be orthogonal to this page.

where $\delta(x^\lambda)$ denotes the Dirac function evaluated in a given point of space-time. A general solution of Eq (1.19) is

$$h_{\mu\nu}(x^\lambda) = -\frac{16\pi G}{c^4} \int d^4x'^\lambda \mathcal{G}(x^\lambda - x'^\lambda) T_{\mu\nu}(x'^\lambda) \quad (1.31)$$

where the integral is tracked over the past light-cone of the source. As the signal is travelling at finite speed from the source, the Green's function takes the form of a retarded potential:

$$\mathcal{G}(x^\lambda - x'^\lambda) = -\frac{1}{4\pi|\vec{x} - \vec{x}'|} \delta(x_{ret}^0 - x'^0) \quad (1.32)$$

with $x'^0 = ct'$ and $x_{ret}^0 = ct_{ret} = ct - |\vec{x} - \vec{x}'|$ the retarded time due to the GW propagating from the source to the observer. Combining these elements and writing the solution in the TT gauge the general solution outside the source has the form:

$$h_{ij}^{TT}(t, \vec{x}) = \frac{4G}{c^4} \int d^3\vec{x}' \frac{1}{|\vec{x} - \vec{x}'|} T_{kl}(t_{ret}, \vec{x}') \quad (1.33)$$

Note the integral only depends on spatial components T_{kl} . Following the notations of section 3.2 of [9] and [10], far from the source one has $|\vec{x}'| \ll r$ where $r = |\vec{x} - \vec{x}'|$ is the distance of source. for a distant observer, we can thus expand $|\vec{x} - \vec{x}'| \sim r(1 - (\vec{n} \cdot \vec{x}')/r)$ (see Eq (6.113) of [10]) since the typical size of the source is much smaller than the source distance. The expression for h_{ij}^{TT} now turns to be

$$h_{ij}^{TT}(t, \vec{x}) = \frac{4G}{rc^4} \int d^3\vec{x}' T_{kl} \left(t - \frac{r}{c} + \frac{\vec{x}' \cdot \vec{n}}{c}, \vec{x}' \right) \quad (1.34)$$

with $\vec{x} = r\vec{n}$. The non-vanishing contribution of the integral comes from the source. If we neglect the contributions coming from the scan of the detailed internal structure of the source (the dot product in Eq (1.34)) we can pursue with an additional Taylor expansion in terms of the stress-energy tensor spatial components:

$$T_{kl} \left(t - \frac{r}{c} + \frac{\vec{x}' \cdot \vec{n}}{c}, \vec{x}' \right) = T_{kl} \left(t - \frac{r}{c}, \vec{x}' \right) + \frac{x'^i n_i}{c} \partial_0 T_{kl} + \frac{1}{2c^2} x'^i x'^j n_i n_j \partial_0^2 T_{kl} + \mathcal{O} \left(\frac{1}{c^3} \right) \quad (1.35)$$

All the time derivatives are evaluated at the retarded time t_{ret} . The terms of the previous approximation reduce to moments of T_{ij} when replaced in Eq (1.34). Their expressions are given in Eqs (3.31)-(3.33) of [9] upto the third order approximation and are denoted by S^{ij} , $S^{ij,k}$ and $S^{ij,kl}$ in what follows:

$$h_{ij}^{TT}(t, \vec{x}) = \frac{4G}{rc^4} \left[S^{kl} + \frac{1}{c} n_m \dot{S}^{kl,m} + \frac{1}{2c^2} n_m n_p \ddot{S}^{kl,mp} + \mathcal{O} \left(\frac{1}{c^3} \right) \right]_{ret} \quad (1.36)$$

The whole terms between brackets is evaluated at retarded time (hence the subscript "ret"). The previous relation is known as the *multipole expansion* of the solution h_{ij} . Each term of the expansion corresponds to a power in $1/c^2$ and can be further decomposed in mass momenta (moments of T_{00}) and momentum density

momenta (moments of T_{0i}). In 1916, Albert Einstein obtained the *quadrupole formula* which corresponds to the zero-th order term in Eq (1.36), that is $S_{ij} = \dot{M}_{ij}$ where M_{ij} is the quadrupole mass moment.

$$M_{ij} = \frac{1}{c^2} \int d^3\vec{x} T_{00}(t, \vec{x}) x_i x_j \quad (1.37)$$

The quadrupole formula is finally expressed by

$$[h_{ij}^{TT}(t, \vec{x})]_{quad} = \frac{4G}{rc^4} \ddot{Q}_{ij} \left(t - \frac{r}{c} \right) \quad (1.38)$$

where we introduced the traceless mass moment $Q_{ij} = M_{ij} - (1/3)\delta_{ij}M_{kk}$. At lowest order, the GW emission is driven by the second derivative of the quadrupole mass moment. In other words, GW are emitted by massive objects whose internal motion has a quadrupole momenta.

The GW amplitude is inversely proportional to the distance of source to the observer. This is common to all orders in the multipole expansion so that GWs can be regarded as a spherical wave. The lowest non-vanishing order term in the expansion is the quadrupole order. The monopole (resp. dipole) term vanishes because of the energy (resp. angular momentum) conservation. Note this contrasts with the electromagnetic radiation since light is emitted by charged particles and the leading order term is the dipole term.

Consider a source with radius R , mass M and asymmetry factor ϵ . An order of magnitude estimate of its quadrupole moment is thus $Q \sim \epsilon MR^2$. And if we denote by T its typical time evolution, then one has $\dot{Q} \sim MR^2/T^2 \sim \epsilon Mv^2$. Putting all these quantities in Eq (1.38) yields

$$h \sim \epsilon \frac{G}{c^4} Mv^2 \sim \epsilon \frac{GM}{rc^2} \left(\frac{v}{c} \right)^2 \quad (1.39)$$

for a source located at a distance r from the observer. Under this form it is clear that loud GW sources must have an important mass and velocities. For example, a 1 m radius and 20 m-height steel cylinder rotating at breaking limit 28 rad/s would emit a GW whose amplitude is $h \sim 10^{-37}$ at a distance of 1 m. As we will see in the next chapter this value is not measurable by actual GW experiments. As a conclusion reasonable sources of GW are both massive and moving at almost relativistic speeds. Those two conditions are fulfilled when dealing with astrophysical objects such as compact binary mergers composed of neutron stars and/or black holes (see Chapter 2). A typical order of magnitude for astrophysical sources is $h \sim 10^{-21}$.

1.5 Energy radiated by gravitational wave sources

During the Chapel Hill, NC conference in 1957, F. Pirani followed by R. Feynmann proposed a simple thought experiment on the physics of GW. Think of two beads allowed to freely slide along a rigid rod with a minimal amount of friction and imagine a passing GW: *Will the relative distance change between the two beads induce an overhear measurable by an ideal thermometer?* It took time to the scientific community to reach a consensus [11]: GW do carry some energy.

The expressions we have obtained have been derived by linearising equations of GR and thus get rid of non-linear effects such as the back-propagation of the GW to the source, spin-orbit interactions or tidal effects. Especially the energy and momentum conservation law $\partial_\mu T_{\mu\nu} = 0$ must hold whatever is the degree of modelling of the source. Integrating the energy-momentum conservation on a volume delimited by a sphere \mathcal{S} centred on the source, one gets to the general formulation of the GW luminosity

$$\frac{dE}{dt} = \frac{r^2 c^3}{32\pi G} \int_{\mathcal{S}} d\Omega \langle \dot{h}_{ij}^{TT} \dot{h}_{ij}^{TT} \rangle \quad (1.40)$$

where the brackets $\langle \cdot \rangle$ denote an average over several orbits for the case of a binary merger. Substituting Eq (1.38) in Eq (1.40) we arrive to the quadrupole energy term first derived by A. Einstein in 1916 [6].

$$\left(\frac{dE}{dt} \right)_{quad} = \frac{G}{5c^5} \langle \ddot{Q}_{ij} \ddot{Q}_{ij} \rangle \quad (1.41)$$

A complete calculation shows that the system also loses angular momentum. The loss contributions come from the orbital angular momentum and the "spin" of each object as shown in [9]. A pair of objects both with mass $30 M_\odot$ orbiting at frequency 75 Hz and separated by 350 km gives a gravitational energy flux of 10^{50} W.

Chapter 2

Astrophysical sources of gravitational waves

Contents

2.1	Gravitational wave and multi-messenger astronomy today	21
2.1.1	Gravitational wave detections	21
2.1.2	The era of Multi-messenger astronomy	23
2.2	An overview about compact objects	24
2.2.1	Stellar evolution in brief	24
2.2.2	Formation of compact objects	27
2.2.3	How do compact binaries form ?	29
2.2.4	GW emission from compact object binaries	32
2.3	Gravitational waves from eccentric binaries	33
2.3.1	Formation channels	34
2.3.2	GW emission from eccentric binaries	35

In chapter 1 we described GW as ripples of space-time carrying energy and angular momentum. Their physical properties are tightly related to the physics of their source. However have not dealt yet with their astrophysical sources. Most of the expected GW sources involve *compact objects* either isolated or in a binary system.

In the first part of the present chapter we review the recent detections made by LIGO and VIRGO and the related advent of multi-messenger astronomy. The second part gives an overview of stellar evolution, discuss how compact objects form and how they group in binaries. The last part reviews two main formation channels for forming binary black hole in eccentric binaries which is of particular interest for this thesis.

2.1 Gravitational wave and multi-messenger astronomy today

2.1.1 Gravitational wave detections

Gravitational wave astronomy based on the direct observations of those waves by a dedicated instrument begins with the large scale interferometric detectors LIGO and VIRGO that we briefly describe in Chapter 3. Shortly after the start of the ADVANCED LIGO first observation run on September 14 2015, the two LIGO observatories detected a GW signal (now known as GW150914) [12]. This signal has been emitted by a merging pair of black holes with masses about $36 M_{\odot}$ and $29 M_{\odot}$. The GW radiation was emitted in the local Universe at $z \sim 0.09$ at a luminosity distance between 230 and 570 Mpc. A century after Einstein's prediction, GW150914 is the first direct detection of a gravitational wave signal and the first observation of a *Binary black hole* (BBH). Despite the low statistic in the number of detections at the time of the event many studies have been lead:

- **Source parameter inference** When crossing the detector network the GW deposits a signal in each detector data segments. The GW waveform phase depends on the masses and spins of the two objects and other physical parameters depending on the source model. The amplitude varies with the source sky location, the luminosity distance and the orbit inclination. A coherent Bayesian pipeline developed

in LIGO analyses each data stream to estimate the common GW source parameters that drive both the frequency and the amplitude [13]. As a result, posterior probability distributions are estimated for the extrinsic (sky location) and intrinsic (other parameters) using various waveform models [14]. The specific parameter estimation study performed on GW150914 suppose either the spin of the objects are aligned with the orbital angular momentum (SEOBNR model) while the second allows for a precession of the orbital plane (IMRPhenom model). The two provide consistent estimates. A common feature over all the detections achieved so far is the poor constraint on the spin values and only speculations on the astrophysical formation channel can be formulated: if the spins are aligned then it is an indicator that the binary has formed in the field (isolated binary) while if spins are not aligned then it is a clue for a binary formed in dense stellar environments. The energy released by the GW150914 event is estimated to be the difference between the final black hole mass and the sum of the two initial black holes masses. Overall the event released an energy $E_{rad} = 5, 3^{+0.9}_{-0.4} \times 10^{47}$ J which is 100 more powerful than the typical energy emitted by a *Gamma-ray burst* (GRB).

- **Tests of GR** A serie of tests have been pursued to evidence the tight link existing between the GW150914 event and predictions from GR [15]. As seen in chapter 1, the Post-Newtonian expansion until a given order is an expansion with a finite set of coefficients $\hat{\varphi}_i$. By allowing a tiny variation $\delta\hat{\varphi}_i$ and re-analysing the data, one measures the new coefficients $\hat{\varphi}_i(1 + \delta\hat{\varphi}_i)$. No significant differences were found that could evidence a deviation from GR. A following immediate test after the signal detection thanks to match-filter techniques is to subtract the best matching template from the data and check whether the residue is statistically consistent with a Gaussian noise. Finally, some theories predict a massive particle called the *graviton* associated to GW (according to the wave-particle duality and even if no quantum description of the gravitational interaction yet exist). GW150914 brought a constraint on the graviton Compton wavelength λ_g related to the mass of the graviton m_g as shown on Fig 8 of [15].
- **Rates** It is difficult to build robust rate estimates based only on a single event. That is why up to GW150914 the rate estimates were computed using population synthesis models [16] *ie.* simulated populations of astrophysical sources accounting for their physical properties like metallicity, opacity, eccentricity. The first BBH detections revealed a yet unknown sub-population of high stellar mass black holes. Estimates from GW150914 were performed using two mass distribution models [17]. The first one used a uniform distribution in the logarithm of the mass and the second used a power-law distribution (Salpeter's mass distribution [18]). The rate estimates have been derived with several detection pipelines and the combination of the results leads to a merger rate of $12 - 213 \text{ Gpc}^{-3} \text{ yr}^{-1}$. The precision in the rate estimate is primordial because it will serve as a discriminator between the BBH formation channels.

After GW150914, other BBH signals have been detected during LIGO's first observation run. The second GW signal GW151226 was detected on December 26, 2015 and is associated to a lighter system than GW150914 (14.2 and 7.5 M_\odot) [19]. The inspiral phase was particularly long so that the integrated strength of the signal is important. Also the phase evolution during the inspiral is guided by the *chirp-mass* \mathcal{M}_c value whereas the ringdown phase is only function of the *symmetric mass ratio* η . These two parameters are built upon the components masses. The GW150914 event thus yield a good estimate of \mathcal{M}_c . LVT151012¹ is a sub-threshold event observed on October 12, 2015. It is considered as a real GW event by most of the analyses although its significance does not reach the $5 - \sigma$ level [19].

After a quite short period of commissioning the LIGO detectors started again taking data on November 2016. Two others BBH detections occurred: GW170104 (farthest event to date [21]) and GW170608 [22]. In August 2017, the VIRGO instrument joined LIGO for a month of common observation. On August 14, 2017 the three-detector network detected a BBH event: GW170814. The VIRGO data allowed to put constraints on the GW polarization modes [23]. On August 17, 2017, the VIRGO and LIGO instruments detected the first GW signal likely to be emitted from a binary neutron star merger: GW170817 [24]. Contrary to the previous BBH detections, the neutron star binary motion is ruled by tidal interactions between the two objects. As they get closer each neutron star experiences stronger and stronger gravitational interactions from its companion. This deforms the mass repartition and contributes to the GW emission in the very late part of the inspiral phase. So the signal analysis enables to put constraints on the neutron star equation of state, mass and radii [25]. The detected GW signals are shown in Fig 2.1.

For BBH the three first detections provided a rate of $101^{+112}_{-89} \text{ Gpc}^{-3} \text{ yr}^{-1}$ combining the inferred rates from two astrophysical population model distributions presented in [21]. Population synthesis models together with

¹LVT stands for "LIGO-VIRGO trigger"

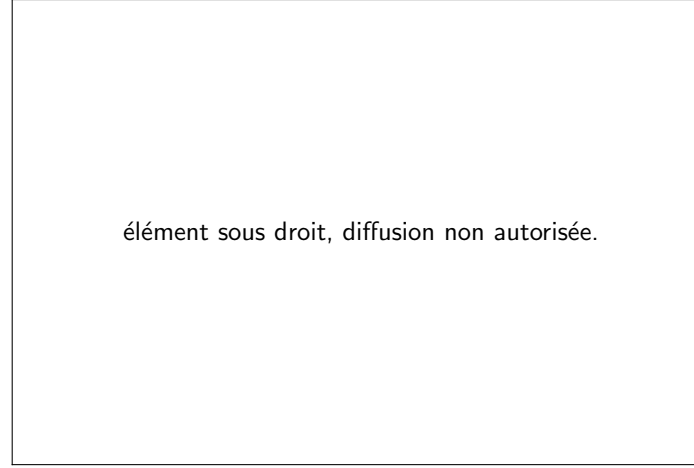


Figure 2.1: Detected BBH events by LIGO and VIRGO during O1 and O2. The best-matching template is represented and evidences the signal duration in the detector bandwidth. [20]

observed systems estimate the rate of *Binary neutron star* (BNS) mergers to be $1540^{+3200}_{-1220} \text{ Gpc}^{-3} \text{ yr}^{-1}$ [24]. The still large estimate has been in fact obtained thanks to the last detection made by LIGO and VIRGO. Finally only an upper limit of $3600 \text{ Gpc}^{-3} \text{ yr}^{-1}$ on NS-BH mergers has been obtained as no such GW source has been observed so far [26].

2.1.2 The era of Multi-messenger astronomy

On February 23, 1987 occurred the supernova SN1987a [27]. The star explosion was associated to both neutrino and electromagnetic emissions detected by various instruments. The observation through multiple channels has been very fruitful with a lot of physics results: source properties (main sequence progenitor mass, distance, metallicity), explanation on the burst neutrino revival mechanism and tracing of the progenitor evolution. Likewise, the GW170817 event has been observed in coincidence with a short GRB (GRB170817a) and a kilonova emission afterwards [28]. The γ -ray radiation has been detected 1.7 s after the GW signal by high-energy space telescopes (FERMI, INTEGRAL). It helped to constrain the sky location of the source together with some tests of the Lorentz invariance, gravity speed and equivalence principle. Finally, the GW signal brought a posterior distribution on the luminosity distance of the source as it scales as the inverse of the GW amplitude. The electromagnetic observation lead to the identification of the source host galaxy called New General Catalogue of nebulae and clusters of stars (NGC) 4993 and provided an estimate of the galaxy's redshift. GW170817 was the closest GRB ever detected with $D_L = 40^{+8}_{-14} \text{ Mpc}$ and is thus located in the local Universe where the approximate relation $cz \sim H_0 D_L$ holds. In the previous relation, z is the redshift and H_0 is the Hubble constant. The H_0 constant had thus been inferred to be $H_0 = 70^{+12}_{-8} \text{ km s}^{-1} \text{ Mpc}^{-1}$ at the 1σ confidence level and did not allow to resolve the tension between the supernovae and Cepheid estimates [29] and the cosmic microwave background measurements [30]. Nevertheless GW provided an independent distance ladder to probe the Universe over tens of Mpc.

The early stages of the detection have been independently performed by the γ -ray space based telescope FERMI and the LIGO-VIRGO GW observatories which first triggered a Gamma-ray Coordinate Network (GCN) ² alert to involved observatories in the electromagnetic follow-up campaign of GW events. Then FERMI was joint by INTEGRAL and a rough source localisation estimate has been inferred from the timing differences. This preliminary estimate constrained an area on the sky. Rapidly another more precise estimate is obtained thanks to GW data coming from the LIGO and VIRGO instruments. Regular updates of the best available skymap are then released among partners so as to facilitate again the follow-up by other instruments. It was the case for GW170817 since even "small" ³ facilities detected an optical counterpart. Later on a *kilonova* emission followed the GRB [32]. In fact nucleons present inside the neutron rich ejecta undergoes a rapid neutron capture that make them unstable. A radioactive decay of the heavy created elements warms up the surrounding environment. This very radiation can be observed from days to months after the prompt emission in the optical, UV, IR and

²Gamma-ray coordinate network. Initially proposed to trigger location and reports on GRB observations, GCN have been extended to GW transient events for which an Electromagnetic (EM) follow-up is possible alert to GW and EM partners observatories.

³"Small" designates telescopes with a relatively small light collecting area ($\leq 1 \text{ m}$ diameter) as compared to current major telescopes

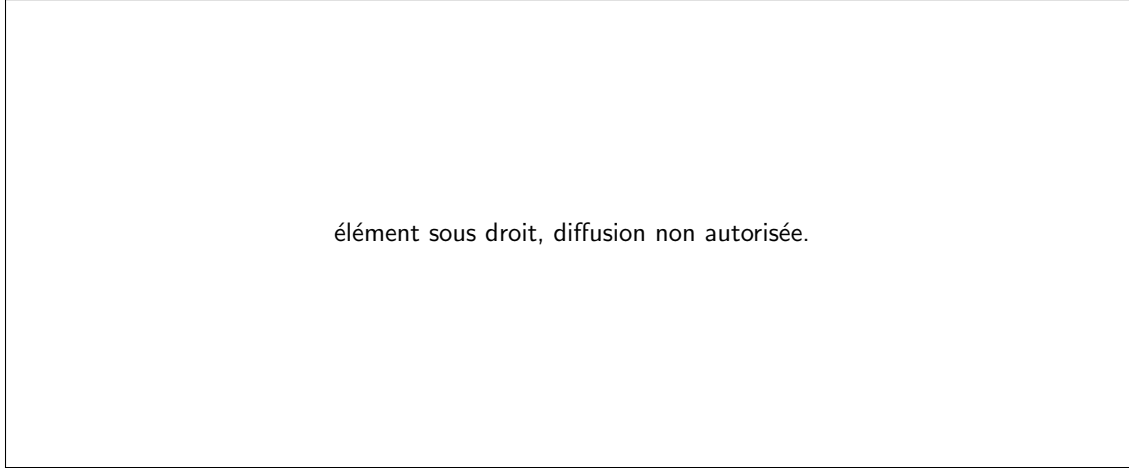


Figure 2.2: (*top left*) Light curve of the GRB170717A transient as observed by the FERMI space telescope. The red line corresponds to the background noise inherent to the low photon statistic in each bin. (*bottom left*) Coherently combined time-frequency representation of the GW170817 event seen by the two LIGO instruments. The merger occurs 1.7 s before the γ -ray luminosity peak. (*right*) Sky localisation obtained by FERMI, INTEGRAL and GW observatories. The dark blue patch is the FERMI/GBMinstrument field of view, the light blue stripe is the sky position constraint obtained from the time delay in each γ -ray detector. The light green patch is the sky position 90% credible region (190 deg^2) as determined by LIGO while the dark green area (31 deg^2) is the reduction of the previous patch accomplished thanks to the VIRGO data. [31]

radio spectrum ranges. All the observations are reported in Fig. 2 of [24]. A neutrino follow-up of the source by the ANTARES and KM3NET did not reveal any neutrino counterpart from GW170817.

2.2 An overview about compact objects

In this section we discuss how compact binary objects form from the early stages of main sequence stars. Emphasis is made on the two main tracks a single isolated star follows depending on its initial mass. Then we discuss more deeply two kinds of compact objects relevant for ground based interferometers, namely neutron stars and black holes.

2.2.1 Stellar evolution in brief

The *proto-stars* form in relatively dense molecular clouds composed of dust and cold hydrogen [33]. The cloud contracts and stretches depending on external conditions of the interstellar medium (stellar wind, nearby supernova, radiation pressure) so that density fluctuations appear that fragment the cloud. The fragmentation consists of a local gravitational collapse that overcomes the thermal pressure of the medium. The process is called the *Jeans instability*. In the case where the typical mass of the local over-density reaches a critical mass known as the *Jeans mass*, it undergoes a gravitational collapse (*ie.* a gravitational potential energy loss) during which time the temperature of the core increases. At this stage, the proto-star only emits light whose source is the star gravitational potential energy and is qualified as a *T Tauri* star [34] provided its mass is below $3 M_{\odot}$. As more and more matter is accreted on the center of mass, the core density keeps on increasing. In parallel, the temperature continues to increase until it eventually reaches the hydrogen fusion temperature ignition (typically $T \sim 10^7 K$). If so, the newly formed star becomes a *main sequence star*. In this configuration the star is in a hydrostatic equilibrium: the gravitational potential energy that tend to attract matter is balanced by the internal energy released through nuclear fusion reactions in the core. In the case where the initial mass of the cloud is insufficient to trigger nuclear reactions (typically below $0.08 M_{\odot}$), the proto-star continues radiating its potential energy and evolves into a *brown dwarf*⁴ [35]. On the contrary, if the mass is large (typically above $80 M_{\odot}$) the star luminosity exceeds the *Eddington luminosity*⁵.

⁴Eventually nuclear burning of the deuterium contained in the core may begin and rapidly stop

⁵The *Eddington luminosity* is a threshold luminosity a star must possess so as to stay in hydrostatic equilibrium. Beyond this limit the radiation pressure becomes more important than gravity and gas is ejected from the star.

A very useful tool to visualize the evolution and distribution of stellar populations is the *Hertzsprung-Russel* (HR) diagram [36]. It is a figure showing the luminosity of a star as a function of its surface temperature. With a very good approximation, stars can be regarded as a black body (*ie.* a body whose emitted spectrum only depends on its temperature) even if this underlying assumption is not always justified at all stages of stellar evolution. Populations are displayed which correspond to several evolutionary stages: *Main sequence* (MS) stars, dwarfs, giant branch, supergiant, *etc.*. All are not accessible to every star as the destiny of a star is guided by its initial mass. Indeed more massive stars will "burn" their nuclear fuel faster. As an example, a $6 M_{\odot}$ star will spend 10^8 yrs on the MS whereas a Sun-like star will spend 10^{10} yrs.



Figure 2.3: Color-magnitude diagram with various star populations. The color or spectral type is a classification of stars as a function of their emission spectrum and of their surface temperature while the magnitude quantifies its brightness. The main sequence forms a long stripe on which a star will spend 90 % of its life. Depending on its initial mass it will go through distinct evolution stages.

As an example, the Sun is a yellow dwarf lying on the MS. Its planned evolution for the 4.5 billion years to come is to transform into a red giant before slowly cooling down and form a white dwarf. Some other representations display constant radius lines which have some importance to explain a star brightness: the larger surface a star offers to the interstellar medium the brighter it appears for an observer. Radius also conditions the temperature: more surface means more efficient energy transfers with the interstellar medium.

Following sections describe the known stellar evolution scenarios for low and high-mass stars. These two populations are animated by distinct physics which lead to the formation of different star remnants.

Low-mass stars

The population of low-mass stars ($0.8 < M < 8M_{\odot}$) is characterised by a specific nuclear reaction on-going in its core: the *proton-proton chain reaction* (PP cycle) [37]. During the reaction, the hydrogen lying in the core is transmuted into helium. The reaction also produces two atoms of hydrogen that may be re-injected at the beginning of the resulting cycle for the PPI sub-cycle. The PP cycle is the dominant one and occurs within a star sitting on the MS. the lifetime of a star on the MS is approximately $10^{10}(M/M_{\odot})^{-2.5}$ yrs. At some point hydrogen is depleted in the core and the *Proton-proton* (PP) cycle progressively stops. The produced amount of helium during the PP cycle is inert for the core temperature is not sufficient to ignite its combustion. The hydrostatic equilibrium is no longer ensured and gravity tends to overcome the star internal energy. As a consequence the star contracts. So far an onion layers structure has formed with helium at the core and a surrounding residual layer of hydrogen. Nuclear reactions have stopped and convection motion of gases now dominates, allowing for the remaining hydrogen to burn at the periphery. The cooling of the star is associated to the expansion of the most superficial regions (its radius can exceed $10^3 R_{\odot}$). The growth of the star increases the surface it offers to the cold interstellar medium: the star temperature decreases (turns red) whereas the luminosity increases. On the HR diagram this stage correspond to the now called *red giant* leaving the MS and moving to the *horizontal branch*. Collapsing matter heats up the core of the newly formed *red giant* and triggers the helium burning. The main reaction mechanism is the *triple-alpha reaction* (3α reaction) through which three helium atoms fuse to produce a single carbon atom. Two cases should be discriminated depending on the progenitor mass:

- **$0.8 < M < 2M_{\odot}$** The inert helium core produced by burning hydrogen layers enriches the star core and progressively increases the core pressure. As the mass of the He core grows, it contracts until it is supported by degenerate electron pressure. A fundamental property of degenerate matter is that the pressure is no longer temperature dependent. The core continues to contract until it reaches 10^8 K. At this temperature, triple- α reactions begin in the core. As the rate of energy production for the triple- α process goes as T^{40} , this induces a violent, runaway He-burning.

This process is called the *helium flash* [38]. The sudden heating releases enough thermal energy to overcome the Fermi energy level and matter in the core is no longer degenerate. The outer layers are opaque and this violent process is not visible for a distant observer. In other words the star luminosity is constant and moves on the horizontal branch toward high temperatures. In this way the red giant star finally acquires a new thermal source and regains its hydrostatic equilibrium. Once again when the helium core is depleted the star contracts and triggers the fuse of heavier elements provided its mass is sufficient. The repetition of the process tends to make the onion structure more and more complex as the star moves to the *Asymptotic giant branch* (AGB) ⁶ (this phase last one million years for a solar mass star).

- **$M > 2M_{\odot}$** Those stars are dominated by the *carbon-nitrogen-oxygen cycle* (CNO cycle) during the MS phase (even if the PP cycle still occurs). This case is simpler than the previous one since the thermal expansion regulates the core temperature. As a result temperature smoothly increases until reaching the limit temperature for helium burning.

Both ways result in a AGB star with an inert core composed of carbon and oxygen, an helium layer surrounding the core and another superficial layer hosting the burning of hydrogen residues. As the star tries to regain hydrostatic equilibrium, there are successive stages of shell burning. Over time, the shell burning becomes unstable causing stronger and stronger thermal pulses inside the star. Eventually, the instabilities become so large that the outer layers of the star are ejected (stellar winds). After 10^5 years, the ionized gas envelope forms a *planetary nebulae* and leaves a hot core which will slowly cool down and lose energy. This object is supported by the pressure from a degenerate gas of electrons and forms a *white dwarf* [39]. Their small radius ($\sim 0.01 R_{\odot}$) give them a low luminosity and are hence found in the bottom-left part of the HR diagram (see Fig 2.3).

High-mass stars

For the population of high-mass stars ($M > 8M_{\odot}$), the initial stages of the evolution are the same as in the low-mass case: once the core is hydrogen exhausted, the star collapses and its envelop expands. However more massive stars go further in the process as they are able to reach the *blue supergiant stage* once they began fusing their carbon in the core. As the cycle of burning, depletions, contraction, expansion goes on, the temperature limit necessary to light on further nuclear reactions increases. This results in the acceleration of the burning rate of each element: helium, carbon, oxygen, nitrogen, neon, magnesium, ... Typically the burning of oxygen

⁶Only stars that are heavy enough to trigger the fusion of elements heavier than helium can reach this stage of stellar evolution.

lasts ~ 1 year whereas the burning of silicon lasts about 1 day [40]. Also each phase releases less and less energy as shown on Fig (2.4). Once a star starts to produce inert iron in its core the fusion cycle breaks. Indeed the fusion of iron is an endothermic reaction (*i.e.* energy needs to be put into the system for further reactions to occur), and is thermodynamically disfavoured.



Figure 2.4: Binding energy per nucleon curve. The dotted line shows the upper limit number of nucleons $A = 56$ (iron) to allow for the fusion nuclear reactions to release some energy. For higher values of A the reaction is disfavoured and compromises the coherent structure of the star.

At this point the nuclear fuel is exhausted in the core and the blue supergiant collapses. Unlike low-mass stars, the star is not massive enough to support the relativistic matter collapse. When the compacted mass exceeds a particular mass named the *Chandrasekhar limit* of about $1.4 M_{\odot}$, electron degeneracy is no longer efficient to counter the incoming matter. The density of the core sharply increases and soon a neutronisation occurs that produces neutrons and neutrinos through the inverse beta decay ($e^{-} + p \rightarrow n + \nu$) and electron capture (${}^A_Z X + e^{-} \rightarrow {}^A_{Z-1} Y + \nu_e$) reactions. Electron degeneracy in the core indeed disfavours the creation of electrons as all Fermi levels are already occupied.

A contraction occurs and continues until the electrons in the atoms are pulled inside the nucleus. This reduction in particle number causes the core to contract until it is stopped by neutron degeneracy pressure. Ultra-relativistic matter bounces onto the core and create shock waves that propagate outwards. This phenomenon is known as a *type II supernova* [41]. At such high densities neutrinos are trapped in the collapsing core ($R_{core} \sim 50 km$). Mechanism driving the next steps are not well known. It is believed the nuclear equation of state plays an important role as it stiffens towards high densities above $10^{14} g/cm^3$. This leads to the formation of a shock sonic wave propagating from the core to the outer medium. It is also suggested the explosion is revived by a post-bounce neutrino burst provoked by the initially trapped neutrinos on the core. It is made possible by the decreased neutrino opacity by the shock wave. But other revival mechanisms are investigated such as the magneto-rotational mechanism [42] and acoustic mechanism [43].

After the gigantic explosion occurred, the central core of the massive star is surrounded by a metal enriched environment. The core continues to collapse until either a new pressure contribution prevents any further collapse or the core mass is simply too important. The latter case lead to the formation of a stellar-mass black hole. Both ways head to the formation of compact objects which will be studied hereafter.

2.2.2 Formation of compact objects

Compact objects are defined as astrophysical objects related to the end life of stars. They no longer undergo thermonuclear reactions. Their internal physics is tightly linked to the most energetic phenomena in the Universe such as γ -ray bursts, micro-quasars or supernovae. The "compact" part of the denomination actually refers to the definition of the *compactness parameter* Ξ whose expression is $\Xi = GM/Rc^2$ where M and R are respectively the mass and the radius of the object. An immediate interpretation of the compactness is hence

the ratio of the gravitational potential energy of an object divided by its rest mass energy.

Object	Mass M (M_\odot)	Radius R (km)	Average density $\bar{\rho}$ ($g.cm^{-3}$)	Compactness Ξ
Sun	1	$6,96 \times 10^5$	1.4	2×10^{-6}
WD	$\sim 0.1 \rightarrow 1.4^{(*)}$	$\sim 10^4$	$\sim 10^6 \rightarrow 10^7$	$\sim 10^{-4} \rightarrow 10^{-3}$
NS	$\sim 1 \rightarrow 3^{(**)}$	~ 10	$\sim 10^{15}$	$\sim 0.2 - 0.4$
BH	$\gtrsim 3$	$8.9 \left(\frac{M}{3M_\odot} \right)$	undefined	1

Table 2.1: Compactness parameter for various astrophysical objects. The Sun is indicated as an element of comparison. (*) The mass upper limit is the typical Chandrasekhar limit. (**) The mass upper limit is the Tolman-Oppenheimer-Volkoff limit corresponding to the maximum mass a star with a degenerate neutron-matter core can have. [44]

An object will then be qualified of being *compact* if $\Xi \gtrsim 10^{-4}$. By convention $\Xi = 1$ for black holes which are the most compact sources. The notion of density is not defined for BH as they are not supported by any outward pressure contribution. Table 2.1 shows for various types of sources along with their typical physical properties. The two last columns highlight the fundamental difference existing between density (scales as M/R^3) and compactness (scales as M/R) which are often confounded. Indeed, one can find very dense objects with a very low compactness parameter: a proton as a mean density $\bar{\rho} = 5 \times 10^{17} kg.m^{-3}$ whereas $\Xi \sim 10^{-39}$. Hence GR effects at the scales of a proton are highly negligible [10]. In the rest of the present section we will be interested in other aspects of the compactness parameter. We will also focus only on compact objects whose gravitational wave emission is likely to be detected by ground based interferometers.

Neutron stars

Neutron stars were first postulated by Baade and Zwicky in 1934 [45], and later by Oppenheimer and Volkoff in 1939 [46]. As seen earlier in the present chapter, a *neutron star* (NS) is the final stage of stars whose initial mass is between 8 and 20 M_\odot . Its core is extremely dense (see Fig 2.1). At these extreme densities the core is degenerate and it is the strong interaction between elementary particles that counteracts gravity. The interior of a neutron star is composed of neutrons, protons and electrons in the most external layers while the interior structure remains quite uncertain. Existing models explore various possibilities: pions condensates, gluon-quark plasma, or preferably a superfluid and superconductive neutron-degenerate matter. This last model explains the very intense magnetic field $B \sim 10^{12}$ G (until 10^{15} G for magnetars) characterizing neutron stars. During the gravitational collapse leading to the formation of a neutron star, the angular momentum is conserved. As the size of the initial supergiant is tremendously reduced in a 10 km-radius sphere, the resulting NS has an important and impressively constant ($\dot{P}/P \sim -2 \times 10^{-15}$) rotation period from few milliseconds to few seconds. After the neutron star has formed the charged ejecta falls back onto the surface and follows the magnetic field lines until the electron reach the poles as shown on Fig (5.15) of [44]. Matter is accelerated by the magnetosphere and emits light mostly via synchrotron emission, inverse-Compton scattering (other population exit that emit in the X or γ -ray domain [47]). Coupled with a fast rotation the whole neutron star can be seen as a cosmic lighthouse for an observer located on the Earth. The continuously emitted beam may then be observed as pulses provided the beam path crosses the eye of an observer. This is why they are called *pulsars* [48]. With time the rotation period of the neutron star decreases because the system losses energy by radiating away electromagnetic and gravitational waves. Some NS models estimate the age of pulsars knowing their period and their orbital decay rate. But in some cases a pulsar regains some angular momentum from accretion mechanisms.

Black holes

Stellar-mass binary black holes arise from the final stage of stars whose initial mass is beyond 20 M_\odot [48]. Within this range of masses the final star is likely to overcome the *Tolman-Oppenheimer-Volkoff* mass limit which poses a strong upper mass limit of objects supported by a neutron degenerate core. Hence the unstable hypermassive neutron star (if any) temporarily formed at the end of the SNIa event further collapses. Once collapsed, the initial extreme matter density forms a *Black hole* (BH). A BH is a region of spacetime where the gravitational field is so intense that it prevents light emitted from the inside to escape. The notion of inside/outside of a

BH is related to the *event horizon*. BH are predicted by GR through many closed-form metric solutions to EFE: the Schwarzschild (1915) [49] solution describe space-time around a spherical non-rotating body, the Kerr (1963) [49] solution describes spacetime around a spherical rotating body and the Kerr-Newmann (1965) [50] solution describes a charged rotating black hole⁷. All the three solutions emphasize that there are actually three physical quantities characterising a BH: its mass M , its angular momentum J and its charge Q . In the astrophysical context it is however difficult to meet with a charged object as it creates an electric field that will rapidly attract charges of opposite sign. In this way charge quickly vanishes. For this reason it is considered that astrophysical BH are reliably described by the *Kerr metric*. In Boyer-Lindquist coordinates (t, r, θ, ϕ) its expression is

$$ds^2 = - \left(1 - \frac{2R_S r}{\Sigma^2} \right) c^2 dt^2 - \frac{4R_S a r \sin^2 \theta}{\Sigma^2} c dt d\phi + \frac{\Sigma^2}{\Delta} dr^2 + \Sigma^2 d\theta^2 + \left(r^2 + a^2 + \frac{2R_S a^2 r \sin^2 \theta}{\Sigma^2} \right) \sin^2 \theta d\phi^2 \quad (2.1)$$

where $R_S = 2GM/c^2$ is the BH radius and $a := J/Mc$ is the reduced angular momentum. Both can be combined so as to define the Kerr parameter $\bar{a} = a/R_S = Jc/GM^2$. The other quantities are

$$\Delta = r^2 - 2R_S r + \bar{a}^2 R_S^2 \quad (2.2)$$

$$\Sigma^2 = r^2 + a^2 \cos^2 \theta \quad (2.3)$$

Kerr metric is a stationary and axisymmetric solution since the components metric are all independent of t and ϕ . If $|J| > 0$ the above solution introduces a non-vanishing cross-term $g_{\phi t}$ with respect to the Schwarzschild solution which encloses the fact that the BH is rotating with respect to an observer located at infinity. It is clear the spacetime metric presents a physical singularity when $\Sigma = 0$. The event horizon is reached when $\Delta = 0$, *ie.* when

$$R_{EH} = R_S \left(1 + \sqrt{1 - \bar{a}^2} \right) \quad (2.4)$$

The apparent singularity in $r = R_{EH}$ is in fact a coordinate singularity. This means it is only due to the mathematical expression of the metric in a given system of coordinates. If one poses a change of coordinate to quit the Boyer-Lindquist system of coordinate then it is possible to dodge this apparent difficulty. It is important to make the distinction between the event horizon defined above and another surface named the *ergosphere* whose radius R_{ES} is defined the following way. Indeed, if $|J| > 0$ then a particle at rest in the Kerr metric is defined by $\Sigma > 2R_S r$ and $R_{EH} \leq r \leq R_{ES}$ [44]. Solving for the second order polynomial in r yields two roots one of which determines a surface beyond R_S . It corresponds to the ergosphere. The space in between the event horizon and the ergosphere is called the *ergoregion*

$$R_{EH} \leq r \leq R_{ES}(\theta) = R_S \left(\sqrt{1 - \bar{a}^2 \cos^2 \theta} \right) \quad (2.5)$$

Outside the ergosphere, a particle can be at rest or move in whatever direction. Inside the ergosphere, the particle cannot be at rest as it is dragged by the BH rotation. This effect is known as the *Lense-Thirring effect* [49].

2.2.3 How do compact binaries form ?

In this part we briefly recap how NS and BH assemble so as to form compact binaries. We will not go into details regarding the evolution of low-mass binaries since this channel is known to produce white dwarf binaries which are not expected to lie in the detection band of ground based instruments. Instead we decide to detail the formation processes of isolated high-mass binaries experiencing the common-envelope phase [51] then the chemically homogeneous evolution [52, 53] proposed to explain the high-mass sub-population evidenced by GW150914. The formation in dense stellar systems will be described in section 2.3.1 since it is the most relevant for formation of eccentric binaries.

Classical isolated high-mass binary evolution

Among stars that go through all the fusion phases, the estimated fraction of stars who live in binaries varies from 40 to 60 % for $M \sim M_\odot$ stars to almost 100 % for most massive O, B, A stars. A given binary is characterised by the components separation a and the mass ratio $q = m_2/m_1$ where m_1 and m_2 are the components

⁷One could also cite the Reissner-Nordstrom solution which describes a non-rotating but charged object.

masses. By convention one takes $m_1 > m_2$ so that the first component is called the donor or primary component whereas the other is the accretor or secondary companion (also called the companion). Due to mass transfer episodes those status are likely to be inverted during the binary evolution. For sufficiently-large separations (so called *wide binaries*) the components do not influence each other. Components of wide binaries then evolves independently of their companion. However in *close binaries* the evolution of stars passes by the progressive filling of the gravitational equipotentials of each component called the Roche lobe. The process is known as the *Roche lobe overflow* (RLOF) [54]. If one star starts to fill its Roche lobe then the matter outside this region is no more gravitationally bounded and can flow through the first Lagrangian point L_1 of the orbit. It is the most common way through which two stars exchange mass. In practice the Roche lobe radius R_L is a only a function of a and q [55]. Depending on the size of the companion, matter can fall directly to the surface or form an orbiting disk. In the case of *detached systems* components have their radii smaller than their Roche lobe, and no mass transfer via the RLOF process occurs and the only gravitational interaction resides in tides. If only one of the components fills its Roche lobe the system is said to be *semi-detached* while if both fills it a common photosphere composed of mixed superficial layers engulfs the binary. These systems are called *contact* or *common envelop binaries*. In this latter configuration it is also possible for the L_2 and L_3 points to be implicated in the mass transfer as the matter flow is highly unstable. Indeed if they are reached by one of the star radius a common disk may form that surround the whole binary.

Obviously the rhythm at which a star will fill its Roche lobe depends on its evolutionary cycle. While the binary components remain far separated, it is still the initial mass that rules each component life. The primary component then evolve through all the evolution stages described above to finally form a supergiant. At this occasion the star radius increases and the most external layers are less and less gravitationally bounded: the star progressively fills its Roche lobe and a stable mass transfer establishes.

Consider two massive main sequence stars with low metallicity ($Z \sim 0.05 Z_\odot$) in a wide binary (separation of the order of 10 AU). The donor evolves faster to the red supergiant phase and fills its Roche lobe. Because of the onion layer structure acquired by stars during their isolated evolution, the hydrogen envelop is first transferred to the companion. The primary component is now called a *Wolf-Rayet* (WR) star [56] a naked burning helium star emitting intense stellar winds ($10^{-5} M_\odot$) toward the accretor which likely widens the binary. As high-mass stars, WR objects explodes as a SNIa leaving either a NS or a BH depending on the mass that has been lost during its life. Note that because of the explosion the binary can be either disrupted or gain in eccentricity due to the explosion kick. It happens the companion star is also a massive star and evolves to the WR stage. Again it fills its Roche Lobe and this time an unstable mass transfer establishes from the secondary to the primary component. The material falls onto the accretor (which is now a compact object), piles up and starts to expand until eventually overfilling its Roche lobe. Such a system is a *high-mass X-ray binary* (HMXB) since it implies an accreting compact object and a high-mass star. An X-ray spectrum is emitted by the accretion disk formed by the falling material. The most known examples of a HMXB are Cygnus X-1 or Vela X.

As described above the formed semi-detached system undergoes a common envelop phase. During this phase the binary experiences dynamic friction by the surrounding helium gas and losses angular momentum which causes the orbits to shrink even more rapidly (timescale of the order of 100 years). Typically two outcomes are possible from this stage. In the first case, the orbit shrunk enough to cause the binary to merge within Hubble time. It results in an exotic configuration where the compact object is located at the core of red giant or red supergiant denominated as a *Thorne-Zytkow object* [58]. No observational evidences for such objects has been published, which corroborates the low number of observed events appearing on Fig (2.5). Surrounding matter finishes to collapse onto the compact object and finally a single NS or BH persists. In the second case, the two objects are brought on a close orbit but do not have time to merge. The system is composed of a compact object and a WR star moving in an evanescent gas envelop. Again the WR explodes as a SNIa and leaves two possible scenarios. Either the supernova explosion is strong enough to kick away the two compact objects so as to disrupt the binary system, either the binary is still composed of two gravitationally bounded compact objects. Again the system may gain in eccentricity but it very depends on the detailed supernova mechanism. In the second configuration, a compact binary system is formed which produces gravitational waves before it merges. It is worth noticing that in this isolated high-mass binary formation scenario, the orbit have likely circularised because of the tight configuration and the friction with the supernovae remnants. A scheme of the successive evolution stages is shown of Fig 2.5.



Figure 2.5: Evolution diagram of a high-mass binary star through the common envelope formation channel. The star at left (resp. right) is the primary (resp. secondary) component. T designates the typical evolution time scale associated to each stage and N denotes the estimated number of objects in a given evolutionary stage in a galaxy [57].

Chemically homogeneous evolution

Another competing formation scenario has been proposed at the time GW150914 was discovered [12]: the chemically homogeneous evolution scenario. This channel proposes a solution for stars assembled in binaries to convert most of their mass into the final black hole, thus explaining the population of high-mass stellar black holes.

Consider two massive hydrogen burning stars orbiting their center of mass with a period of few days (almost a contact binary). When being so close to each other, each companion experiences tidal effects from the other companion and each fills its Roche Lobe partially. The deformation by tides triggers some hydrodynamic instabilities (Eddington-Sweet instability [59]) in the inner structure of the stars. Both companions become tidally locked so that the whole binary is synchronised: the orbital period and the rotation period get close. As a result each component is rotating at break-up velocities. Tidal interactions in addition to an important rotation engender an efficient mixing of nuclear burning materials from the core to the envelope of the stars. The overall mechanism thus prevents a star from having an "onion layers structure" with burning hydrogen in the core and inert helium in the envelope. Instead chemical species are mixed. Nuclear reactions are maintained on longer time scales than for an isolated main sequence star and it attenuates the shrinkage/ expansion stages a single star generally experiences. None of the two stars fills totally its Roche lobe which avoid mass transfers even in a tight orbit configuration. Moreover the still low metallicity of the medium prevents the star from losing

mass driven by stellar winds [52]. After core hydrogen exhaustion both stars evolve to the SN stage the less massive star after the other. Contrary to the common envelope scenario, the kicks provided by the supernova explosions are not sufficient to impact the binary orbit due to the high orbital velocity [60]. The chemically homogeneous scenario leaves a pair of black holes which will merge within Hubble time even if this duration strongly correlates with metallicity [61]. The whole evolution is schemed on Fig 2.6.

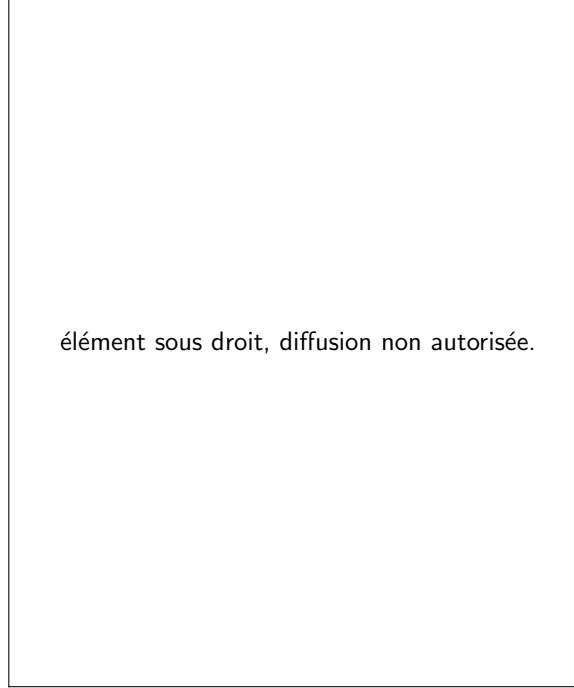


Figure 2.6: Evolution diagram of a high-mass binary star through the chemically homogeneous formation channel. The two stars experience tidal effect from each other which prevents any Roche Lobe overflow. Numbers in red indicate the objects mass at each stage of their evolution [61].

These two main formation channels could explain the high mass binary populations observed during Laser Interferometer Gravitational Wave Observatory (LIGO) first science run.

2.2.4 GW emission from compact object binaries

Compact object binaries are by far the most frequent sources expected in Earth based instruments detection bandwidth. The high-mass binary evolution scenarii evoked previously eventually ends with two orbiting compact objects. It has now been largely explained that within the framework of GR, a system composed of two objects orbiting each other emit GW. The emission is accompanied by a loss of energy and angular momentum for the earlier initial moments of the coalescence where the two objects are far apart: the *inspiral phase*. This explains a predicted tendency of the orbit to decrease and circularise during this phase. As seen in chapter 1 this phase dominates the orbit and is well described by the Post-Newtonian formalism [62] where each object is modelled as a point-like source and introducing slight perturbations of the space-time metric. While the objects get closer the orbital frequency increases (so do the GW signal frequency and amplitudes) and tidal interactions are now so strong that relativistic and tidal effects become dominant until the objects collide during the *merger phase*. At this point it is required a full integration of EFE with numerical tools, named *numerical relativity* [63]. At the end of the merger phase the two compact bodies are in a non-equilibrium state where the two horizons touch each other. The final phase called the *ringdown phase* consists in a relaxation of the distorted BH described by the *quasi-normal mode* formalism [64]. It results in the formation of a new stable compact object.

An expression for the GW emission from a circular or eccentric orbit is directly given by Eq (2.20) and Eq (2.21) at Newtonian order. The given expression can in fact be re-expressed in term of the *chirp mass* \mathcal{M} which governs the frequency evolution of the chirp signal at lowest (Newtonian) order



Figure 2.7: GW150914 signal reconstructed (grey) and predicted (red) along with the stage of the orbit [12].

$$\mathcal{M} = \frac{(m_1 m_2)^{3/5}}{(m_1 + m_2)^{1/5}} = \frac{c^3}{G} \left[\frac{5}{96} \pi^{-8/3} f^{-11/3} \dot{f} \right]^{3/5} \quad (2.6)$$

where f is the observed frequency and \dot{f} is the frequency time derivative. In the circular orbit case, the GW frequency is the double of the orbital frequency and evolves in time according to

$$f = \frac{1}{\pi} \left(\frac{5}{256} \right)^{-3/8} \left(\frac{c^3}{G\mathcal{M}} \right)^{5/8} (t_c - t)^{-3/8} \quad (2.7)$$

where t_c is the coalescence time. From Eq (1.38) the two polarisations at Newtonian order are

$$h_+(t) = \frac{4G\mu\omega^2 a^2}{rc^4} \left(\frac{1 + \cos^2 \iota}{2} \right) \cos(2\omega t) \quad (2.8)$$

$$h_\times(t) = \frac{4G\mu\omega^2 a^2}{rc^4} \cos \iota \sin(2\omega t) \quad (2.9)$$

in the case of two compact objects with reduced mass $\mu = (m_1 m_2)/(m_1 + m_2)$ describing a circular orbit. In Eq (2.8) and Eq (2.9): a is the separation distance between the two objects, r is the luminosity distance of the source, ι is the orbital plane inclination angle with respect to the observer's line of sight and ω is the orbital frequency.

At Newtonian order the chirp mass drives the time-frequency evolution of the signal. But other physical quantities drive the phase evolution such as the component spins and eccentricity. All carry some information on the formation process of the compact binary. For instance, the spin components orientation with respect to the orbital angular momentum is likely to tell us whether the binary has formed in galactic field or through dynamical formation. If the binary has formed isolated then the spins are aligned with respect to the orbital angular momentum via the *Bardeen-Petterson effect*, [65] whereas if the binary form in a dynamically hot environment the spins are affected by the surrounding tidal effects and do not have time to align. It appears the non-aligned spins scenario is preferred according to all the recent detections but GW151226 [19].

2.3 Gravitational waves from eccentric binaries

In this section we are interested in how *eccentric binary black hole* (eBBH) emerge from dense stellar environments and what are the expected merger rates as those sources remain undetected. Along the other chapters of this thesis we focus the discussion on how the eccentricity affects the phase evolution of the GW signal.

2.3.1 Formation channels

Compact binary objects are commonly assumed to orbit each other in a circular motion. This assumption is justified by the fact eccentric compact binaries are expected to circularise before they merge [66]. However there exist astrophysical phenomena and environments that can lead to significant orbital eccentricity at the merger. The binary history and its interactions with neighbouring objects determine its orbital motion and in particular how it deviates from the circular orbit. Several scenarios lead to elliptic orbits during the late phases of the coalescence. These formation channels involve high stellar density media such as galactic cores or globular clusters.

Searching for those systems is a promising source as it would be very informative on the dynamics of densely populated astrophysical environments. Furthermore, the observation of an eccentric BBH merger would inform BH population models. From the point of view of the GW signal the presence of higher order mode will probe the strong field regime of GR.

A first formation channel is via hierarchical triplets composed of field massive stars. The differential inclination between the two orbit planes causes variations of the tidal forces between the triplet components. It impacts the dynamics of the whole system and finally induces some oscillations in the eccentricity of the inner binary. This effect is known as the *Kozai-Lidov mechanism* [67, 68, 69]. These triple systems are supposed to be rare with $0.3 - 1.3 \text{ Gpc}^{-3} \text{ yr}^{-1}$ merger events [70]. They lead to oscillating values of the eccentricity and the inclination angle as the two binaries exchange angular momentum. When the inner stellar mass binary is located close to a massive third component (typically a *supermassive black hole binary* (SMBHB)), the effects of the Kozai-Lidov mechanism amplify the eccentricity oscillations and could lead to very high eccentricities. Around 0.5% of the eccentric binaries that merge close to the *supermassive black hole* (SMBH) enter the LIGO/VIRGO observational window with a very high eccentricity $e \geq 0.5$ [71]. The majority of the stellar mass binaries (99% of them) will have eccentricity below $e = 0.1$ when the orbital frequency reaches 10 Hz (see Fig 2.8). There thus are two coexisting populations of stellar mass BH binaries.

The second mechanism also involves a SMBH with mass $10^5 - 10^6 M_\odot$, located at the center of a Milky-Way-like galaxy. Such an object creates a density cusp which favours runaway encounter processes when two black holes come close to each other. Although stellar mass BHs are not expected to emit light, their presence in the Milky-Way center is established by population models but also by electromagnetic observations of the galactic center and its vicinity in the X-ray wavelength [72]. If during a BHs encounter, a sufficient amount of energy is radiated away in the form of GW, then a bound system may form. If this binary merges within a few hours timescale the orbit will not have time to circularise. In the case of Milky-Way-like galaxies the progressive segregation of stellar mass BHs towards the galaxy cusp can concentrate around 20,000 BHs within the last parsec of the central SMBH⁸ [73]. Due to the important density of compact objects in the galactic core, the merger rate is far more important for this formation channel as $1 - 50 \text{ Gpc}^{-3} \text{ yr}^{-1}$ mergers are anticipated. As seen in Chapter 1, the presence of residual eccentricity causes the binary to merge faster and hence lead to an increased merger rate. Once assembled in yet eccentric binaries it is thought they further segregate to the accretion disk around the central SMBH in less than 10 Myr [74]. During this migration the orbital motion circularises and the binary finally merges within 1 Myr. This formation model thus also explains the BBH sources detected so far by LIGO (with an estimated event rate of $12 - 213 \text{ Gpc}^{-3} \text{ yr}^{-1}$ [75]. An eBBH formed in a galactic core is expected to have eccentricity larger than 0.9 at the time its orbital frequency is 5 Hz [76].

A third possibility involve globular cluster (GC), *i.e.* old cluster of stars orbiting a galactic core. Evolving within a GC, BHs become the most massive objects within the first few million years of GC evolution [77]. With the intern dynamical friction BHs progressively segregate in toward the center of the cluster in the same way as in the galactic nuclei. There, they can also interact and form binaries with residual eccentricity. The process concerns single-binary and binary-binary encounters that eventually merge. The encounter rate density is proportional to $\mathcal{R} \sim \int dV \langle n_*^2 \rangle \sigma_{cs} v$ where n_* is the stellar number density, $\sigma_{cs} \sim GMb/v^2$ is the capture cross section, M is the total mass, b is the impact parameter, v is the typical velocity dispersion. Monte-Carlo methods estimate a merger rate of $\sim 5 \text{ Gpc}^{-3} \text{ yr}^{-1}$ [78]. The studies reveal that the initially more massive GCs (more massive than $10^6 M_\odot$) contribute significantly to the rates.

One could think of other ways for binary systems to gain or retain orbital eccentricity (in the galactic field or in clusters) like recycling objects via accretion or natal kicks associated to the end life of a high-mass binary but

⁸Both in globular clusters and galactic cores there is an equipartition of components kinetic energy due to the exchanged kinetic energy and angular momentum at each dynamic encounter. It results that the heavier binary component progressively segregates toward the SMBH.

the two previous channels are largely preferred to explain eBBH populations. The residual eccentricity of these sources, when they become visible to GW detectors, depends on their formation mechanism. Fig 2.8 shows the eccentricity distribution for globular clusters and galactic cores. Dynamical encounters occuring in galactic nuclei are associated to eccentricities $e \sim 1$. For this reason the solid curve extends to hyperbolic encounters for which $e \geq 1$ at the time the orbit reaches the last stable orbit frequency. Calculations undertaken in [73] confirm the previously given eccentricity values for the two environments.



Figure 2.8: Eccentricity distribution of simulated events in [73] occurring at the last stable orbit for a Milky-Way-like galactic nuclei (solid line) and a globular cluster (dashed line). [73]

2.3.2 GW emission from eccentric binaries

This section describes the expected waveform emitted by a pair of objects following an elliptic orbit. An elliptic orbit is a plane closed curve whose form deviates from a circular orbit. The deviation is quantified by a geometric parameter called the *eccentricity* denoted e which varies between 0 (circular limit) and 1 (unbound orbit). An intermediate case is shown in Fig 2.9.

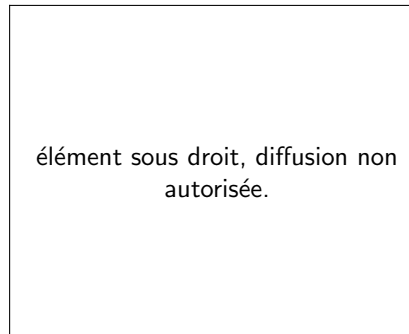


Figure 2.9: Scheme of an elliptic orbit with semi-major axis a , semi-minor axis b and eccentricity e . The point for which the distance to the focus F is minimal (resp. maximal) is called the *periastron* (resp. *apastron*).

An ellipse is characterised by a semi-major axis a , a semi-minor axis b which both correspond to the radius of the circle in the circular orbit case. The points (x, y) of the ellipse are defined by

$$\left(\frac{x}{a}\right)^2 + \left(\frac{y}{b}\right)^2 = 1 \quad (2.10)$$

where $e = \sqrt{1 - b^2/a^2}$. Eccentricity can also be related to the reduced mass, the orbital energy and the orbital angular momentum (see Eq (5.1)-(5.3) of [79]). Consider two point masses m_1 and m_2 describing an elliptic trajectory in a xOy (or (r, ϕ) in polar coordinates) plane with orbital frequency ω_0 . In a Cartesian (x, y, z)

frame the parametrised coordinates can be expressed as

$$x_0(t) = r(t) \cos \phi(t) \quad (2.11)$$

$$y_0(t) = r(t) \sin \phi(t) \quad (2.12)$$

$$z_0(t) = 0 \quad (2.13)$$

where $r(t) = r_2 - r_1$. A direct application of Eq (1.37) knowing that $\rho = T_{00}/c^2$ gives the non-vanishing components of Q_{ij} as a function of the reduced mass $\mu = (m_1 m_2)/(m_1 + m_2)$ and the orbital phase $\phi = \omega_0 t$

$$Q_{xx} = \mu r^2 \cos^2 \phi \quad (2.14)$$

$$Q_{yy} = \mu r^2 \sin^2 \phi \quad (2.15)$$

$$Q_{xy} = Q_{yx} = \mu r^2 \sin \phi \cos \phi \quad (2.16)$$

where $r(\phi) = a(1 - e^2)/(1 + e \cos \phi)$ is the radius of the center of mass. The next step is the computation of the second time derivative of each of the previous components of Q_{ij} . For this we will need an analytic expression for $\dot{\phi}$ and $\ddot{\phi}$. It is obtained by the generalisation of the third Kepler law for elliptic orbits. It leads to [66]

$$\ddot{Q}_{xx} = -\alpha (3e \cos \phi + 4 \cos 2\phi + e \cos 3\phi) \quad (2.17)$$

$$\ddot{Q}_{yy} = -\alpha (4e^2 + 7e \cos \phi + 4 \cos 2\phi + e \cos 3\phi) \quad (2.18)$$

$$\ddot{Q}_{xy} = \ddot{Q}_{yx} = \alpha (5e \sin \phi + 4 \sin 2\phi + e \sin 3\phi) \quad (2.19)$$

In the previous relation we defined $\alpha = Gm_1 m_2 / a(1 - e^2)$. finally, using Eq (1.38), the radiated GW polarisations as observed by an observer located at a distance r with an inclination angle ι with respect to the z axis (itself perpendicular to the orbital plane) are

$$h_+(t) = \frac{G^2 m_1 m_2}{arc^4(1 - e^2)} \left\{ \left(\frac{1 + \cos^2 \iota}{2} \right) [\zeta(e, \phi) \cos 2\Phi + \Xi(e, \phi) \sin 2\Phi] - (\sin^2 \iota) \Psi(e, \phi) \right\} \quad (2.20)$$

$$h_\times(t) = \frac{G^2 m_1 m_2}{arc^4(1 - e^2)} \cos \iota [\zeta(e, \phi) \sin 2\Phi - \Xi(e, \phi) \cos 2\Phi] \quad (2.21)$$

with the functions

$$\Xi(e, \phi) = 5e \sin \phi + \sin 2\phi + e \sin 3\phi \quad (2.22)$$

$$\zeta(e, \phi) = 5e \cos \phi + \cos 2\phi + e \cos 3\phi + 2e^2 \quad (2.23)$$

$$\Psi(e, \phi) = e \cos \phi + e^2 \quad (2.24)$$

and where Φ is the angle between the projection of the line of sight on the orbital plane and the major axis of the ellipse. The expressions Eq (2.20) and Eq (2.21) are also given in [80] or by Eq (11.78a)-(11.78b) in [81]. The GW polarisations following Eq (2.20) and Eq (2.21) are shown in Fig 2.10. We verify the quadrupole order expressions are recovered in the circular orbit limit, *ie.* when e goes to 0. At quadrupole order, the waveform contains three harmonics as compared to the uni-modal orbital frequency of the circular case. In this case the GW frequency is twice the orbital frequency. When $e \rightarrow 1^-$ and beyond the quadrupole order, the amplitude modulation visible on Fig 2.10 tends to a succession of peaks interpreted as repeated bursts of gravitational waves each time the masses reach the periastron [82]. This situation is quite close to parabolic or hyperbolic (hence un-bound orbits) encounters that are also associated to an emission of GW bursts. At this occasion the system loses energy and angular momentum and likely becomes bounded. Note the eccentric waveform length is shorter with respect to the circular case (see Table 1 in [83]). However the total energy of the signal is larger.

Substituting Eq (2.19) in Eq (1.41) gives the GW luminosity radiated by an eccentric binary system at quadrupole order (see Eq (16) and (17) of [79])

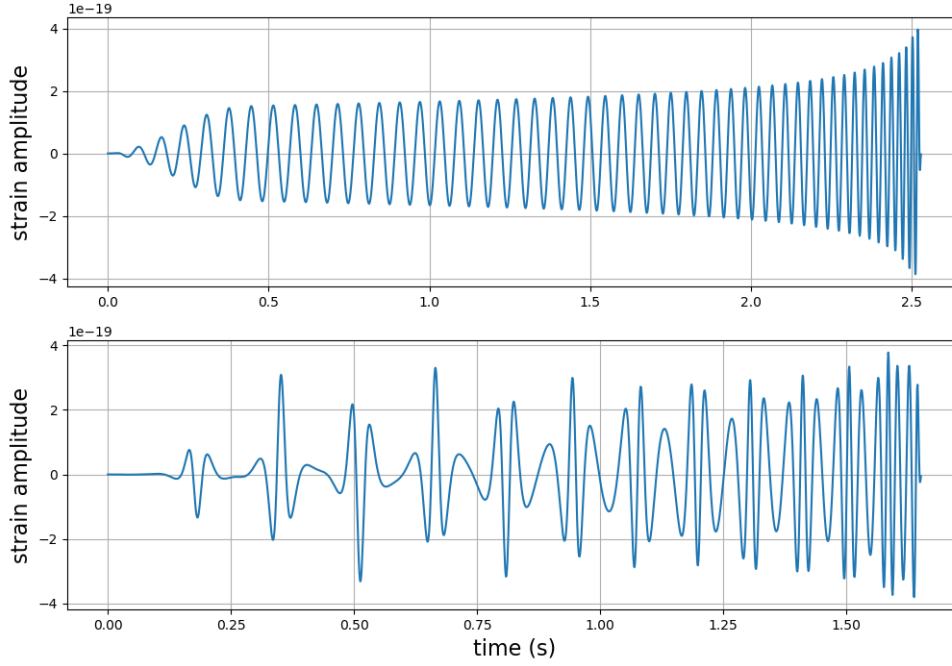


Figure 2.10: Plus polarization of a circular and eccentric binary system (with $e = 0.3$) of two $30M_{\odot}$ non-spinning black holes located at 1 Mpc. For the circular case we used a **TaylorT4** approximant [84] and for the eccentric case we used a **EccentricTD** approximant [85]. For both case the lower frequency cut is $f_{low} = 16$ Hz. A tapering window is applied that accounts from the fact the signal is generated at a particular lower frequency.

$$\left\langle \frac{dE}{dt} \right\rangle_{quad} = \frac{32G^4 m_1^2 m_2^2 M}{5a^5 c^5} f(e) \quad (2.25)$$

where $M = m_1 + m_2$. The dependence in ϕ has disappeared because of an average over many orbits. The eccentricity dependence in Eq (2.25) is stored in a monotonically increasing function $f(e)$

$$f(e) = \frac{1}{(1 - e^2)^{7/2}} \left(1 + \frac{73}{24}e^2 + \frac{37}{96}e^4 \right) \quad (2.26)$$

which measures the enhancement of the GW emission with respect to the circular case. For example, the Hulse & Taylor binary pulsar [86] presents a fairly large eccentricity ($e \simeq 0.617$) for which $f(e) \sim 11.8$. Emitted power is hence multiplied by a factor of ten⁹. Instead the circular case leads to $f(e) = 1$.

As GW are the consequence of a gravitational system losing energy, it is relevant to express the system *breaking law*, *i.e.* the rate at which the orbital period decays. Mass transfers that largely impact the eccentricity of the binary are not regarded. The system period T is linked to the proper pulsation $\omega_0 T = 2\pi$ and comes in the third Kepler law $GM = \omega_0^2 a^3$. Hence the combination of those two relations plus knowing that $a = GM\mu/2|E|$ gives the expression of the braking law \dot{T}/T .

$$\frac{\dot{T}}{T} = -\frac{3}{2} \frac{\dot{E}}{E} = -\frac{96\mu G^3 M^2}{5a^4 c^5} f(e) \quad (2.27)$$

For any system, it is clear from this relation that the orbital period decreases as the system emits GW since $\dot{T}/T < 0$. This relation is of tremendous importance since it is the basis for the first indirect proof for the existence of gravitational waves by Hulse and Taylor [86]. Other time-dependent physical quantities like the semi-major axis or the eccentricity are also affected by the decrease of the orbital period as demonstrated by [66, 79].

⁹It can even be a factor 100 if $e = 0.8$!

$$\left\langle \frac{da}{dt} \right\rangle_{quad} = -\frac{64}{5} \frac{G^3 m_1 m_2 M}{a^3 c^5} f(e) \quad (2.28)$$

$$\left\langle \frac{de}{dt} \right\rangle_{quad} = -\frac{304}{15} \frac{G^3 m_1 m_2 M}{a^4 c^5} \frac{e}{(1-e^2)^{5/2}} \left(1 + \frac{121}{304} e^2 \right) \quad (2.29)$$

These two relations highlight an important fact: eccentric binaries tend to circularize. Indeed both derivatives in Eq (2.29) are negative and the eccentricity finally vanished when a is confounded with the radius of the innermost stable circular orbit. The eccentricity of a binary system is thus monotonically decreasing. To characterize the orbital eccentricity of a binary system, we use its eccentricity at a reference orbital frequency (typically the last stable orbit frequency as shown on 2.8).

We conclude the present section by pointing out the fact that we considered so far an unimodal oscillatory motion for the center of mass from which we arrived to a multi-modal GW emission. A more general description consists in regarding the trajectory as a superposition of weighted oscillations or orbital modes. The parametrized trajectory of the center of mass is then written as a Fourier expansion. An analogous derivation gives another form for the eccentricity dependent term [66]

$$g(n, e) = \frac{n^4}{32} \left\{ \left[J_{n-2}(ne) - 2eJ_{n-1}(ne) + \frac{2}{n}J_n(ne) + 2eJ_{n+1}(ne) - J_{n+2}(ne) \right]^2 + (1-e^2) [J_{n-2}(ne) - 2J_n(ne) + J_{n+2}(ne)]^2 + \frac{4}{3n^2} J_n(ne)^2 \right\} \quad (2.30)$$

where we denoted by n the n^{th} harmonic, by J_n the n^{th} order Bessel function of the first kind and where $f(e)$ acts as a normalisation constant over the modes $\sum_{n=1}^{\infty} g(n, e) = f(e)$. Each mode contribution at chosen eccentricity values are shown in Fig (2.11). The curve peaks become wider with increasing eccentricities which means more orbital modes are needed to faithfully describe the orbital motion. In the circular case limit, the only emission comes from the fundamental mode ($n = 2$ harmonic) whereas the high eccentricity case need numerous harmonics to be fully described. Another interesting aspect is the relative importance of the modes: an orbital mode can be associated to a large coefficient for a given eccentricity and is almost insignificant for another value. For instance the $n = 2$ mode contribution is less than any other harmonic at $e = 0.7$ while it contributes a lot for low eccentricity values.

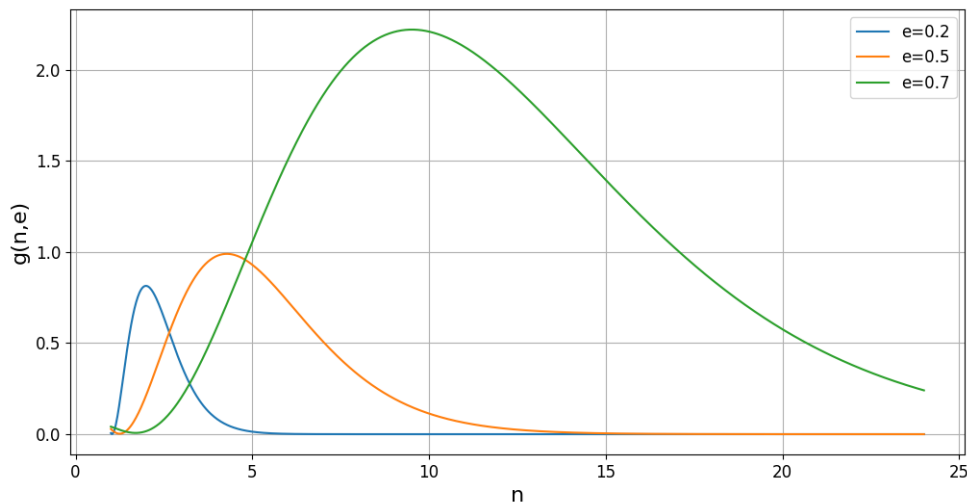


Figure 2.11: Plot of Eq (2.30) as a function of the n^{th} harmonic for eccentricities $e = 0.2, 0.5, 0.7$.

We will develop a search for GW from eccentric binary systems in chapter 6 of this thesis.

Chapter 3

Gravitational wave interferometric detectors

Contents

3.1 Basics of interferometry and main noise contributions	39
3.1.1 Laser interferometry in a nutshell	39
3.1.2 Limiting noises	41
3.2 Network of detectors	41
3.2.1 On the importance of detector networks	41
3.2.2 Second generation detectors	43

We have seen that GW are metric perturbations propagating at the speed of light. If compared to a material, space-time is particularly stiff mainly because of the smallness of the G/c^4 factor in EFE [87]. It is challenging to measure so tiny variations even for recently developed ground based experiments.

The present chapter will give a sense of the effort that has been deployed to detect GW until laser interferometry techniques and how a whole network of gravitational wave observatories can contribute to the new era of GW astronomy that has just opened.

3.1 Basics of interferometry and main noise contributions

Since Einstein prediction in 1916, a lot of efforts were pursued to detect GW. Two strategies were considered: resonant bars and laser interferometry. The former idea emerged with J. Weber in the 60s [88]. He designed resonant cylinders that an incoming GW signal whose frequency sits in the cylinder's bandwidth would then make resonate. However, despite his first claim in 1969, he did not succeed in detecting any real GW event. In 1962, M. Gertsenshtein and V.I. Pustovoit [89] had proposed the concept of what is nowadays known as a laser interferometric detector. Ten years after, Moss, Miller, Forward [90] and Weiss [91] developed the idea in details and first prototypes were built.

3.1.1 Laser interferometry in a nutshell

The first chapter pointed out the two polarizations of a gravitational wave as the consequence of a gauge invariance. However we have not discussed yet the effect GW have on matter. The fact is that within the Lorenz and TT gauges a free falling test-mass do not move when a GW passes [92]. In other words a GW does not affect the position of a body when the motion is studied in the gauges discussed earlier. Instead a GW modifies the distance between a pair of test-masses: a GW will stretch space-time in a differential way. This very particular feature is exploited in GW detectors. Let us consider again the configuration of Fig 1.1. When a GW propagates perpendicularly to the ring it will modify the relative distance between two test masses at the wave frequency with opposite effects in the orthogonal directions.

It is thus possible to detect a GW by measuring the relative change of distance between two orthogonal directions. Today the most common and accurate techniques to measure distances rely on laser interferometry. In nowadays

experiments the instrument configuration conjugates the use of power lasers along with two orthogonal arms in a so called *Michelson interferometer* [93] as shown on Fig 3.1.

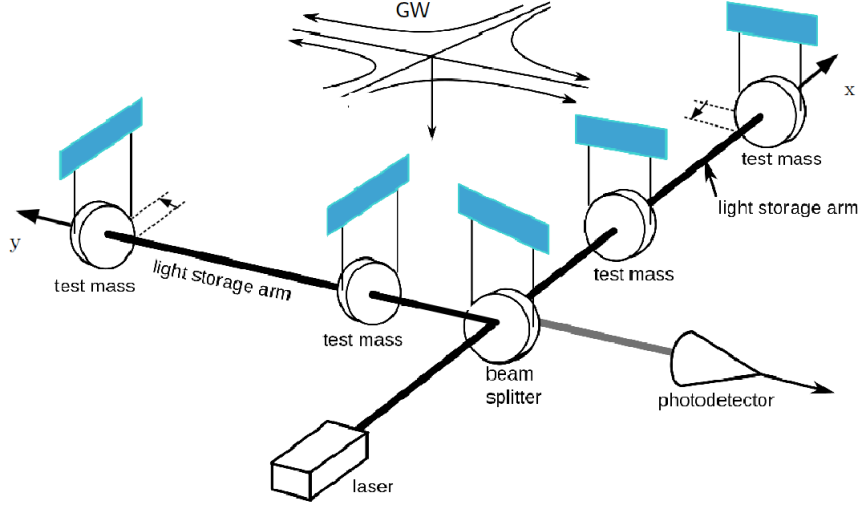


Figure 3.1: Simplified Michelson interferometer scheme. A “+”-polarized GW is reaching the instrument and causes a relative displacement of the test masses.

A Michelson interferometer is composed of two orthogonal arms with same length L . At the end of each arm a mirror plays the role of a test-mass in free-fall, *ie.* no other force than gravity must act on mirrors. For this reason they are isolated from any environmental noise. A laser beam enters the interferometer and is split into two beams of equal intensity. Each of the two travels the distance separating the beam splitter and the test mass in their respective interferometer arm. When a laser beam reaches the test-mass it is reflected. After a full round-trip the two beams are recombined and the phase difference is finally inferred from the intensity of the resulting beam. In the case where no GW is crossing the instrument the local space-time is flat (Minkowski spacetime) the interferometer is set up so that the two laser beam interfere destructively. If a GW passes then the differential effect of the GW induces a phase variation between the two beams which reflects a difference in the optical paths followed by the two laser beams.

In the TT gauge the distance in the perturbed space-time metric around the interferometer is

$$ds^2 = g_{\mu\nu} dx^\mu dx^\nu = -c^2 dt^2 + [1 + h_x^{TT}(t)] dx^2 + [1 + h_y^{TT}(t)] dy^2 \quad (3.1)$$

Light follows light-like geodesics and the previous equation must hence verify $ds^2 = 0$. If we now focus only on the two test masses disposed along the x-axis the relation reduces to

$$dt = \frac{1}{c} \left[1 + \frac{1}{2} h_+^{TT}(t) \right] dx \quad (3.2)$$

at first order in h_+^{TT} . At time t_1 a laser beam crosses the beam splitter and at time t_2 it arrives on the test mass at the end of the arm. The integration leads to

$$\delta t = t_2 - t_1 = \frac{L}{c} + \frac{1}{2} \int_{t_1}^{t_2} dt' h_+^{TT}(t') \quad (3.3)$$

In the limit where the GW strain amplitude is constant during the time interval, *ie.* if the GW wavelength is larger than the distance between the two mirrors then:

$$\frac{\delta L_x}{L} = \frac{1}{2} h_+^{TT}(t) \quad (3.4)$$

where δL_x (resp. δL_y) denotes the relative change along the x-axis (resp. y-axis). Since $\delta L_y/L = +(1/2)h_y^{TT} = -(1/2)h_+^{TT}$. The resulting arm length difference is

$$\delta L(t) = \delta L_x - \delta L_y = h_+^{TT}(t) L \quad (3.5)$$

It should be emphasized that the $h_+^{TT}(t)$ quantity in Eq (3.4) is the only measured quantity by a given instrument¹ and one cannot disentangle the two GW polarisation modes h_+ and h_\times with a single detector. Knowing that the GW strain amplitude when reaching the Earth is $h \sim 10^{-21}$ (for a typical coalescing binary) and the typical length of a ground based detector is $L \sim 1$ km. An estimation of the variation distance that has to be measured leads to $\delta L_x \sim 10^{-18}$. Detecting a GW is then a real challenge since the signal to identify has an amplitude which is a thousand times smaller than the atomic nucleus radius.

3.1.2 Limiting noises

Given their exquisite sensitivity, GW detectors are sensitive to any disturbances coming from the environment or from the instrument itself. Those disturbances are undesired contributions to the measured signal generically called *noises*. Three main noises fundamentally limit the measurement sensitivity.

- **The seismic noise** is a *displacement noise* that results from vibrations of the ground below the instrument. These vibrations are created by both the global motion of tectonic plates, the surrounding anthropic activities or weather. It mainly limits the instrument sensitivity towards low frequencies (below 10 Hz). The implemented solution in current interferometers to temper this type of noise is to use suspension systems. In this way, optics are mechanically isolated from the environment thanks to a set of suspended pendula which act like low-pass filters.
- **The thermal noise** is a displacement noise due to the Brownian motion of the atoms that compose the mirrors and the suspensions. Usually the effect can be tempered using high quality factor material (fused silica fibres for suspension and fused silica substrates for the mirrors). Thermal noise is important for the detection since it affects frequencies around 100 Hz, where the interferometer sensitivity is the best.
- **The shot noise** is a *sensing noise* that arises from the quantum nature of light. The photons impinging the output photodiode are discrete and independent events following a Poisson statistic. The statistical fluctuation in the number of photons per unit of time impinging the output photodiode leads to an uncertainty in the measurement of the output light power which is called *shot noise*. This uncertainty on the interference pattern translates into an uncertainty in the measurement of the strain amplitude caused by a GW. This noise scales inversely with the square root of the input laser power.

The previous list dealt with noises inherent to the physics of the detector which can only be mitigated. On the contrary, other noise contributions called *technical noises* are due to the instrument design: scatter light, ... Many of them will be (at least partially) addressed by some technological upgrades planned for future generation interferometers. Those upgrades include for example: an increase in the input laser power and the installation of frequency (in)dependant squeezing.

3.2 Network of detectors

Many Michelson laser interferometers are actually monitoring the passage of a gravitational wave signal. All individually record the phase variations coming from their photo-diodes and are put together to constitute a real array of GW detectors. We briefly detail the reasons why many instruments are combined and the status of the actual and future ground and space based instruments.

3.2.1 On the importance of detector networks

The derivation presented in section 2.1.1 included the "+"-polarization only. The inclusion of the second polarization must account for the GW source position in the sky (hence the detector position and orientation on Earth) and the source polarisation angle. The response $h(t)$ of a detector to an incoming GW sky and time coverage is expressed as

$$h(t) = F_+(\theta, \phi, \psi) h_+(t) + F_\times(\theta, \phi, \psi) h_\times(t) \quad (3.6)$$

where θ is the polar angle, ϕ is the azimuthal angle and ψ is the polarization angle as shown on the left part of Fig 3.2. Functions F_+ and F_\times are called the *antenna pattern functions* and encode the detector angular sensitivity. Their expression can be found in Eq (7.271) of [9].

¹Technically it is the interference pattern as detected by a photo-diode (see Fig 3.1) which encodes the $h(t)$ information. The pattern is itself created by the existing phase difference between the two laser beams.

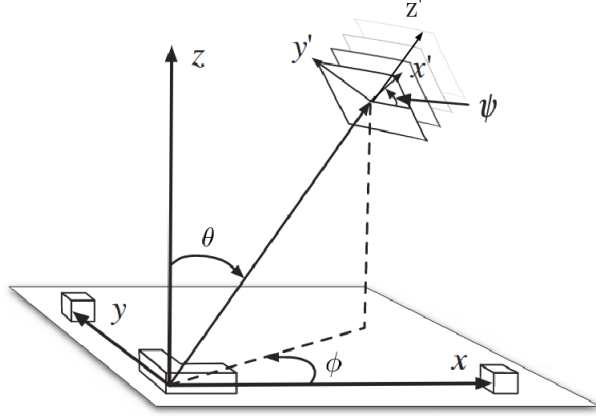


Figure 3.2: (left) Coordinate system used in the computation of the antenna pattern functions. The origin of the system coincides with the beam splitter (see Fig 3.1). Rotations around the axis y by an angle θ and around the axis z by an angle ϕ brings the (x', y', z') frame to match the (x, y, z) frame. Black segments lying in the xy plane correspond to the interferometer arms. (right) Antenna pattern functions F_+ , F_\times and $F_+^2 + F_\times^2$ (from left to right).

Detector antenna pattern functions in Eq (3.6) translates the fact that GW detectors have a very wide aperture and are non- directional. It means that contrary to conventional telescopes one cannot point to a specific location in the sky. It also follows that GW detectors are blind to certain directions that correspond to the two bisector directions of the two detector arms ($\phi = \pm\pi/4$ and $\theta = \pi/2$). Inversely the detector has a maximum sensibility for a GW arriving from the zenith ($\theta = 0$) and the opposite direction ($\theta = \pi$).

Consequently a complete coverage over the celestial sphere requires a network of detectors. There are several other advantages with having multiple instruments organised in a network:

- **Sky location** : A single detector poorly constraints the source position in the sky. Then if one imagines an ideal source located on the bisection plane of two detectors, then the GW will reach each detector at exactly the same time. The intersection between a plane and the celestial sphere being a circle, two detectors delimit a circle which can be again constrained thanks to the GW amplitude information. Finally three detectors enables to perform a *source triangulation* of the arrival times. Each pair of detector thus provide a cut circle on the sky and the three two by two intersections ideally gives a two mirror points localisation of the source.
- **Duty cycle improvement** : Each detector is subject to an entire zoology of noises that jeopardise the full time detector operation. The loss of duty cycle arises because of instabilities of the instruments causing the loss of control of the interferometer on its working point. Having several detectors increases the chance of having at least one running detector.
- **Detection confidence** : The GW signal is the only common signal received by all the detectors in the network. Indeed the GW signal is buried in some noise fluctuations which are supposed to be uncorrelated from one detector to the other. Identifying the same GW signature in the data generated by independent detectors allows us to gain confidence in a detection. The confidence we gain is all the more important there are numerous instruments with comparable sensitivities in the network.
- **Polarization constraint** : GR predicts the existence of two tensor polarisation modes. From the observational point of view, Eq (3.6) is observed differently by each detector due to the antenna pattern functions. It means every detector do not respond optimally to the GW signal from a source at a given sky position. It is impossible to retrieve the GW polarization modes with a single detector. At least two non aligned detectors are needed to retrieve h_+ and h_\times . If two detectors are (quasi-)aligned then they have (almost) the same response. In the opposite case one has a system of two independent equations with two unknown quantities. And having even more detectors has the advantage of further constraining both the nature and the polarisation of the GW polarisation modes. Other theories of gravitation beyond GR also predict GW with a mixture of polarization types (scalar, vector and tensor modes) [94]. So having a network also allows to constraint GR.

3.2.2 Second generation detectors

In the late 1990s a first generation of interferometric detectors have been operated and initially included five instruments. The twin US- based LIGO detectors [95] in Handford, WA and Livingston, LA; the French-Italian experiment VIRGO [96] located near Pisa, Italy; the German-British detector GEO [97]² located close to Hannover, Germany; and the TAMA300 interferometer [98] in Mitaka, Japan. Six science data takings ran between 2002 and 2011.

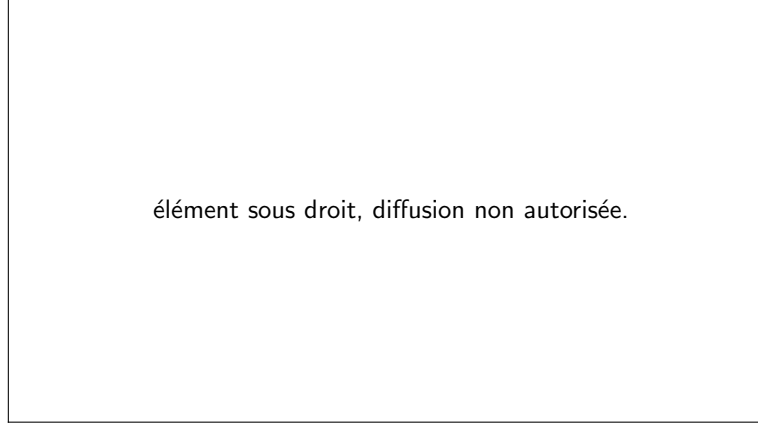


Figure 3.3: Map of the worldwide network of Earth based interferometer of first and second generation. [20]

Those runs provided no GW detection and the planned upgrade of the instruments was undertaken with the help of the most recent technology developments. The aim was to increase again the sensitivity of first generation instruments of one order of magnitude in observable distance. This would have resulted in a 1000 times larger volume of observable universe, thus of the rate of GW detections.



Figure 3.4: Regions of ADVANCED LIGO (*left*) and ADVANCED VIRGO (*right*) target strain sensitivities as a function of frequency. The binary neutron star range (*i.e.* the average distance to which these signals could be detected) is indicated in megaparsec in the legend. [99]

The two ADVANCED LIGO detectors [100] had their installation started in 2011 and did their first scientific run (called O1) from September 2015 until January 2016. During this first run the two instruments had a sensitive range of 1.3 Gpc for a 10 - 10 M_{\odot} binary black holes and 80 Mpc for binary neutron stars (see Fig 3.4). This was a factor 3 improvement in sensitive distance with respect to the initial LIGO instrument. The

²Although it is far less sensible then other ground based detectors GEO is indispensable as it is used as a pathfinder for last interferometric developments. Its sensitivity is comparable to other detectors in restricted parts of the GW spectrum.

second run (named O2) occurred between November 2016 and August 2017. The ADVANCED VIRGO [101] instrument joined the observation during the last month. The construction of VIRGO started in 2012 and many commissioning periods lead to the upgraded Advanced VIRGO instrument. The detector ran during the full month of August 2017 aside the American instruments with a BNS sensitive range of 27 Mpc. This was made possible thanks to many technological upgrades on the initial VIRGO: monolithic suspensions, mirror coating improvements, installation of many light absorbers (to reduce scattered light emission), heavier mirrors (reduce radiation pressure noise), enhanced Fabry-Perot cavities finesse and others. An additional LIGO INDIA instrument is planned for the year 2024 which will be built on the north-west part of India [102]. The japanese instrument TAMA demonstrated the feasibility of an underground instrument with cryogenic sapphire mirrors called KAGRA. KAGRA is expected to reach, between 2018 and 2020, a sensitivity sufficient to participate to the next observing runs of LIGO and VIRGO [103, 104].

Chapter 4

Gravitational wave transient searches

Contents

4.1	Searches for continuous GW sources	45
4.1.1	Continuous waves	45
4.1.2	Stochastic GW background	46
4.2	Searches for GW transient sources	47
4.2.1	Known signal model: matched filtering	47
4.2.2	Unmodeled signals: generic transient searches	51
4.2.3	Event significance	57
4.2.4	Limitations of current searches	58

Gravitational wave interferometers measures the strain GW amplitude $h(t)$ due to the relative change in length of the instrument arms. The detection of gravitational waves then consist in extracting the GW signal from noisy data collected by an array of observing sites. It is made possible by efficient data analysis techniques applied to interferometric data. Two main strategies are employed when searching for GW transient signals which lead to an interesting complementarity regarding targeted sources and searches sensitivities. Modeled searches rely on an *a priori* knowledge of the targeted signal phase provided by general relativity. On the contrary, unmodeled searches make no assumption on the GW emission and take advantage of having a network of GW detectors.

In the first part we briefly describe the methods used to detect long duration signals in LIGO-VIRGO. In the second part we detail how modelled and unmodelled searches provide robust ranking statistics together with the sky location and the characterisation of the GW source. *Coherent WaveBurst* (cWB) is introduced as a typical detection pipeline for unmodelled GW transient search for generic emissions of gravitational waves. Finally we look more closely at the current limitations of modeled searches.

4.1 Searches for continuous GW sources

The Hulse and Taylor binary pulsar [86] provided the first observational evidence for the existence of GWs emission. Radio pulses received from this system are in very good agreement with the predictions from GR. This demonstrates that compact binary systems are a good example of gravitational wave source candidates. Many astrophysical systems are expected to emit GW in the LIGO and VIRGO frequency bandwidth. The present section aims at describing main families of sources and their associated searches. Many of them remain to be detected.

Four categories of GW sources are distinguished. The taxonomy relies on the time duration of the GW emission process and the level of understanding of the source modelling. Such a classification is summed up in Fig 4.1. This thesis is about transient searches. Before moving to the main topic, we briefly review the searches for continuous sources.

4.1.1 Continuous waves

A continuous emission of GW is expected from populations of NS that present a certain degree of asymmetry. NS likely form with an important angular momentum resulting from the initial nagular momentum of the source

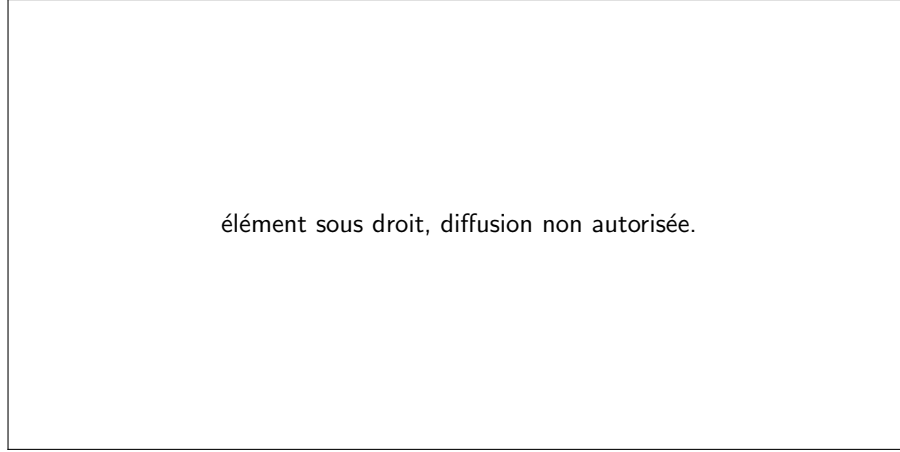


Figure 4.1: Classification of GW searches based on the emission duration and the degree of knowledge for their associated target signal [105].

and from the supernova explosion. During the initial matter collapse the radius of the star suddenly decreases and it results in a rotational kick. The back-of-the-envelope estimate (1.39) of the GW strain amplitude emitted by a generic source evidenced the importance of a minimal degree of asymmetry ϵ . If a source exhibits a deviation from spherical geometry ¹ then it can be a good GW source. For instance, one can imagine a "mountain" at the surface of a NS caused by its internal dynamic. Then all the ingredients of Eq (1.39) are present to obtain a detectable GW emission by current instruments.

$$h \sim 6 \times 10^{-25} \left(\frac{f}{500 \text{ Hz}} \right)^2 \left(\frac{r}{1 \text{ kpc}} \right)^{-1} \left(\frac{\epsilon}{10^{-6}} \right) \quad (4.1)$$

Another possibility that could generate such degree of asymmetry is the existence of strong internal magnetic field lines which rearrange [106]. The emitted GW signal is purely monochromatic with a GW frequency being twice the rotation frequency. Although the order of magnitude of the strain amplitude is too weak the quasi-periodic signal can be integrated over long periods to be detected. Luckily NS are among the most compact objects supposed to emit light and a coincident detection of an isolated rotating NS in the γ -ray, X-ray or radio domain would tell us more on their equation of state while gaining confidence on the detection. Dedicated searches take advantage of considering a mono-chromatic GW emission that results in a peak in the frequency domain. Continuous emission of GW have not been detected during the O1 and O2 science runs but upper limit on their signal amplitude have been derived [107].

4.1.2 Stochastic GW background

A stochastic background of GW is postulated from two possible origins. First, an astrophysical background of GW can arise from the incoherent superposition of many unresolved and uncorrelated GW sources. This background is predicted to be Gaussian and isotropically distributed [108]. Its discovery would provide precious informations regarding the initial mass function ², star formation history at the Galactic scale and allow to place constraints on the merger rate of compact objects.

Secondly, there may exist a GW background of cosmological origin from the very early phases of the Universe. Some cosmological models predicts an early epoch of the Universe where quantum fluctuations, phase transitions, cosmic strings and topological defects [109] could contribute to a stochastic background of gravitational waves. Its detection would discard some of the numerous inflation models.

When dealing with a stochastic signal a common approach consists in estimating its power spectrum [110]. A similar relation as Eq (1.40) can be established for the GW energy density denoted $\rho_{GW} = c^2 \langle \dot{h}_{ij} \dot{h}^{ij} \rangle / 32\pi G$. Thus the energy density of a GW stochastic background scales as $h^2 f^2$ where the factor f^2 comes from the

¹Often astrophysical objects are self gravitating structures whose geometry is very close to a sphere.

²The initial mass function of a population of stars is the initial distribution of masses at the moment they enter the main sequence

derivatives in the expression of ρ_{GW} . However this estimate implicitly suppose a flat spectrum where all frequency modes are of equal importance. For an arbitrary spectrum we replace the f^2 contribution by $f^2 S_{gw}(f)$ where $S_{gw}(f)$ is the energy density per unit frequency. Taking account of the multiple directions of emission one arrives to

$$\frac{d\rho_{gw}}{d\ln(f)} = 4\pi^2 f^3 S_{gw}(f) \quad (4.2)$$

To obtain a quantity that can be compared to other cosmological energy densities such as $\Omega_{rad}, \Omega_{\Lambda}, \dots$ we pose

$$\Omega_{gw}(f) = \frac{1}{\rho_c} \frac{d\rho_{gw}}{d\ln(f)} = \frac{4\pi^2}{3H_0^2} f^3 S_{gw}(f) \quad (4.3)$$

where $\rho_c = 3H_0^2/(8\pi)$ is the critical energy density and H_0 is the Hubble constant. From the already very precise determination of cosmological parameters obtained from cosmic microwave background experiments, we know that Ω_{gw} should be less than 10^{-5} . It is searched for a stochastic GW background by looking at cross-correlation of the observed signal by an array of GW observatories. No background of cosmological nor astrophysical origin have been found during the first observation run.

It is expected that the GW astrophysical background that LIGO/VIRGO may eventually detect will be dominated by the population of BBH mergers observed so far. The contribution from eccentric binaries is not anticipated to be significative. Studies with neutron star binaries reveal that eccentricity would have an effect on the stochastic gravitational wave background within the Laser Interferometer Space Antenna (LISA) frequency band [111, 112]. The effect tends to be more pronounced in the high eccentricity limit and higher harmonics affect more significantly the background.

4.2 Searches for GW transient sources

4.2.1 Known signal model: matched filtering

Astrophysical objects presented in chapter 3 are the most likely sources expected to lie within the frequency range where the sensitivity of ground based instruments is best (50 Hz - 2 kHz). The frequency dependence of the sensitivity is characterised by the noise *power spectrum density* (PSD). In practice, the PSD is estimated using Welch-based methods, that is averaging the energy of a signal in the frequency domain over many chunks of a data segment.

The instrument noise defines a frequency range of few kHz where gravitational waves can be observed. For this reason, LIGO and VIRGO data have a sampling frequency $f_s = 16$ kHz. Once sampled, data band passed so as to restrict the frequency bandwidth to the most sensitive part, then it is scaled to the noise level (details are found in the section dedicated to cWB). The PSD curve exhibits strong spectral lines which are of instrumental origins. e.g. the mirror pendulum mechanical resonances, calibration lines and others. They are avoided in some analyses by using analytical fits of the measured PSD.

Noise assumptions

The problem of characterising instrumental noise is not an easy task as the underlying hypotheses would impact the science that is done with the data (detection, parameter estimation). A very wide definition (the one that is adopted here) of a noise is a signal component one is not interested in. It is superposed to the signal of interest $h(t)$ of astrophysical origin: $s(t) = h(t) + n(t)$ where $s(t)$ is the strain as measured at the output of the pre-processing step (see above lines).

The noise in GW experiments can be considered locally over time scales of minutes to hours as stationary and Gaussian. However those assumptions have limits:

- **Stationary** Noise statistical properties are supposed to be independent of time over periods of observations. In GW experiments, the noise level varies over long time scales (hour/days) because of slow changes

in the optics alignment for instance and/or day/night changes in the environment (weather, human activities); changes in the instrument configuration, ... This motivated the division of science runs into chunks where the sensitivity is relatively stationary.

- **Gaussian** Fundamental noises are essentially Gaussian distributed. However, technical noises due to numerous perturbations are at the origin of a non Gaussian components known as glitches.
- **Uncorrelated** Generally it is assumed that there is no source of correlated noise in a network of interferometers. However studies have shown that high magnitude earthquakes [113] or electromagnetic waves propagating in between the ionosphere and the Earth surface known as the Schumann resonance [114] may lead to correlated noises.

All of these hypotheses are supposed satisfied in what follows and detection strategies even profit some of them.

Matched filtering

With the current status of ground based GW interferometers noise $n(t)$ largely dominates whatever class of GW signal $h(t)$. The *matched-filtering* technique aims at finding a known signal in noise [115, 116]. Signal is known in the sense where data is compared to a set of signals called *filters* whose phase evolution is close to the embedded GW signal. In what follows we demonstrate how these filters are concretely used and how this technique leads to the definition of a detection statistic. The following demonstration is largely inspired from [9]. Consider a time-dependent function $K(t)$ called the *filter function* and define the scalar quantity \hat{s} as

$$\hat{s}(\tau) = \int_{-\infty}^{\infty} dt s(t - \tau) K(t) \quad (4.4)$$

where τ is initially set to zero for simplicity. It is assumed that the GW signal $h(t)$ is known. The goal is to find the optimal filter function that maximizes the *signal to noise ratio* (SNR). That is the reason why this technique is called matched filtering: the filter function is chosen to match the signal. The SNR is defined as S/N where S is the expected value of \hat{s} when the signal is present in the data at the instant τ and N is the root mean square value of \hat{s} knowing that the signal is absent. Let us assume the noise has a vanishing mean value, *ie.* $\langle n(t) \rangle = 0$, and this without any loss of generality since an appropriate change of variable can make the noise distribution centered on zero as long as the signal is stationary. The signal S is then

$$S = \int_{-\infty}^{\infty} dt \langle s(t) \rangle K(t) = \int_{-\infty}^{\infty} df \tilde{h}(f) \tilde{K}^*(f) \quad (4.5)$$

where we transformed the integrand to the frequency domain. By definition N is:

$$N^2 = [\langle \hat{s}^2(t) \rangle - \langle \hat{s}(t) \rangle^2]_{h=0} = \int_{-\infty}^{\infty} \int_{-\infty}^{\infty} dt dt' K(t) K(t') \langle n(t) n(t') \rangle \quad (4.6)$$

where we used $\langle n(t) \rangle = 0$. This integral can be evaluated in the frequency domain through a Fourier transform. For a stationary noise, it simply gives:

$$N^2 = \int_0^{\infty} df S_n(f) |\tilde{K}(f)|^2 \quad (4.7)$$

where $S_n(f)$ is the one-sided power spectrum of the considered instrument. By definition $\langle n(f) n(f') \rangle = (1/2) S_n(f) \delta(f - f')$. Finally the expression for the SNR is:

$$\frac{S}{N} = \frac{\int_{-\infty}^{\infty} df \tilde{h}(f) \tilde{K}^*(f)}{\left[\int_0^{\infty} df S_n(f) |\tilde{K}(f)|^2 \right]^{1/2}} \quad (4.8)$$

The filter function maximizes the SNR for a given $h(t)$. For convenience we define a *weighted scalar product* of two generic functions $a(t)$ and $b(t)$ denoted $(a|b)$ and defined as

$$(a|b) = 4 \operatorname{Re} \int_0^{\infty} df \frac{\tilde{a}^*(f) \tilde{b}(f)}{S_n(f)} \quad (4.9)$$

where $\operatorname{Re}(z)$ is the real part of a complex number z . With such notations Eq (4.8) can be formulated as

$$\frac{S}{N} = \frac{(u|h)}{\sqrt{(u|u)}} \quad (4.10)$$

where the time-domain function $u(t)$ is the function whose Fourier transform is $\tilde{u}(f) = S_n(f)\tilde{K}(f)/2$. Determining the expression for $K(t)$ is equivalent to ask: what is the filter $u(t)$ that maximizes Eq (4.10)? The scalar product between two vectors being maximal for two collinear vectors, one must take $u(t)$ being proportional to $h(t)$ in order to maximise the SNR. In other words and in the frequency domain $\tilde{K}(f) \propto \tilde{h}(f)/S_n(f)$ where the proportionality constant is of no importance since rescaling by a factor does not change the SNR. The best filter is the one equal to the normalised expected signal (up to a normalisation by the PSD). Matched filtering-based searches are qualified as *modeled searches* as they rely on amplitude and phase models coming from well known astrophysical sources (see chapter 3). Another remark is that one must down-weight frequencies where the detector is more noisy to reach an optimal SNR whose expression is:

$$\left(\frac{S}{N}\right)^2 = (h|h) = 4 \int_0^\infty df \frac{|\tilde{h}(f)|^2}{S_n(f)} \quad (4.11)$$

Concretely a matched filtering search calculates $\hat{s}(\tau)$ defined by Eq (4.4) at each instant τ and in each detector (see Fig 4.2). Maxima of $\hat{s}(\tau)$ are identified and χ^2 -based tests [117] are performed in various frequency bands to test whether data is consistent with the best matching template. The recording of the SNR timeserie is performed in each detector. When a relevant candidate is found in an instrument, a next step in the analysis consists in ensuring that the signal appears coherently in the network. To this purpose only events present in pairs of detectors within a 15 ms window and detected thanks to the same template are considered as relevant GW candidates. Note however that the search is intrinsically not coherent as this last condition is imposed afterwards.

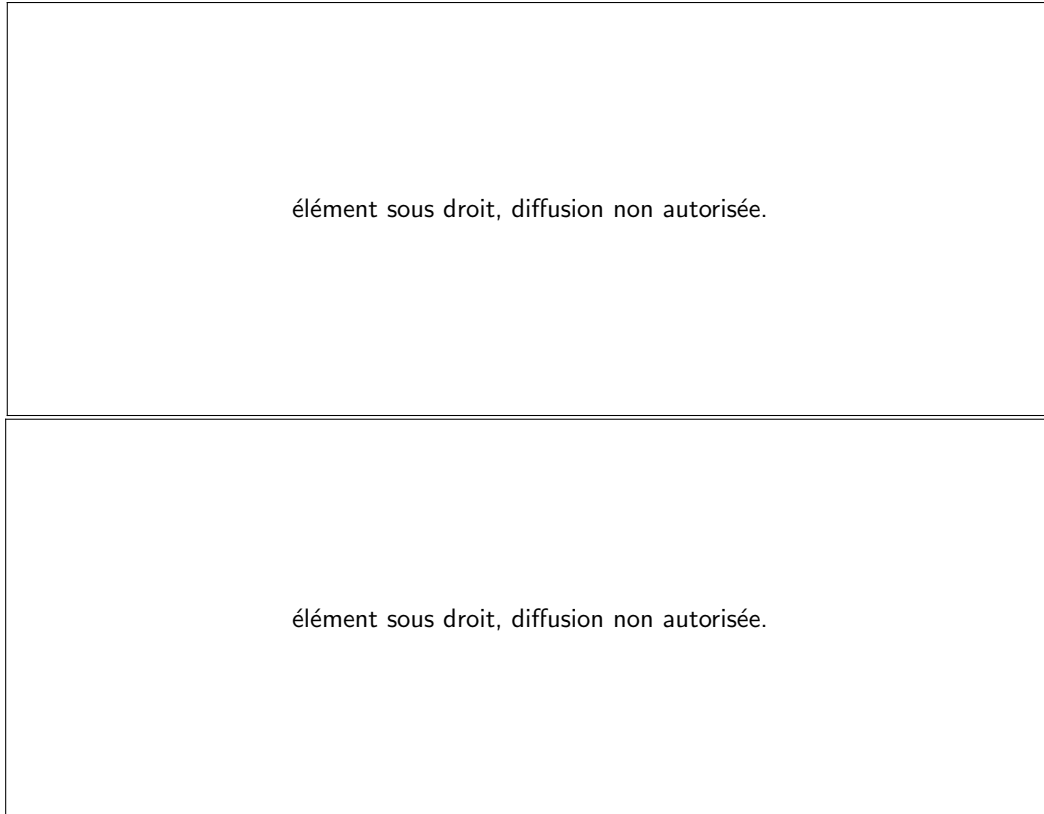


Figure 4.2: Matched filtering search results with the GW150914 event at the Handford (H1) LIGO detector. (*Top*) Signal-to-noise ratio $\rho(t)$ timeserie. Numerous side lobes come from the oscillatory behaviour of the compact binary coalescence signal. Maximum SNR is reached when both amplitude and phase match the template. (*Bottom*) Superposition of the preprocessed (band-passed then whitened) H1 data around the event and the best-matching templates. The two coincides at the merger instant where the SNR is the most important (Credits: LIGO Open Science Center).

Template banks

Searching the data is facilitated when a physical model of the targeted signal is available. As seen in chapter 1, the theory of general relativity provides a robust framework to predict GW emission waveforms. Sets of signal model later referred to as *templates* have been developed. Templates are in fact approximation of the real GW amplitude and phase of the GW emission relying either on a Post-Newtonian [62] for the inspiral part either an Effective-One-Body [118] approximation for the inspiral, merger and ringdown parts. An additional type of approximation consists in fitting computationally expensive numerical relativity waveforms. Each is restricted to an astrophysical context (still focusing on coalescing systems) and an associated parameter space enclosing the relevant physical quantities to describe the system. Among them one distinguishes between the *intrinsic parameters* which are the binary components masses m_1 and m_2 and spins χ_1 and χ_2 , and the *extrinsic parameters* which are the orbital inclination ι , the luminosity distance D_L , the sky localisation (θ, ϕ) , the polarisation angle ψ , the arrival time at geocenter t_{\oplus} and the coalescence phase ϕ_c . For instance, all these 9 parameters fully define the **TaylorT4** approximant waveform [84] which faithfully models the inspiral part of a BNS merger for which spins influence is negligible. An *approximant* in fact represents a computation method together with a given approximation precision. The computation method can be a direct integration of non-linear differential equations ruling the orbital evolution or an approximated formulation using a stationary phase approximation. The level of precision of the expansion is often given in terms of the post-Newtonian order. Some other astrophysical scenarios can be added to the previous list of intrinsic parameters depending on the context. Common ones are the components spins \tilde{S}_1 and \tilde{S}_2 ³ (which define 6 more parameters to the model) and less common are the binary spin precession angle α and the orbital eccentricity e .

Templates are usually grouped in banks spanning over a more or less extended part of the parameter space. These multidimensional regions are populated using stochastic placement *Markov Chain Monte Carlo* (MCMC) algorithms [119]. In fact distances in the parameter space are computed thank to a metric which gives a sense of how much should the distance between two nearby points vary if one varies each parameter one by one. In practice one specifies a maximum match between two neighbour templates and add to the template bank whatever point provided its distance is not too close to another template. In our study, the maximum density is decided to ensure that 90% of the detectable binaries are indeed detected provided real signal do not deviate from the waveform model. Template banks are more densely populated towards low masses as the phase modulation is more sensitive to low-chirp mass values [120]. To give an idea, the template bank grid associated to spinning BBH binaries counted 250,000 waveform templates spanning the compact binaries with total mass $M < 100M_{\odot}$, mass ratio $q = m_1/m_2 < 99$ and the dimensionless spin magnitude $\chi_{1,2} := S_{1,2}/m_{1,2} < 0.989$ during the first Advanced LIGO science run. The template grid used for the second Advanced LIGO run has 400,000 waveforms covering a parameter space extending to larger masses $M < 500M_{\odot}$ with a denser sampling to the high-mass region with $q < 3$.

Parameter estimation

Once detected a gravitational wave event remains to be characterized. This passes by inferring the source parameters when disposing of a signal model. We focus here on CBC sources since they are the best modelled GW sources (see chapter 1 and 3). Two parameter inference approaches are commonly applied: a frequentist approach which considers each parameter like a variable whose value is yet to be determined and the Bayesian approach for which a parameter is a random variable following a distribution. Such a distribution encodes all the informations on the model prediction and the results coming from the measurements. The Bayesian approach is commonly used in the LIGO and VIRGO collaborations. It is a natural way of obtaining an error estimate when combining data and model, including a prior knowledge or restricting the parameter space to physically relevant values. The central results in Bayesian statistics is provided by *Bayes theorem* [121]

$$p(\theta|\mathcal{D}) = \frac{\pi(\theta) \mathcal{L}(\mathcal{D}|\theta)}{p(\mathcal{D})} \quad (4.12)$$

The numerator of the right-hand-side in Eq(4.12) is the product of the *prior distribution* $\pi(\theta)$ and the *likelihood function* $\mathcal{L}(\mathcal{D}|\theta)$. The former contain the information one has on the parameters θ right before measurements are performed while the second encodes the knowledge acquired after the experiment has been performed. The denominator $p(\mathcal{D})$ is of little interest for parameter estimation purposes and is named the *evidence*. However it carries precious information when addressing Bayesian model selection problems. The left-hand-side $p(\theta|\mathcal{D})$ is another distribution called the *posterior distribution*. It can be viewed as an updated prior once information

³The spin angular momentum of the i^{th} compact object denoted S_i is related to the dimensionless spin vector χ_i by $\chi_i = S_i/m_i^2$

from the data are included. The fact of manipulating distribution instead of fixed quantities allows us to get a complete description and a full estimation of uncertainties. Models used in gravitational wave astronomy are quite complex and requires numerical approximations of the targeted posterior distribution [13]. Most popular strategies involve MCMC [122] techniques that are slow but accurate. In practice MCMC variants such as [123] are used so that multi-modal posteriors (*i.e.* posterior distributions composed of several peaks or ‘modes’) can be reliably sampled. This case is mostly encountered when dealing with angular physical quantities (polarisation angle, orbital inclination).

Sky location

In parallel to the parameter estimation step, the tridimensional source localisation (position on the celestial sphere and distance) is estimated thanks to triangulation-based techniques. For gravitational wave observations the location precision is far from the telescopes one: it cannot go below a few tens of square degrees (e.g., 60 deg² for GW170814 [23] which involved the LIGO and VIRGO detectors). As seen in chapter 2, the inclusion of other instruments helps reducing the error box in the sky localisation. For instance the GW150914 event has been estimated to lie within a 600 deg² area at 90% credible region with the two LIGO detectors. Simulations have revealed this error could have been divided by 10 if the VIRGO detector had been online at the moment of the event. In fact the poor spatial resolution is due to the antenna pattern functions which make the detector sensitivity dependent on both the position and orientation of the detector at the surface of the Earth and the source sky position. The luminosity distance is deduced from its inverse dependency to the signal amplitude. However, Eq (2.20) and Eq (2.21) explicitly show there is a degeneracy between the luminosity distance D_L , the orbital plane inclination ι and the orbital eccentricity e of a coalescing binary. This complicates the simultaneous determination of the posterior distributions. Luckily the two polarisations are differently affected by ι allowing an additional instrument to disentangle the degeneracy (provided at least 3 of the instruments within the network are not co-aligned). Gravitational waves are thus an inestimable way of measuring distances in the Universe and this independently of any other messenger. Said differently gravitational waves are a new kind of *standard siren* like type Ia supernova or variable stars [124]. Moreover they provide an independent determination of the Hubble constant with a given cosmological model [125].

It is worth noticing that luminosity distance helps defining the horizon of a GW detector. By convention, *horizon* is defined to be the distance at which an optimally oriented (face-on) equal-mass binary neutron star is detected with SNR = 8. Other close formulations [126] make the distinction between the horizon and the sensitive distance. Formally the horizon is:

$$D = \frac{1}{8} \left(\frac{5\pi}{24c^3} \right)^{1/2} (G\mathcal{M})^{5/6} \pi^{-7/6} \sqrt{4 \int_{f_{low}}^{f_{high}} \frac{f^{-7/3}}{S_n(f)} df} \quad (4.13)$$

where D is clearly detector dependent and this considering a fixed detection bandwidth $[f_{low}, f_{high}]$. Having a coincident EM counterpart is obviously important when trying to put constraints on the source distance. To this purpose catalogues of galaxies are build and compared against the derived sky position posteriors to infer the source host galaxy [127].

4.2.2 Unmodeled signals: generic transient searches

Burst sources of GW reflects a whole category of transient astrophysical phenomena: core-collapse supernovae, cosmic strings, merging compact binaries and possibly other unpredicted types of sources. These sources all share a poorly known phase evolution with time because of a lack of reliable models. Supernovae core collapses are a typical burst source which remain poorly understood due to the fact they involve a variety of physics domain: hydrodynamics, nuclear physics, particle physics, ... at various time and space scales. The complexity of the supernova mechanism is then approached by numerical simulations of the innermost processes in order to understand the internal motions responsible of the GW emission [128, 129]. Another feature of burst sources actually resides in the ‘burst’ denomination: all are brief and sudden GW emission that could be associated to the most violent phenomena in the Universe such as gamma-ray burst or magnetar flares.

Generalities

Generic transient searches do not operate with a specific waveform model knowledge. Minimal assumptions are formulated upon the GW signal waveform, in addition to assuming very basic properties such as the existence

of two polarisations and the fact gravitational waves propagate at the speed of light (see chapter 1). Generic searches are suboptimal with respect to matched filtering techniques when the signal waveform is accurately known. However they are more robust in the general case where a detailed knowledge of the signal is not available. They are thus the best hope to detect unknown GW sources.

Generic transient searches aim at detecting signals consistent with a common GW signal present in all detectors. To do so data streams from all detectors are mapped to the time-frequency plane and unmodeled searches monitor excess power that appear coherently in phase and time in such representations.

Fourier analysis provides the frequency content of a signal but does not tell when a given frequency appears. On the contrary, windowed Fourier transforms allows to capture frequencies evolving with time such as in GW chirp signals (e.g., Gabor transform [130] on a discrete time-frequency lattice). The discrete windowed Fourier transform S of a real-value function f with a time window g is:

$$Sf(n, m) = \langle f, g_{n,m} \rangle = \int_{-\infty}^{\infty} dt f(t) g(t - nu) e^{-im\xi t} \quad (4.14)$$

where $g_{n,m}$ is an *atom* of the windowed Fourier dictionary [131] and where n and m are indices over the time-frequency domain.. A *dictionary* refers to an ensemble of atoms over which the function $f(t)$ is decomposed. A Gabor dictionary \mathcal{D} is constructed by translating the atom $g_{n,m}$ by n in time and m in frequency, so that *ie.* $\mathcal{D} = \{g_{n,m}[n] = g(t - nu) \exp(-im\xi t)\}_{(n,m)}$ leading to regular time-frequency tiles that have a constant time-frequency resolution.

In this context, it is difficult to apply the Gabor transform to non-stationary signals like chirps. The typical timescale of a GW signal continuously changes from the inspiral to the merging phase. It is not exactly proportional to the signal frequency like wavelets. In order to catch the entire signal phase using a 'compact' representation, it is worth projecting the signal thanks to many transforms with ranging time-frequency resolutions. The idea is to create a dictionary formed by the union of Gabor dictionaries for instance. A more spread dictionary increases the probability to find an element of the dictionary with a good accordance with the local level and frequency of the signal. Such an extended dictionary is inherently redundant *ie.* it is a dictionary whose elements are correlated between each other. As a consequence the decomposition is not unique.

Wavelets cure this drawback by changing the time and frequency resolutions. The idea behind wavelets is to introduce a new dictionary $\mathcal{D} = \{\Psi_{n,m}(t) = (1/\sqrt{2^n})\Psi((t - 2^n m)/2^n)\}$ whose central element is a so-called *mother wavelet* Ψ . It is a zero-mean function with a scale parameter s and a time translation parameter u [131]. The wavelet transform of $f(t)$ is:

$$Wf(n, m) = \langle f, \Psi_{n,m} \rangle = \frac{1}{\sqrt{2^n}} \int_{-\infty}^{\infty} dt f(t) \Psi\left(\frac{t - 2^n m}{2^n}\right) \quad (4.15)$$

Now the atoms time-frequency resolution changes. A wavelet with small s describes well a sinusoid, *ie.* a signal with a wide time support and very located frequency content. On the opposite, when s gets higher the time support becomes narrower and the frequency spread increases. Such wavelets are more likely to catch transient parts of a signal (high frequency patterns).

In the following sections we describe a generic transient search pipeline which is at the heart of this thesis.

Coherent WaveBurst

cWB [132, 133, 134] is one of the main gravitational wave burst search pipelines used by LIGO and VIRGO. cWB has been successfully applied to all-sky searches for short-duration GW events. cWB detects and characterises a broad class of un-modeled GW transients thanks to the coherent analysis of the signals recorded by an array of detectors. A constrained likelihood statistic is then built from the salient pixels extracted from wavelet-based time-frequency representations of the data.

We first start by looking at the time-frequency representation used by cWB. We then detail how the constrained likelihood is constructed and how detection statistics are derived. Finally we go through each step of the cWB detection pipeline from the pre-processing of interferometric data until the event trigger generation.

cWB's time-frequency mapping is obtained through the so-called *Wilson-Daubechies-Meyer* (WDM) transform [135] which shares common properties with the windowed Fourier transform. It has the advantage of

curing the orthogonality problem raised by the Balian-Low theorem. This theorem states that if a dictionary $\{g_{n,m}|m, n \in \mathbb{Z}\}$ forms a basis of $L^2(\mathbb{R})$ then:

$$\int_{-\infty}^{\infty} t^2 |g(t)|^2 dt = \infty \quad \text{or} \quad \int_{-\infty}^{\infty} \xi^2 |\tilde{g}(\xi)|^2 d\xi = \infty \quad (4.16)$$

Or said differently it does not exist a Gabor dictionary that forms a basis of $L^2(\mathbb{R})$ and whose atoms are both well localised in time and frequency. WDM transform are Wilson-Daubechies transforms [136] with a Meyer scaling function denoted ϕ . Formally the atoms of the WDM dictionary are defined as:

$$g_{n,0}(t) = \phi(t - nT) \quad (4.17)$$

$$g_{n,m}(t) = \begin{cases} \sqrt{2}(-1)^{nm} \cos(2\pi mt/T) \phi(t - nT/2), & \text{if } m + n = 2k, m > 0 \\ \sqrt{2} \sin(2\pi mt/T) \phi(t - nT/2), & \text{if } m + n = 2k + 1, m > 0 \end{cases} \quad (4.18)$$

where T is the time resolution of ϕ . Note the complex exponential term in the definition of a Gabor atom is replaced by a sine and a cosine terms. The WDM dictionary forms an orthonormal basis of $L^2(\mathbb{R})$ if ϕ satisfies admissibility conditions [135]. The Meyer scaling function obeys those conditions. In practice the Meyer scaling function prevents spectral leakage (sharply decreases in frequency) and the resulting forward/backward transform can be efficiently thanks to fast Fourier transform algorithms. It thus provides a family of atoms which are very compact in the time-frequency domain. Such a behaviour is appreciated when working with band-limited sampled data sets. cWB uses a union of WDM bases. A given time-frequency (TF) map, as defined previously, is seen as a grid on the TF domain whose tiles have fixed dimensions due to the window function. cWB selects pixels whose amplitude exceed a level-dependent threshold and clusters the pixels selected for all resolutions. So using an union of cWB bases with various TF tiles allows to catch the phase variability inherent to chirp-like signals.

Let $s[n] = s(t_n)$ with $n = 0, \dots, N - 1$ be the time-series samples. Then WDM decomposition coefficients at a fixed TF resolution are given by

$$x[i] = \sum_n g_i[n] s[n] \quad (4.19)$$

where i denote a time-frequency index and N is the number of samples in the data segment. A $x[i]$ element is further referred to as a *wavelet*⁴ or a *pixel*. WDM wavelets are characterised by three parameters namely centred time, centred frequency and level s . Level actually refers to the TF resolution level of a cWB grid as each level $M = 2^s = T f_s / 2$ corresponds to a WDM time-frequency map with size $(M + 1) \times (N/M)$ and where f_s is the data sampling frequency. The time resolution is M/f_s and the frequency resolution is $f_s/2M$. Note that as M increases the frequency resolution increases while the time resolution decreases as shown on Fig 4.3.

In addition to the presented likelihood functional, cWB also includes regulators [134]. Their main goal is to get rid of non-physical transient events being flagged as possible GW candidates. Depending on the GW source orientation with respect to a detector, one has $|f_\times| \ll |f_+|$ where f_+ and f_\times are the orthogonalised versions of the antenna beam pattern functions defined in 3.6. In this so called *dominant polarisation frame* [134], and in this case, most of the SNR produced by this event is contained in the f_+ detector response. On the contrary, the f_\times response has little contribution and is likely to be noise dominated. This has an impact on the GW signal reconstruction.

⁴Even if not totally appropriate

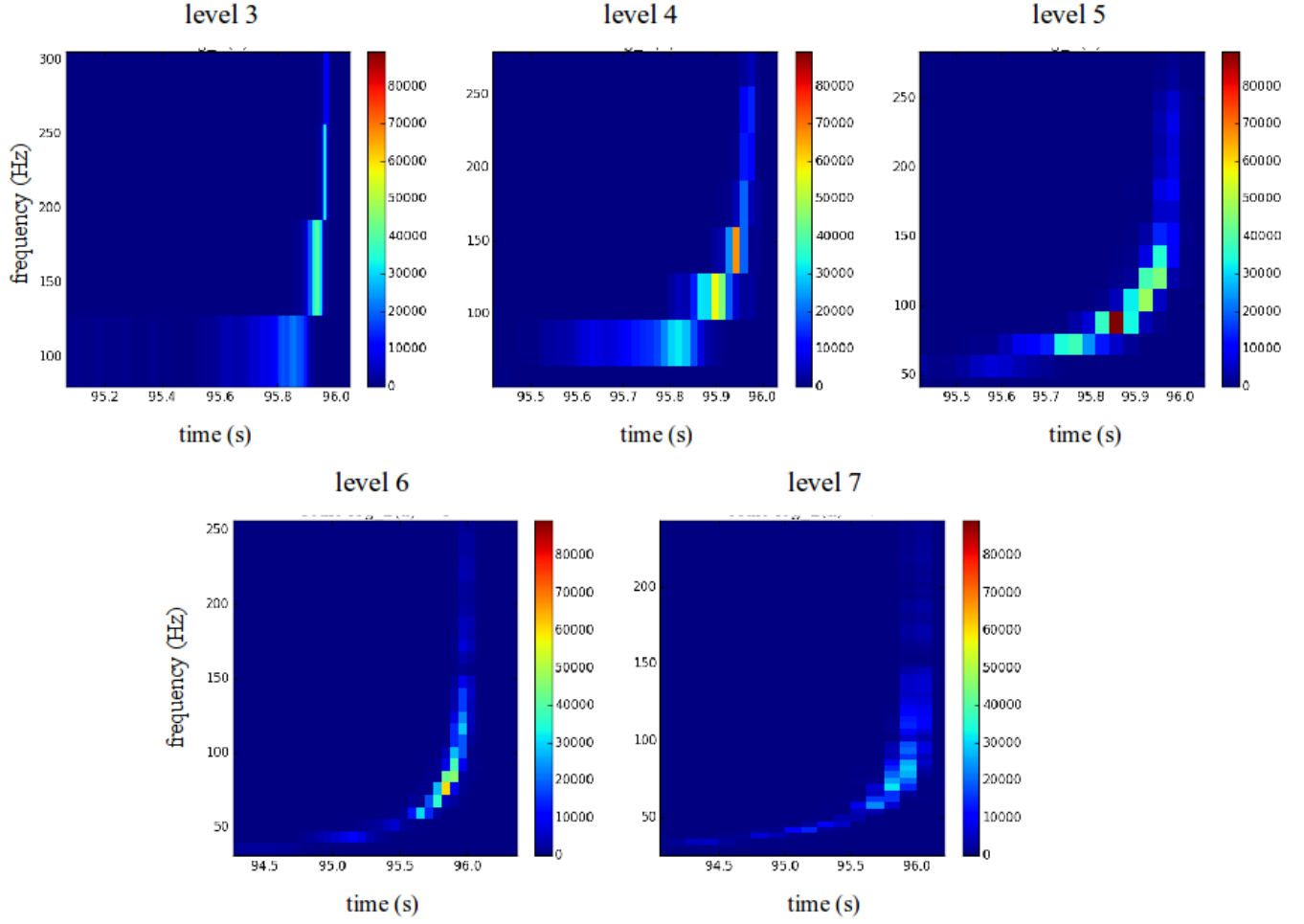


Figure 4.3: Time-frequency maps resulting from the WDM decomposition of a coalescing $10 - 10M_{\odot}$ non-spinning circular binary black hole on levels 3 to 7. Time (resp. frequency) resolution gets refined when the decomposition level decreases (resp. increases).

Algorithm

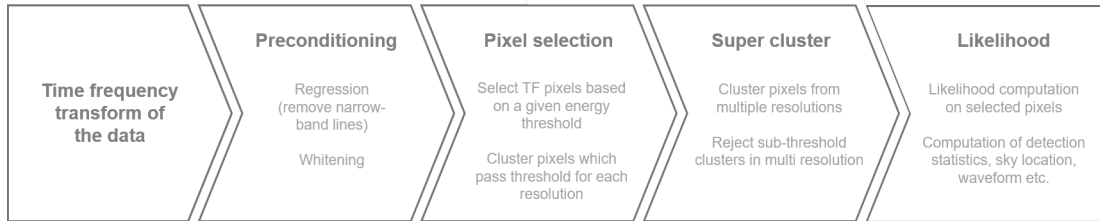


Figure 4.4: cWB pipeline detection flowchart.

The overall cWB algorithm is sketched in Fig 4.4. Data from each detector is first band-passed to focus the analysis on the frequency band of interest for GW observations. Then data is decomposed on a multi-leveled WDM basis and whitened using the specific detector PSD estimate. Strong narrow-band lines such as mechanical resonances are removed by a linear predictor filter. The whitened data are obtained by $x_k(t, f)/\sigma_k(t, f)$ where the standard deviation $\sigma_k(t, f)$ is estimated over the entire segment, thus providing noise-scaled TF maps $w_k(t, f)$ at each decomposition level and for each detector k .

The next step consists in selecting salient pixels depending on the TF background level and their energy. cWB computes energy TF maps from every detector taking into account the time delays. More precisely it is the

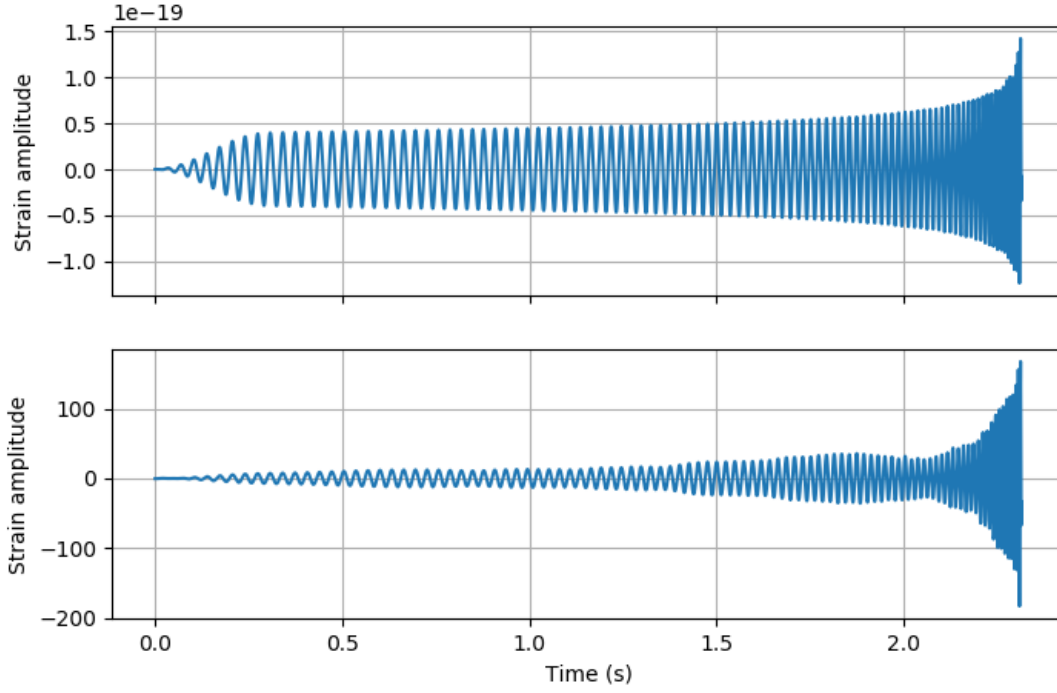


Figure 4.5: Non-spinning circular $10 - 10M_{\odot}$ BBH waveform using the `TaylorT4` approximant with starting frequency $f_{low} = 32$ Hz. (*Top*) non-whitened waveform (*Bottom*) whitened waveform.

energy contained in each TF resolution $E[i] = \sum_k w_k^2[i]$ which is first maximised over all possible time of flight delays. Note these time delays are the same needed to maximise the likelihood ratio. Only pixels whose amplitude is above the last centile (or per-mille) under Gaussian noise assumption are collected. cWB uses a clustering scheme based on a nearest-neighbour approach to build clusters of TF pixels. It forces the resulting cluster to be compact in the TF domain. If all the clusters passed this first step then they are all assembled in a supercluster thus ranging over all the TF resolutions. This supercluster also has to pass some thresholds so as to be flagged as a relevant GW event. For what follows, it is important to remark there exist no constraint at all on the shape a cluster can have. cWB only applies limits on the cluster by fixing the maximum gap existing in time and frequency. Otherwise extracted pixels can have whatever distribution in the TF domain: no particular phase evolution is tracked as expected from an unmodeled searches.

cWB adopts a frequentist approach to the gravitational wave detection problem. Two hypotheses are confronted thanks to a model comparison method between: (i) the analysed data segment contains no GW signal (H_0 hypothesis) and (ii) the analysed data segment contains noise plus a GW signal (H_1 hypothesis).

cWB firstly estimate the noise PSD $S_k[i]$ and it is used to whiten raw TF-mapped data $\mathbf{x}[i] = \{x_1[i], \dots, x_K[i]\}$ from the K detectors. One finally gets to the noise scaled data $\mathbf{w}[i] = \{x_1[i, \tau(\theta, \phi)]/\sqrt{S_1[i]}, \dots, x_K[i, \tau(\theta, \phi)]/\sqrt{S_K[i]}\}$ where τ is a time-shift accounting for the time delay to a reference detector among the K instruments. As a consequence data still possesses a dependence on the source position. It is made explicit denoting:

$$\mathbf{x}[i] = \xi[i; \theta, \phi] + \mathbf{n}[i] \quad (4.20)$$

where $\mathbf{h}[i] = [h_+[i], h_{\times}[i]]$ is the gravitational wave vector composed of the two polarisations, $\xi[i] = \mathbf{F}[i; \theta, \phi] \cdot \mathbf{h}[i] = f_+[i; \theta, \phi]h_+[i] + f_{\times}[i; \theta, \phi]h_{\times}[i]$ is the noise-scaled network response and $\mathbf{F}[i; \theta, \phi] = [f_+[i; \theta, \phi], f_{\times}[i; \theta, \phi]]$ is the network antenna pattern (see Eq (3.6)). When the H_0 hypothesis is verified, it is assumed that the collected data arise from Gaussian noise fluctuations with probability distribution $p(\mathbf{x}|H_0)$. On the contrary when the H_1 hypothesis is verified, data result from a common GW signal in all the detectors with probability distribution $p(\mathbf{x}|H_1)$. With these notations the likelihood ratio is $\Lambda = p(\mathbf{x}|H_1)/p(\mathbf{x}|H_0)$ can be written in the following form:

$$\mathcal{L} = 2 \log \Lambda = 2 \langle \mathbf{w} | \xi \rangle - \langle \xi | \xi \rangle \quad (4.21)$$

where $\langle . | . \rangle$ denotes the Euclidean scalar product. Non-optimal solutions have been proposed [134] like the *mlr* over the sky position and the GW polarisations. In this approach the maximum likelihood ratio (MLR) is computed over the whole network and it is compared to a fixed threshold. The MLR approach then yields:

$$\mathcal{L}_{max}(\theta, \phi) = \sum_{i \in C} \mathbf{w}[i] \mathbf{P}[i] \mathbf{w}^T[i] = \sum_{i \in C} \sum_{n, m} w_n[i] P_{nm}[i] w_m[i] \quad (4.22)$$

where C is the extracted cluster of pixels and \mathbf{P} is a projection operator onto the so-called dominant polarisation frame (DPF) characterised by $(f_+ | f_\times) = 0$ and $|f_+| \geq |f_\times|$. DPF is generated by the vectors e_+ and e_\times collinear to f_+ and f_\times respectively. Eq (4.22) is in fact a quadratic form whose symmetric matrix can be split into a diagonal and off-diagonal parts. The diagonal part contributes to the *incoherent energy* E_{inc} while the off-diagonal part contributes to the *coherent energy* E_c .

$$E_{inc} = \sum_{i \in C} \sum_n w_n[i] P_{nn}[i] w_n[i] \quad (4.23)$$

$$E_c = \sum_{i \in C} \sum_{n \neq m} w_n[i] P_{nm}[i] w_m[i] \quad (4.24)$$

In the previous relations the matrix notations have been dropped so as to explicit the different contributions from the diagonal and off-diagonal components of \mathbf{P} . The two energy contributions have to be compared to the *null energy* E_n measured in the null space of \mathbf{P} . This subspace is orthogonal to the DPF and collects the residual detector noise. By definition the null energy is the energy remaining after subtracting the MLR value:

$$E_n = E_0 - \mathcal{L}_{max} = \sum_{i \in C} \mathbf{w}[i] \mathbf{P}^{null}[i] \mathbf{w}^T[i] \quad (4.25)$$

with $\mathbf{P}^{null} = \mathbf{I} - \mathbf{P}$ and \mathbf{I} is the identity matrix and where E_0 is thus:

$$E_0 = \sum_{i \in C} \sum_n \mathbf{w}[i] \mathbf{w}^T[i] \quad (4.26)$$

All of the three energies defined so far are combined into cWB statistics. The *network correlation coefficient* c_c quantifies the signal correlation over all the detectors. It is defined as $c_c = E_c / (|E_c| + E_n)$. A noise free GW signal observed by all detectors yields $c_c = 1$ whereas noise fluctuations are not expected to be coherent and have $c_c \ll 1$. Note in the previous formula the correlation information is provided by E_c , that is the off-diagonal components of the MLR statistic. The second important statistic η_c quantifies the strength of a coherent signal and is defined as $\eta_c = \sqrt{c_c E_c K / (K - 1)}$. It is proxy to the matched-filtering network SNR. Depending on the search other statistics are used together with the above ones. For compact binaries searches for example, the chirp mass is estimated and a cut is imposed that discard unphysical chirp mass estimate values. In the end a cWB trigger event is described by a set of TF pixels and a few detection statistics.

The MLR estimate is also used for the signal reconstruction. Recall that to build an isolated cluster, cWB selects pixels or wavelets which correctly approximate the signal. In addition to the position of a pixel in the TF domain it also carries an amplitude. The linear combination of the selected wavelets is an approximation of the GW signal extracted from noisy data. Mathematically, the maximisation of Eq (4.21) with respect to the GW polarisations gives:

$$\hat{h}_{+, \times}[i] = \frac{(\mathbf{w}[i] | \mathbf{f}_{+, \times}[i])}{(\mathbf{f}_{+, \times}[i] | \mathbf{f}_{+, \times}[i])} \quad (4.27)$$

It is the literal expression for the reconstructed polarisations from the data. This aspect actually underlines the only assumption formulated by cWB on the targeted signal: searched signals are bivariate and as explained in chapter 1, is a direct consequence of gravitational wave physics.

Maximisation of Eq (4.21) at each sky position provides a likelihood probability density map for the source position on the celestial sphere. In practice, the sky is divided into patches (or cells) of fixed area (usually 0.2 deg^2) which is assigned a central sky position. cWB runs over the patches and compute the time delays τ coming in the definition of \mathbf{w} and finally successfully estimate \mathbf{w} , \mathbf{x} and Λ . The evaluation of the MLR on a celestial sphere composed of $\sim 200,000$ cells involves an important computational cost in cWB.



Figure 4.6: Skymap of the GW150914 event as produced by cWB. The displayed 90 % confidence region spans 600 deg^2 [137]

4.2.3 Event significance

We have shown how GW signals are retrieved from measurements and more exactly what are the two main strategies to extract them from the noise. Both provide a decision statistics likely to isolate a GW signal: matched filtering techniques use a χ^2 re-weighted SNR and generic searches build statistical estimators of the energy contained in the TF domain.

A type of statistical error consists in rejecting the null hypothesis (*i.e.* the absence of GW signal) while it is actually true. In terms of signal detection theory it is questioned how likely an event arises from a gravitational wave: what is the probability (or equivalently the frequency) of making an error when stating a GW signal is present in the data when there is none ? This frequency is most known as the *false-alarm rate* (FAR). Its determination is non trivial as it is not possible to collect signal-free background or said differently to shield the detectors from a passing gravitational waves. The cWB algorithm uses the technique of time lags to estimate the FAR vs. ranking statistic η_c curve. We introduce in advance the η_c quantity computed by cWB as it is a proxy for the GW signal strength in an array of GW detectors. For a given data set, the method consists in generating an artificial amount of data from real data streams coming from each detector. It is achieved by shifting pairwise data segments by multiples of the GW time-of-flight from one detector to the other. This very last element is crucial as it ensures that any coincident signal that may be detected while analysing time-shifted data streams may simply be false alarm coincidences. The overall analysis then yields a count of spurious events arising from noise fluctuations or transients as a function their strength. One obtains a background curve similar to what is shown on Fig 4.7.

Among others the advantage of computing a background curve enables to map the FAR to a false alarm probability and hence to a detection significance. This is what is shown on the top part of Fig 4.7. Note that the background depends greatly on the binary masses. For instance, ‘blip’-glitches (common class of short-duration and wide frequency range glitches) are short duration signals (with less cycles) that mimic GW signals with short durations. In this case, GW signals show a TF morphology closer to the one of a glitch and bring loud SNR triggers.

Other possible manners of gaining confidence in a detection are to: look for transient noises present within a time window around the candidate event, monitor the 200,000 sensors (magnetometers, seismometers) around the detectors. But the less ambiguous evidence is brought by a direct association with an astrophysical event (gamma-ray burst, optical transient, magnetar flares) as the GW170817 event demonstrated it. Unfortunately, gravitational wave bursts are particularly well simulated by non-Gaussian events from transient disturbances in the detector electronics and optics. Most of transient noises are impossible to model and the only way of eliminating them is to perform coincidences between instruments. When the presence of a glitch is evident



Figure 4.7: Background curves associated to generic transient searches during the first *LIGO* observational run O1. We display a quantity proportionnal to the FAR, namely the count of transient noise events during the O1 run in a given bin of η_c . The loudest event GW150914 present in O1 data appears with an important η_c statistic and is thus largely detached from the background. Dedicated searches look for signals with various time-frequency morphologies: known populations of transient noises (C1), events whose frequency increases with time (C2) and events that do not match in previous classes (C3) [12]

minimal *data quality vetoes* are applied to the concerned data segments (see Sec 5.5.1).

4.2.4 Limitations of current searches

The search for BBH signals in the LIGO and VIRGO data is performed using a variety of methods, among which matched filtering techniques are the most commonly used. Matched filtering use a discrete grid of templates known as a waveform template bank. The waveform templates are obtained by solving for the coalescence dynamics during the inspiral and merger phases. Current targeted BBH searches use template waveforms obtained from the quadrupolar order, *ie.* gravitational wave modes emitted by a BBH in quasi-circular orbits and with spins aligned with the orbital angular momentum [120]. Those are reasonable assumptions on the physics of the source and have shown to be justified with the last detections [12, 21]. Template-based methods require the model to be in almost perfect phase match with the gravitational wave emission from binaries. Current searches ignore three effects that can be relevant in several formation scenarios such as dynamical captures in dense stellar environments: higher-order than quadrupolar gravitational wave modes, orbital precession due to non-aligned spins with respect to the orbital spin and orbital eccentricity.

The inclusion of those effects is not straightforward for several reasons. First, gravitational wave modelling from binaries is still a topic of active research and accurate waveform models are not always available. It is particularly true for eccentric waveforms which do not extend to high eccentricity values [138, 85]. Second, a larger search space implies a larger template grid, and thus larger computing needs. For instance, the search for arbitrarily spinning (*ie.* precessing) binaries requires 10 times more template waveforms. More precisely, millions of templates are needed with relaxed sampling density requirement when computing the template bank.

The use of a wavelet representation of the targeted signals by unmodeled searches is itself an advantage. Indeed matched filtering searches look for a correlation in phase in the data. The phase coherence should be very precise to ensure the efficiency of these methods. So in the case of poorly known sources for which at least a rough knowledge exist, modelled searches are not expected to perform well. Instead wavelets locally fit the data and do not need an overall precise agreement in phase.

Chapter 5

Wavegraph

Contents

5.1	Computation of time-frequency patterns	59
5.1.1	Stationary phase approximation	59
5.1.2	Sparse time-frequency representation and WDM transform	62
5.2	Graph computation	63
5.3	Search the observational data using the graph	65
5.4	Comparison study: Gaussian noise case	66
5.4.1	Time-frequency graphs	67
5.4.2	Simulated data sets	68
5.4.3	Results	68
5.5	Comparison study: real noise case	71
5.5.1	cWB gating and vetoes	72
5.5.2	A glitch rejection algorithm for Wavegraph	73
5.5.3	Running Wavegraph with consistency test in O1 data	75

In this chapter we present *Wavegraph* (WG), a novel clustering scheme dedicated to cWB [1]. The goal of Wavegraph is to address some of the limitations of current searches identified in Sec 4.2.4. Wavegraph is based on a pattern matching formulation of a signal detection technique performed in the TF domain. Expected patterns are computed from a template bank. Wavegraph can be viewed as a matched filtering technique performing in the TF domain. Astrophysical scenarios generally provide a range of waveforms parametrized by several physical source parameters. For example compact binary mergers phase is mainly driven by the binary components masses and spins. This leads to some variability in the expected time-frequency pattern. In Wavegraph the waveform model phase variability is encapsulated into a graph. Sec 5.1 reviews methods to compute the time-frequency pattern from a time domain waveform. We also describe a sparse signal approximation algorithm which allows to obtain a reliable description of the waveform model. Using the graph the detection problem can be reformulated as a combinatorial optimization problem for which efficient algorithms exist as explained in Sec 5.3. Along this chapter we focus on GW signals emitted from coalescing compact binaries.

5.1 Computation of time-frequency patterns

Wavegraph relies on the *a priori* knowledge of the targeted signal. Wavegraph establishes a mapping between the reference waveform and its representation by a finite set of pixels in the TF domain. This section reviews different methods in order to establish such a mapping.

5.1.1 Stationary phase approximation

The first pixel selection method determines which wavelets of the dictionary has the largest coupling with the targeted signal by working in the continuous limit. We use a transform where time, frequency and levels vary continuously. Sine-Gaussian (SG) basis are used to allow for analytical and hence fast computations [139]. The

SG wavelet with central time t_0 , central frequency f_0 and level ℓ_0 (or scale) is defined in the frequency domain as

$$\tilde{w}_0(f) = \tilde{g}(f - f_0; \sigma_0) e^{-2\pi i f t_0} \quad (5.1)$$

where $\tilde{g}(f; \sigma) = (2\pi)^{1/4} \sqrt{\sigma} e^{-\pi^2 \sigma^2 f^2}$ is the mathematical expression of a SG atom in the frequency domain. The parameter σ_0 defines the typical time-scale of the SG wavelet. It can be approximately related to the level parameter ℓ_0 in the discrete WDM transform by $\ell_0 \sim f_s \sigma_0$ (where f_s is the signal sampling frequency). A SG wavelet transform is a projection onto the SG basis such that the square of the TF map coefficients are given by

$$\rho_0^2 = \rho(t_0, f_0, \ell_0)^2 = \left| \int df \frac{\tilde{w}_0(f) \tilde{s}(f)}{S_n(f)} \right|^2 \quad (5.2)$$

In order to identify salient pixels one has to identify times t_0 and levels ℓ_0 which maximise the square energy ρ_0 at a given f_0 . However Eq (5.2) is analytically intractable in general but can be simplified for chirp-like signals. Chirp signals can be expressed in the complex domain as $\tilde{s}(f) = A(f) e^{i\Psi(f)}$ where we denoted the amplitude $A(f)$ and the phase $\Psi(f)$ of the chirp. Eq (5.2) can then be re-written in term of an oscillatory integral $\int dx f(x) e^{ig(x)}$. Assuming slow variations of the integrand amplitude with respect to the integrand phase, Eq (5.2) can be approximated using the *stationary phase approximation* (SPA). As a consequence the square energy expression becomes (the derivation is detailed in Appendix 7.2):

$$\rho_0^2 \sim \frac{\pi |\mathcal{A}(f_0)|^2}{|\pi^2 \sigma_0^2 - i\beta|} \exp \left(\text{Re} \left[\frac{\pi^2 (t_0 - \tau(f_0))^2}{\pi^2 \sigma_0^2 - i\beta} \right] \right) \quad (5.3)$$

where $\mathcal{A}(f) = (2\pi)^{1/4} \sqrt{\sigma_0} A(f)/S_n(f)$ and $\text{Re}(z)$ denotes the real part of the complex number z . Also $\beta = \ddot{\Psi}(f_0)/2$ is the chirp rate and $\tau(f_0) = -\dot{\Psi}(f_0)/2\pi$ is the group delay of a SG wavepacket. Maximisation of the previous equation over t_0 and σ_0 at a given frequency yields

$$\rho(\hat{t}_0, f_0, \hat{\ell}_0)^2 = \frac{f_s}{\sqrt{\pi}} \frac{|A(f_0)|^2}{\hat{\ell}_0 S_n^2(f_0)} \quad (5.4)$$

Such a maximum is reached at $\hat{t}_0 = \tau(f_0)$ and $\hat{\sigma}_0 = \sqrt{|\beta|}/\pi$ converted into $\hat{\ell}_0$ using the Gaussian to Meyer conversion rule stated above. Finally, the parametric curve associated to the signal $\tilde{s}(f)$ is

$$\mathcal{C}(f_0) = \left[\hat{t}_0 = -\frac{1}{2\pi} \dot{\Psi}(f_0); f_0; \hat{\ell}_0 = \frac{f_s}{\sqrt{2\pi}} \sqrt{|\ddot{\Psi}(f_0)|} \right] \quad (5.5)$$

Eq (5.5) provides an approximation for the wavelet transform in the continuous limit. This curve has to be discretized according to the time-frequency-level lattice adopted by cWB. It results in a finite and ordered set of pixels/wavelets \mathcal{C} referred to as a *chirp path*. Four chirp paths are shown on Fig 5.1 with increasing values of total mass. We recover the fact that high mass binaries have a short signal duration. High frequency content is mostly described by short-time wavelets, *i.e.* low-level SG wavelets. The use of different levels enables us to obtain bright pixels above the noise level (see Fig 5.2).

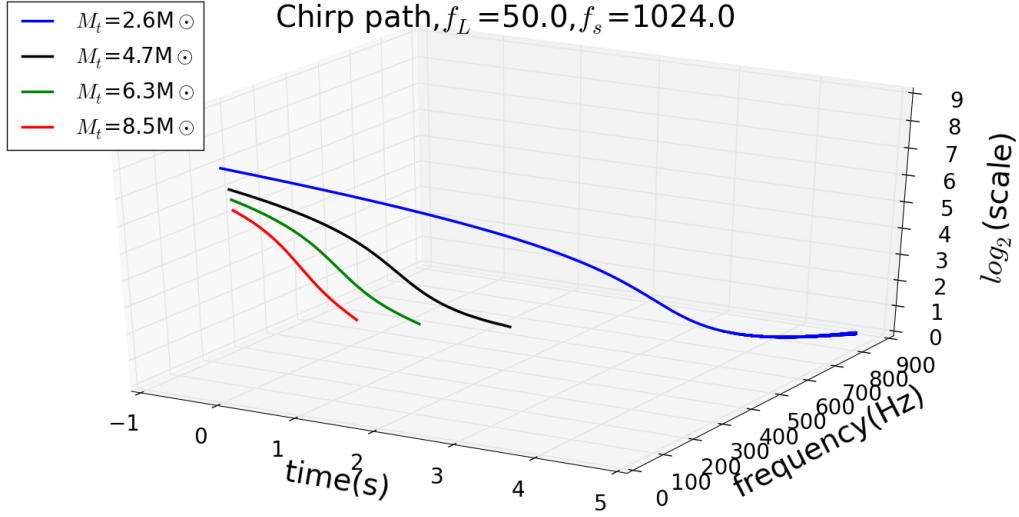


Figure 5.1: Chirp paths obtained by using the SPA. Here again coalescing binary signals show an increasing frequency with time.

For the purpose of the algorithm, the cluster \mathcal{C} is in fact discrete. It means that the cluster will in fact be described as a finite set of salient pixels (dark grey pixels in Fig 5.2). Those pixels are obtained by maximising Eq (5.4) for each frequency and level bins. An isolated cluster with this technique is displayed in Fig 5.2. Pixels follow the TF evolution trend of the GW signal and this over the decomposition levels.

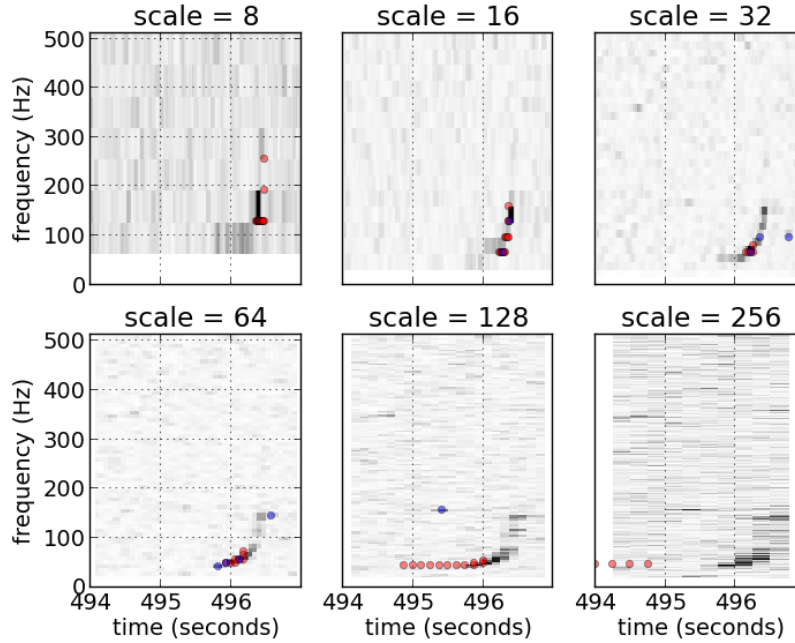


Figure 5.2: Selected TF pixels by using the SPA at each TF resolution ($\ell_0 = 3, \dots, 8$). The GW signal is a chirp with associated masses 8.6 and 3.3 M_\odot . Clusters extracted at each level/scale by Wavegraph are indicated by red dots and the clusters extracted by cWB are shown with blue dots.

The previous derivation yields an efficient yet not completely accurate TF representation of the signal. Indeed noise-free chirp signals are poorly reconstructed with such a method as the low phase oscillation hypothesis on which SPA relies on is less and less verified as one gets close to the merger part of the signal. But the most important caveat is the loss of reconstructed signal energy we experienced when looking for GW events in noisy data. We realised an average 40% loss in the reconstructed SNR. We tried to extract the first neighbours of each maxima along the time axis when those neighbours at least carry a fraction of the energy of the loudest

pixel. The idea has been pushed until the third neighbours but has not proved to catch the necessary amount of energy. In the end we realised a need for a new pixel selection algorithm that conserves the phase evolution information but also gathers more energy from the noise free GW signals.

The use of wavelets to describe GW signals consists in locally fitting the waveform model. This contrasts with the matched filtering approach in the sense where a global phase accordance is needed between the data and the waveform models. Decomposing the signal with wavelets makes the search more robust with respect to poorly modeled GW signals.

5.1.2 Sparse time-frequency representation and WDM transform

Contrary to expansions performed in a Fourier basis for instance, signal expansions in redundant dictionaries are not unique. Sparse expansions present a specific interest here as they provide a complete signal representation where the power is concentrated in a small set of dominant pixels that are more likely to stand above the noise level. Those algorithms are widely used in the domain of signal processing for de-noising or signal compression purposes. Also, thanks to the small number of pixels there is a reduced probability that one or several pixels in the decomposition match noise fluctuations in GW data.

Sparse signal approximations in redundant dictionaries has been a field of research in applied mathematics for the last twenty years. Although the approximation is known to be a NP-hard problem ¹, algorithms exist that provide sub-optimal solutions. Given an astrophysical model y we want to obtain a sparse approximation x which satisfies

$$\min_x \|x\|_0 \quad \text{subject to} \quad \|y - W^T x\|_2 \leq \delta \quad (5.6)$$

where $\|\cdot\|_p$ is the L_p norm, W is the WDM transform operator from the time domain to the time-frequency domain and δ is the approximation error detailed after. Wavegraph uses the *matching pursuit* (MP) algorithm proposed by [131] to solve the Eq 5.6 problem. Other algorithms have been proposed and tested as detailed in [3].

Procedure 1 Wavegraph matching pursuit algorithm

Input: signal to be decomposed y , approximation error δ

Output: Time-frequency approximation (WDM maps) x

Initialise set of chosen pixels $x \leftarrow \emptyset$

Initialise the residue $r \leftarrow y$

while $\|r\|_2 > \delta$ **do**

 Compute WDM transform of the residual $g_n \leftarrow W r$

 Select best fitting WDM pixel $p \leftarrow \operatorname{argmax}_n \|g_n\|_2$

 Add it to the current approximation $x \leftarrow x + p$

 Update the residual $r \leftarrow y - W^T x$

return x

In Alg (1) we detail the MP algorithm. An initial time-domain signal y is decomposed on the cWB TF grid thanks to the W operator. At each iteration one collects the best coupling WDM pixel with the signal then subtract its inverse WDM transform from the current signal called residual (as its norm keeps on decreasing with iterations). The best pixel selection and subtraction steps are repeated until a termination condition is fulfilled. Wavegraph terminates when 80 % of the original signal energy (L_2 norm) is reconstructed. Fixing the termination condition at 80 % is a good compromise as, above this level the convergence is very slow and the approximation error reaches a plateau (see top panel of Fig 5.3). In such conditions, the algorithm selects low amplitude pixels that do not contribute significantly to the overall detection efficiency of the pipeline.

Fig (5.3) illustrates the MP algorithm with a BH signal. On the top panel is displayed the convergence of the MP algorithm tested with the same signal as on the upper panel of Fig (4.5). During the first iterations, the MP algorithm picks high amplitude pixels/wavelets which are nearly orthogonal to each other. The MP behaviour

¹Non-deterministic polynomial-time (NP) problems are problems for which no algorithm exist that can solve these problems in polynomial time. A typical example of NP-hard problem is the *traveling salesman problem*.

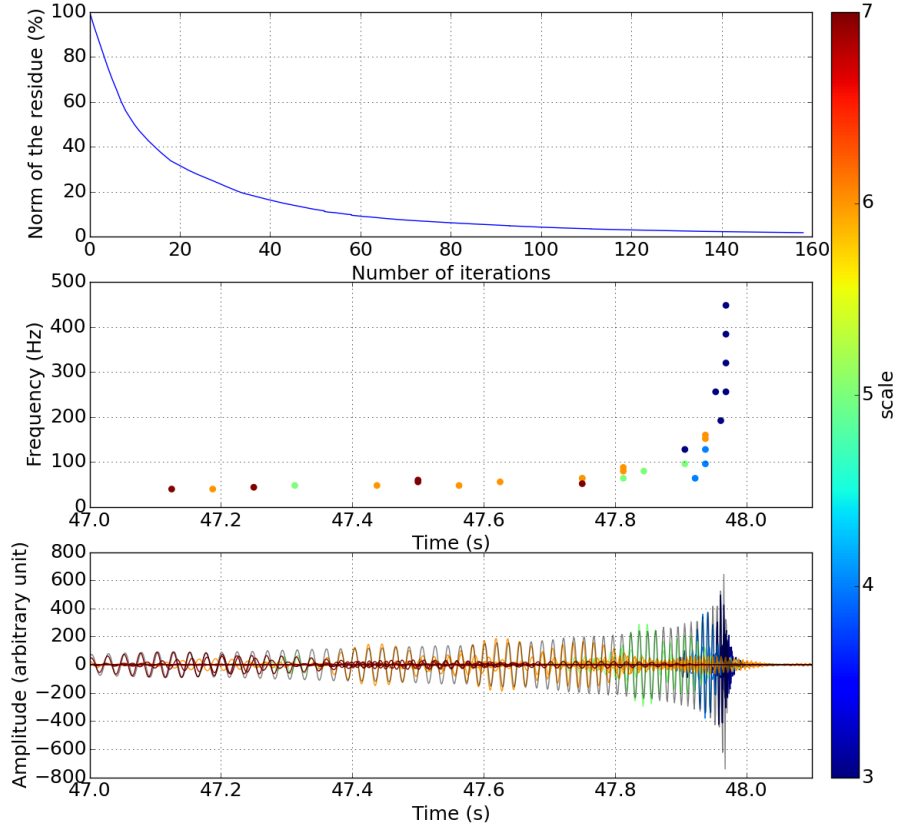


Figure 5.3: Convergence of the matching-pursuit algorithm in the case of an equal-mass non-spinning BBH waveform with $20 M_{\odot}$ total mass after whitening by advanced LIGO design sensitivity PSD. Fixing the termination condition at $\delta = 20\%$, collects 33 pixels (*top*). Time-frequency pixels selected by the matching pursuit algorithm (*middle*) and corresponding wavelets and approximation (*bottom*) for the very same signal. The color indicates the scale ℓ associated to each pixel that corresponds to a wavelet timescales $2^{\ell}/f_s$ with $f_s = 1024$ Hz. The strain amplitude of the original waveform (*black*) is shown in the background. Few early pixels selected by the MP are not displayed because they fall outside the frame chosen for this figure.

mimics the one of a principal component analysis [140]. After about 20 iterations, convergence slows down until reaching a plateau. In the middle panel the TF map contains the set of WDM pixels returned by Alg (1) with $\delta = 20\%$. Clearly short (resp. long) duration in blue (resp. red) pixels describe the late (resp. early) part of a coalescing binary signal. Finally the bottom panel shows the corresponding wavelets obtained by inverse WDM reconstruction in the time domain. Although the approximation error is relatively large the waveform reconstruction is globally satisfactory (see Appendix 7.2).

Sparse approximation techniques described here works for any signal morphology *i.e.* whether they are chirp-like or not. In principle, these techniques allow to use Wavegraph on a broader class of signals. Clusters obtained with other template waveforms are illustrated in the last chapter of this thesis.

5.2 Graph computation

The set of time-frequency pixels selected by the sparse signal approximation provides a compact representation of the waveform model. With the selected pixels, we form a cluster by connecting pixels to keep a record of their co-occurrence in association to the same signal. To limit the number of interconnections we only connect pixels that are adjacent in a particular ordering defined by a rule, e.g., by ascending order in time first, and ascending in frequency in second. This thus forms a chain where a pixel is connected to one pixel downstream,

and another upstream. The ordering rule may be adapted to the waveform morphologies of the targeted classes of signals.

We repeat this operation for different alignments in time between the waveform and the coarsest time-frequency lattice associated to the WDM transform with the largest analysis timescale. These alignments are obtained by shifting the waveform in time by multiples of the smallest analysis timescale. For the scale range $\ell = 3, \dots, 7$ used here, there is thus a maximum of $2^4 = 16$ possible alignments.

It is also repeated on every waveform signal associated with the considered astrophysical search, *ie.* the template bank. In this way we obtain as many pixel clusters as there are templates in the bank times the number of time alignments.

The collection of all pixels in the clusters form a graph². In Wavegraph, vertices are the pixels characterised by the central time, frequency and duration of the corresponding wavelet; and the edges are the links between pixels resulting from the ordering rule. Because the TF tracks associated with two distinct chip signals can intersect the chain of pixels can intersect as well leading to multiple interconnections between pixels in the graph. The ordering rule is primordial to ensure the graph is oriented (e.g., in time and/or frequency). A different ordering rule can be used depending on the phase evolution. These fundamental properties will be used further when searching for GW signals in data streams.

Wavegraph (412 nodes) generated with the following options:

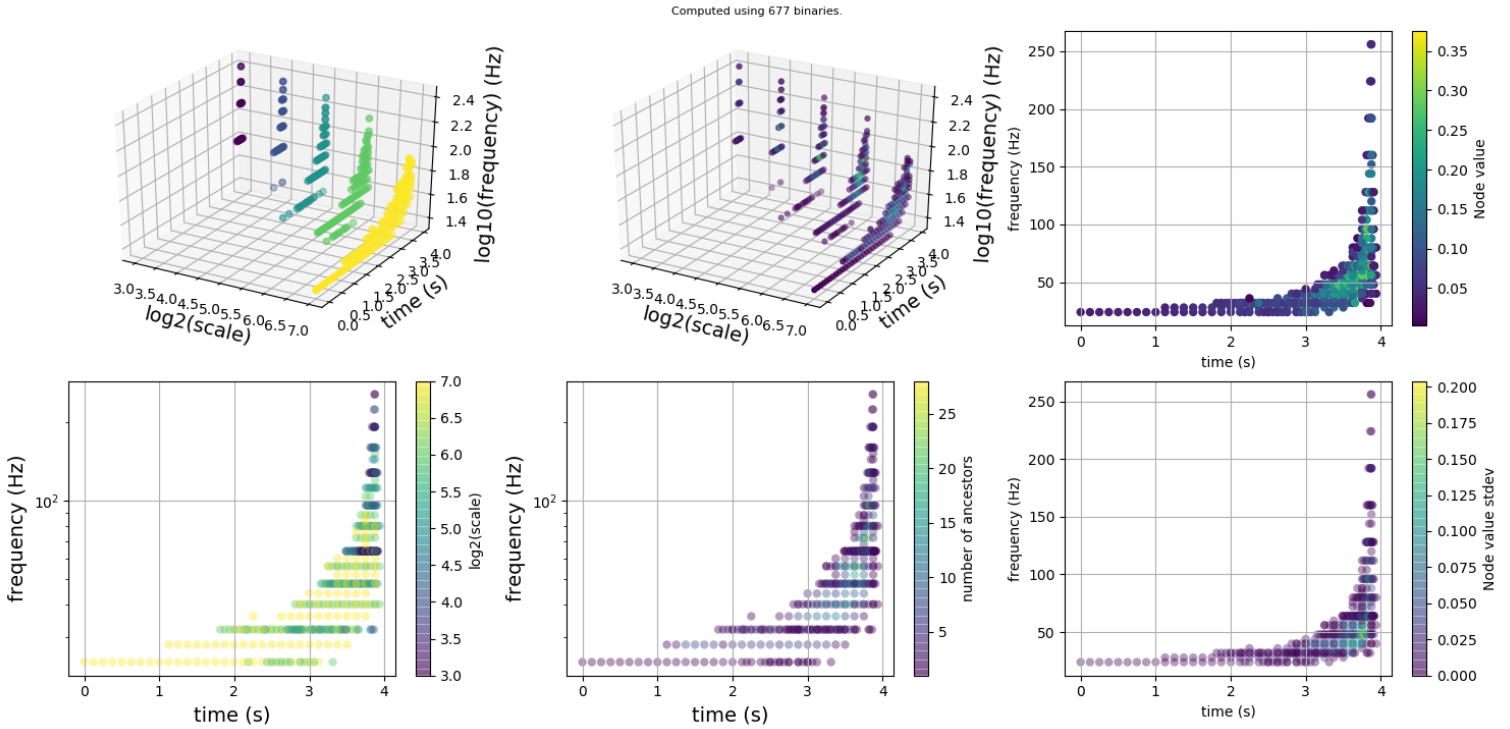


Figure 5.4: Wavelet graph generated by using 677 template **TaylorT4** waveforms whose mass lie in the 10 - $25M_{\odot}$ range. Each subplot displays a given quantity carried out by each vertex (mean value, standard deviation, scale/level). The graph is composed of 412 vertices indicating that many chirp paths share common pixels.

When multiple paths have a pixel in common, this pixel is assigned a value equal to the mean of the node values from all paths. We also store the standard deviation calculated over the intersecting pixels. Mean and standard deviation of the WDM coefficients distributions are associated to each node. Storing this information in the graph has an interest as detailed in the rest of the chapter. Both are represented on the two right subplots on

²A graph $G = (V, E)$ is a mathematical structure composed of vertices V linked to each other by edges E . *Oriented graphs* have edges that point from a vertex v_1 to v_2 . *Non-oriented graphs* have edges that are simply pairs of vertices. *Acyclic* graphs have no cycles.

Fig 5.4.

5.3 Search the observational data using the graph

The resulting graph provides a compact and convenient representation of the entire waveform manifold associated to a class of GW sources. It allows to use efficient search algorithms borrowed from graph-based combinatorial optimization.

Signals belonging to the targeted family can be searched for by analysing the cluster that best match with the data in the time-frequency-level space. Ideally we would search for the cluster in the graph that maximizes the likelihood ratio in Eq (4.21). However this would require the computation of \mathcal{L}_{max} over the sky grid which is too computationally expensive. Instead the cluster of pixels C^* in the graph G is identified that satisfies

$$C^* = \operatorname{argmax}_{C \in G} \sum_{p \in C} E_p - \lambda \bar{E}(f_p, M_p), \quad (5.7)$$

where $E_p = \sum_k \hat{w}_{p,k}^2$ with

$$\hat{w}_{p,k}^2 = \max_{\theta, \phi} w_k^2(t_p - \tau_k(\theta, \phi), f_p, M_p) \quad (5.8)$$

The first term of the sum in Eq (5.7) is a proxy for the cWB maximum likelihood ratio. Note however that E_p is an quantity analogous to the incoherent energy E_{inc} defined in the previous chapter. This is an attempt to collect the energy from a single GW signal observed by multiples observatories. It is similar situation to an array of photo-detectors which receives a luminous signal. The amount of energy received by the whole array is the sum of the the energy at each photo-detector.

The second term \bar{E} is an estimate of the noise level in a given frequency bin f_p and level M_p obtained by the median value of E_p at (f_p, M_p) for all times. It acts as an "Occam's razor" penalization term that favours selection of short-duration clusters. Without this penalisation, the maximisation would have the tendency to prefer large clusters that accumulate more noise than signal power. The parameter λ allows to tune the strength of this penalisation.

Procedure 2 Wavegraph dynamic programming algorithm

Input: acyclic and oriented graph $G = (V, E)$. V follows a topological order fixed by the ordering rule and contains values $\text{val}(p) = E_p$ ³ obtained from the data.

Output: cluster C^* , energy sum L

Initialise empty cluster $C^* \leftarrow \{\}$

Initialise energy sum $L \leftarrow 0$

for p in V **do**

 Update energy with the value of current pixel energy $L \leftarrow L + \text{val}(p)$

 Determine the set of pixels linked to p that are backward: $\mathcal{N}(p)$

 Initialise index and value of the maximum energy pixel in Q : $max \leftarrow 0$

 Determine the index of the maximum energy pixel among $\mathcal{N}(p)$: $m \leftarrow \arg \max_{n \in \mathcal{N}(p)} \text{val}(n)$

 Update the sum energy $L \leftarrow L + \text{val}(m)$

 Store new selected pixel in the cluster $C^* \leftarrow C^* + m$

return C^*, L

The maximisation problem is related to the class of "longest path" problems. The idea is to find the unique cluster of pixels collecting the maximum of energy with or without⁴ a constraint on its length. Many efficient and fast algorithms exist to address such problem acting on graphs. In Wavegraph, the longest path problem is solved by the *dynamic programming* algorithm [141] described in Alg(2) and represented on Fig 5.5. It is generically applied to graph optimisation problems and is based on a "divide and conquer" paradigm. In the

⁴Depending on the value of λ

Wavegraph case, the complexity of the algorithm scales with the number of connexions. That is why a graph complexity is estimated with the number of *ancestors* \mathcal{N} a pixel has in the graph, *i.e.* the number of edges between that pixel and its neighbours.

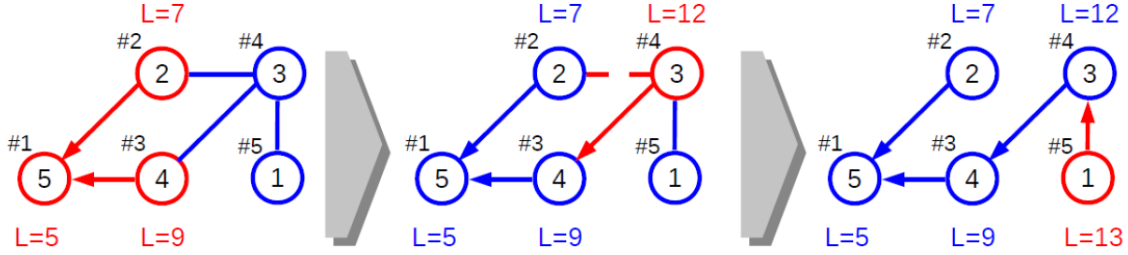


Figure 5.5: Dynamic programming algorithm flowchart. At each iteration, the algorithm estimates selects the pixel which maximizes the cumulated incoherent energy. On this example, pixel 1,3,4 and 5 have been selected and all form the extracted cluster.

Dynamic programming dominates Wavegraph computational cost. Overall the cost compares with that of cWB. Once the cluster of pixels C^* has been identified, the pipeline follows the post-processing steps of cWB. In the end the overall flowchart that combines Wavegraph and cWB is the one illustrated in Fig 5.6. The pre-preprocessing and graph computation are performed upstream the clustering step which occurs during the processing of interferometric data.

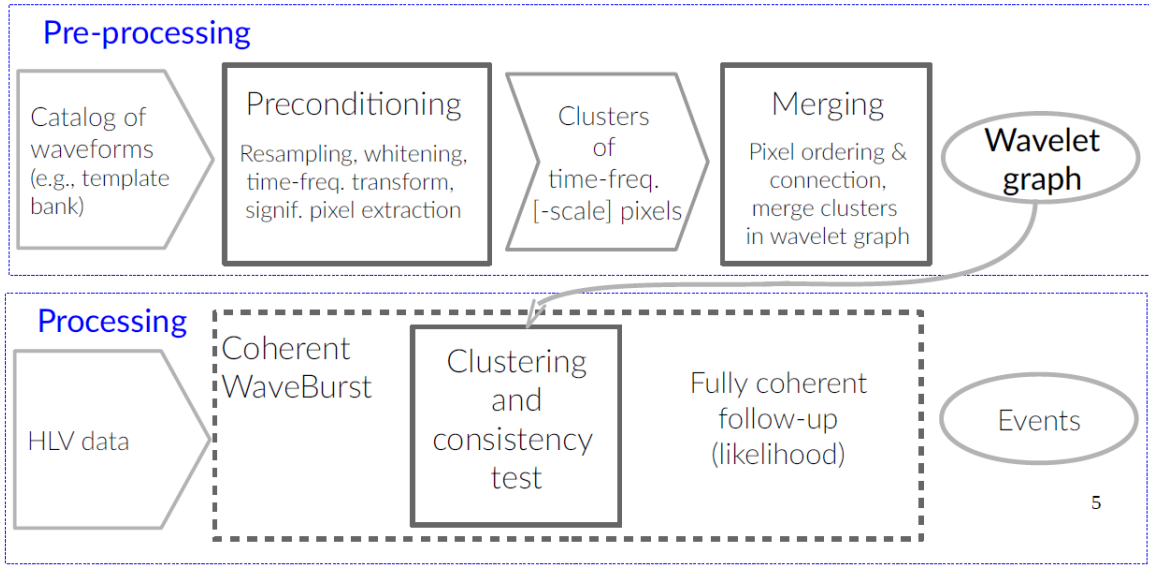


Figure 5.6: General overview of WG together with cWB. Steps relevant to cWB are inside the dashed line rectangle.

5.4 Comparison study: Gaussian noise case

In the present section, we show how Wavegraph performs in the context of a binary black hole search in idealised Gaussian noise. The goal of this first study is to demonstrate Wavegraph in the case of a well-characterised search. Graphs that correspond to the targeted parameter space are presented. We compare cWB and *Coherent WaveBurst with Wavegraph* (cWB+WG) backgrounds and sensitivity obtained in this context. All materials presented here are included in a published paper [1].

5.4.1 Time-frequency graphs

The BBH mass parameters space is divided into two disjoint regions. The region R1 (so called low-mass region) corresponds to a total mass range of 10 - 25 M_{\odot} , while R2 (higher-mass region) covers 40 - 70 M_{\odot} . The selected range of mass is similar to that of the BBH events observed during the first two LIGO observational runs. Also a different behavior of the Wavegraph method is expected in these two regions. For both regions, the mass ratio $q = m_2/m_1 \leq 2$ and the entire spin range of the available `SEOBNRv2_ROM_DoubleSpin` waveform model is covered. Note that the orbital eccentricity parameter is not taken into account in this model. Using the algorithm described previously the time-frequency graphs are computed relying on two banks of template waveforms (one for each region of the parameter space). Obviously those banks of signals are of different sizes as the template waveform space is differently populated depending on the mass range. So computing two graphs for two distinct parameter spaces has the advantage of allowing a comparison between graphs of different sizes and complexities. The R1 (resp. R2) bank of template waveforms includes 28201 signals (resp. 2950 signals).

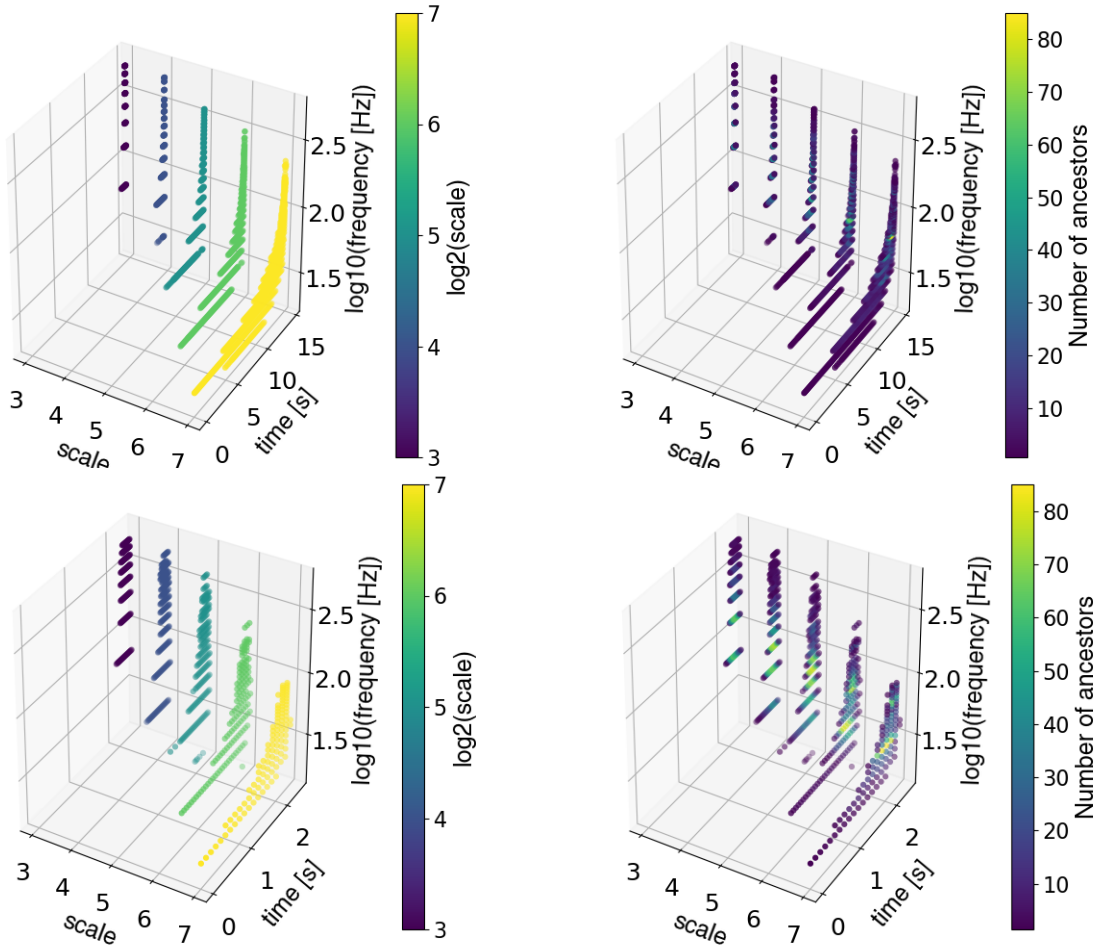


Figure 5.7: Time-frequency graphs used to search for BBH signals with the Wavegraph algorithm. Top graph corresponds to a low-mass region (total mass range of 10 – 25 M_{\odot}) of the parameter space whereas the bottom one corresponds to a higher mass region (total mass range of 40 – 70 M_{\odot}). The number of ancestors refers to the number of edges linking a given pixel to its neighbours. It is an indicator of the graph complexity.

Already there are clues for a difference in the graphs complexity since the low-mass region contains more signals thus the final graph will have a larger number of nodes. Moreover the associated duration is also very different: a longer signal in time will need a greater amount of wavelets to be reconstructed at a given reconstruction precision. It is then expected the R1 graph will have a larger amount of nodes for these two reasons. Template banks are generated using a stochastic placement algorithm [119]. This algorithm uses a Markov Chain Monte Carlo to sample the user-defined parameter space with a certain minimal match between a pair of neighbouring templates. In order to limit the overall computational cost for the time-frequency graph, the set of template waveforms is produced with a slightly coarser sampling in the R1 case with a minimal match of 95 % for R1

and 99 % for R2.

A limited number of waveform alignments have been used: only 1 for R1 and 32 for R2. Waveform alignments consist in time shifting a given template to account for the time resolution of the alrger level. Doing so for a single template signal we increase the number of nodes. This leads to a graph with 1643 pixel nodes for R1 and 941 nodes for R2 as shown on Fig 5.7.

5.4.2 Simulated data sets

To evaluate the impact of Wavegraph, we perform a Monte Carlo simulation. More precisely, we simulate 129 days of coincident data for a network of detectors composed by the two LIGO (H1, L1) and VIRGO (V1) GW observatories. The simulated noise is Gaussian and coloured according to the detectors design sensitivities [100, 101]. A set of gravitational wave signals with parameters in the targeted space is injected at random positions in time into the simulated noise. A given signal is injected several times to make possible its detection at various SNR values. Finally, the resulting data segment is analysed by the detection pipeline and we evaluate the fraction of the injected events that are recovered.

In the present study we compare the number of recovered injections by cWB and cWB+WG. To this purpose 10^6 binary black hole signals are added to the simulated noise. Injected binaries are arbitrarily oriented, isotropically and uniformly distributed in volume with a maximum distance of 1.4 Gpc for the R1 region and 3 Gpc for the R2 region. These distance values have been chosen to exceed the distance reach of the considered network for each search region. Cosmological effects are ignored and the simulated binary population is thus not exactly distributed uniformly in comoving volume. It is expected this have little impact on the results as we are primarily interested in the relative comparison of the search that is lead here. Moreover the bulk of injected and recovered sources is located at low redshift $z < 0.1$. The mass ranges of the simulated signals are also consistent though slightly larger than the span used to compute the time-frequency graph. As a consequence a small fraction of the injected signals may then fall outside of the time-frequency mass coverage.

5.4.3 Results

Background estimation

The first step to characterise a detection technique is to quantify the background of the search. To do so we apply the time-shift method developed in chapter 4. In the present simulation, around 600 time lags are applied to the simulated data in order to obtain an equivalent of 212 years of time-shifted surrogate data. The analysis of this noise-only data produces a search background, *ie.* the set of noise-related events detected by the pipeline and characterized by their detection statistics η_c , c_c and additional ones. In Fig 5.8 the FAR is represented against the η_c value. We compare the pipelines efficiencies at a reference FAR= 10^{-8} Hz. This rate is equivalent to 0.3 noise events per year.

The shape of a background curve obviously depends on the parameter space under investigation but also on the selection cuts that are imposed. These cuts will hopefully discard events whose cluster shape is too far from the one expected from a BBH cluster in our case. In the simulation a first selection cut on the correlation coefficient is imposed $c_c < 0.7$. It is a conservative value widely experienced by using cWB. A second cut helps rejecting events whose associated cluster has a time duration incompatible with the targeted sources. For instance, it is known stellar mass GW signals have waveform duration of the order of few milliseconds. A third selection cut is imposed when using cWB only which discards events with a non physical estimated chirp mass value. Chirp mass is estimated using a fit of relation (2.6) in the time-frequency plane. As it supposes a Newtonian order chirp the estimate is crude and serves only the purpose of selecting events. This selection cut does not improve the cWB+WG background in both regions. When all the cuts are applied this yields a background curve shown in Fig 5.8.

Both analyses using Wavegraph show a higher background curve than cWB alone. An explanation is that the clusters extracted using Wavegraph are, by design, larger on average and with a wider spread in time. Said differently the TF space investigated is larger. While cWB gathers sets of contiguous pixels with large amplitudes, Wavegraph allows for interruptions, since the pixels within the cluster remain selected despite they are far away or whatever is the overall energy. These two effects have the consequence to slightly expand the signal TF space accessible to Wavegraph which slightly results in a higher background. However extracting a long

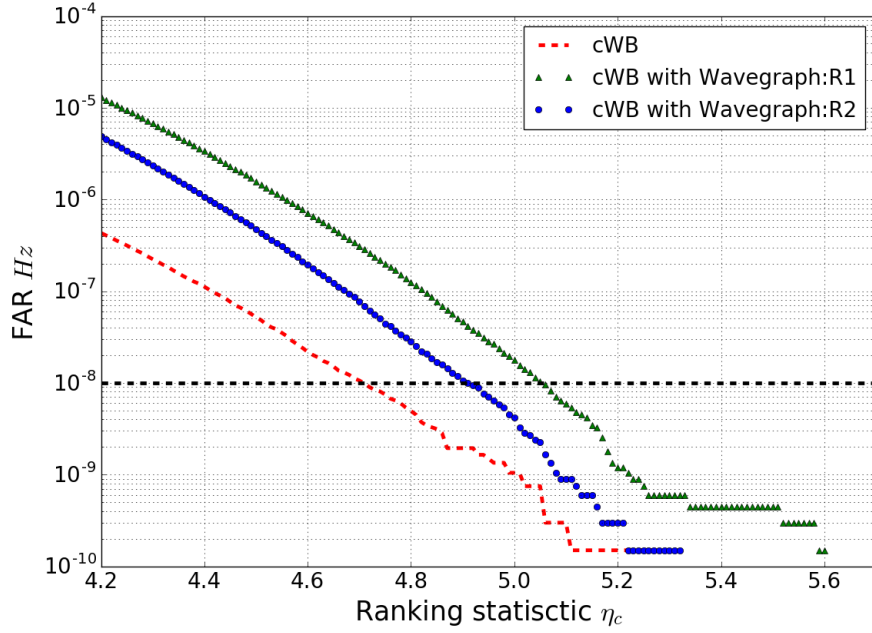


Figure 5.8: Background noise curves associated to the R1 and R2 graphs (see Fig(5.7)). These curves have been obtained by removing noisy events characterised by $c_c < 0.7$ and a duration greater than 5 ms. In the cWB case a third cut is applied based on a crude estimate of the chirp mass.

cluster facilitates the reconstruction of the signal at low frequencies.

The analysis using the R1 graph shows a higher background compared to R2. This is related to the increase in size and complexity of the graph, that has about twice more nodes in the R1 case, which thus increases the probability of picking up noise outlier. At the reference $\text{FAR}=10^{-8}\text{Hz}$ adopted here, the η_c selection threshold is 4.8, 4.9 (+2%) and 5.05 (+5%) for cWB, cWB+WG (R1 region) and cWB+WG (R2 region) respectively. The accuracy on the determination of those thresholds is estimated to be less or approximately equal to 0.6%. This estimate results in a linear approximation of the η_c cut at the considered FAR and assuming the uncertainties on the background points follow a Poissonian distribution. In the following, these selection thresholds on η_c are applied to declare a signal detected. Since this ranking statistic is homogeneous to the signal-to-noise ratio and is thus inversely proportional to the distance, it may be concluded that one loses few percent in distance reach by using Wavegraph. However it should be folded in the amount of SNR recovered on average in presence of a real signal as it will be discussed below.

Signal recovery

We now discuss various figure-of-merits and properties extracted from the recovered BBH signals detected by cWB and cWB+WG for each region of the parameter space. Table (5.1) displays the summary of injected and recovered BBH signals in both the R1 and R2 regions by cWB with and without Wavegraph. About $\sim 35 - 40\%$ of the events recovered with Wavegraph are missed by cWB alone (exactly, 14 627 and 11 402 for R1 and R2 regions respectively). Conversely, $\sim 15 - 25\%$ of the events recovered by cWB alone are missed when using wavegraph (exactly, 7 941 and 4 492 for R1 and R2 regions respectively). There is thus a good complementarity between the two pipelines.

Fig 5.9 shows the efficiency distribution for cWB and cWB+WG, that is the distribution of recovered injection divided by the injected network SNR. Left and right panels show the signal recovery from R1 and R2 regions respectively. For the two mass regions, the figures reveal that the use of Wavegraph improves the detection efficiency especially in the low injected network SNR region though we applied a more selective threshold on η_c to keep the FAR requirement equal for all searches. The distinction becomes clear above an injected SNR of 20 both in R1 and R2. The errorbars towards high injected SNR values are calculated assuming a Poisson distribution of recovered events. For the other events the large population of injection make the errorbar very small.

Algorithm	R1 region		R2 region	
	Injected	Recovered	Injected	Recovered
cWB	930 744	28 900 (3.1 %)	930 870	26 927 (2.9 %)
cWB+WG	930 744	35 340 (3.8 %)	930 870	33 699 (3.6 %)

Table 5.1: Number of injected/recovered signals by the simulation in the R1 and R2 regions for the two compared pipelines. Note the recovered signals indicated in the table are not exclusive to a single pipeline.

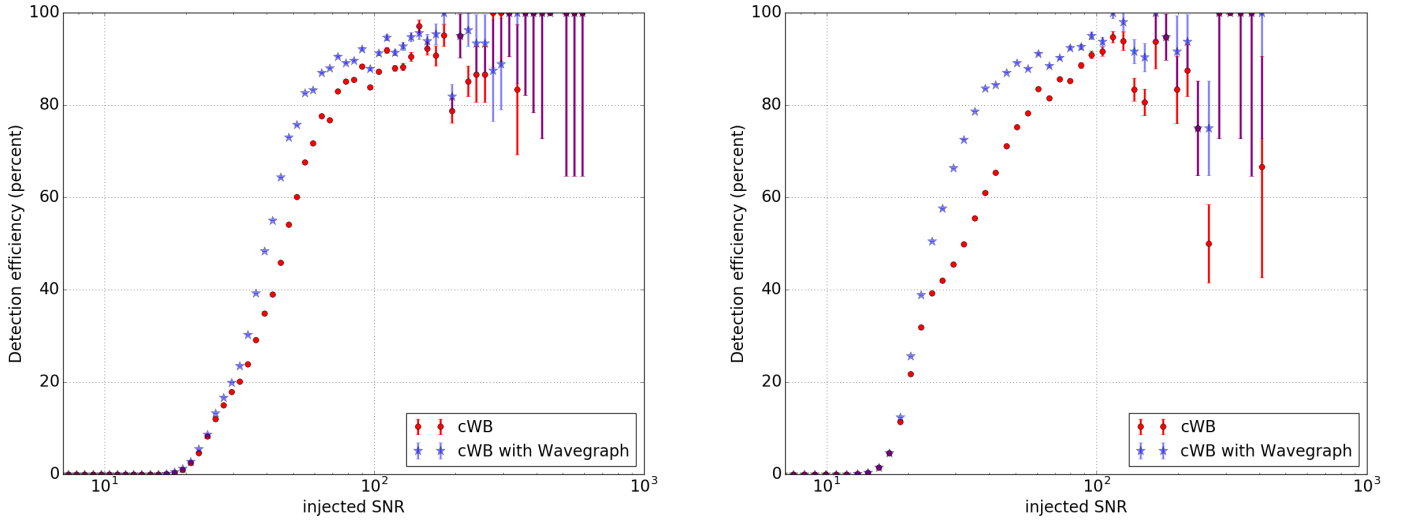


Figure 5.9: Efficiency curves for the R1 (*left*) and R2 (*right*) parameter spaces using cWB+WG and cWB+WG. Note the curve seem to decrease toward high injected SNR but this is the consequence of a very low statistic.

On Fig 5.10 is plotted the distribution of the network correlation c_c statistic for the signals recovered by cWB and with cWB+WG. It appears that using Wavegraph, the recovered signals have a higher c_c statistic for both R1 and R2 searches. Thank to the information extracted from the waveform model stored in the time- frequency graph, the Wavegraph algorithm is more likely to pick pixels relevant to the gravitational-wave signal itself, leading to an overall larger correlation. As a consequence it is believed this could serve GW signal reconstruction purposes.

Finally, detection pipelines like cWB detect GW events within a limiting distance. It is thus relevant to question the sensitivity to the search, *i.e.* how far can a given source be detected. To this aim Fig 5.11 shows the relative improvement in term of the distance reach for cWB+WG. The sensitive distance reach is estimated by computing the sensitivity distance of recovered injections integrated over the observation time, sky locations and binary orientations. The sensitive distance is computed over both mass ratio q and chirp mass \mathcal{M}_c bins (see Fig 5.11). In the R1 region, the average relative improvement in sensitive distance when using Wavegraph is $\sim 7\%$ with a maximum of 9.7% for the most asymmetric binaries ($q \sim 2$). The maximum relative improvement translates to a distance of 643 Mpc for the R1 region. In the R2 region, the average improvement is $\sim 8\%$ with a maximum at 13% in the lower part of this mass range. In term of distance the maximum improvement reaches 1257 Mpc but the farthest event recovered by cWB with Wavegraph is at 2017 Mpc. Overall, this translates into an improvement in the event rate of about 20 – 25% at a FAR level of 0.3 events per year. The relative improvement decreases with the total mass for a fixed mass ratio. As the total mass increases, the BBH chirp signal gets shorter and cWB is able to collect all relevant pixels. The dependency of the relative sensitive distance improvement with the mass ratio, for a fixed total mass is rather weak except for the low mass region.

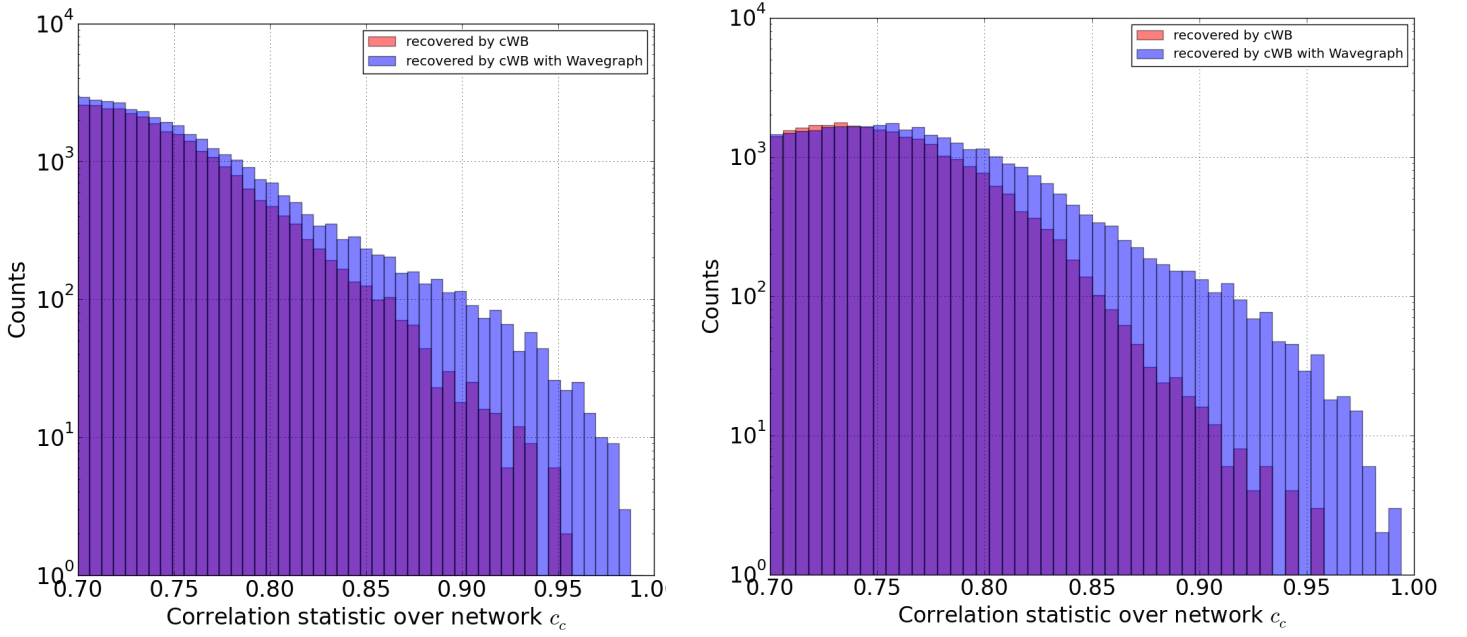


Figure 5.10: Histogram of the c_c detection statistic for the R1 (left) and R2 (right) parameter spaces using cWB and with cWB+WG.

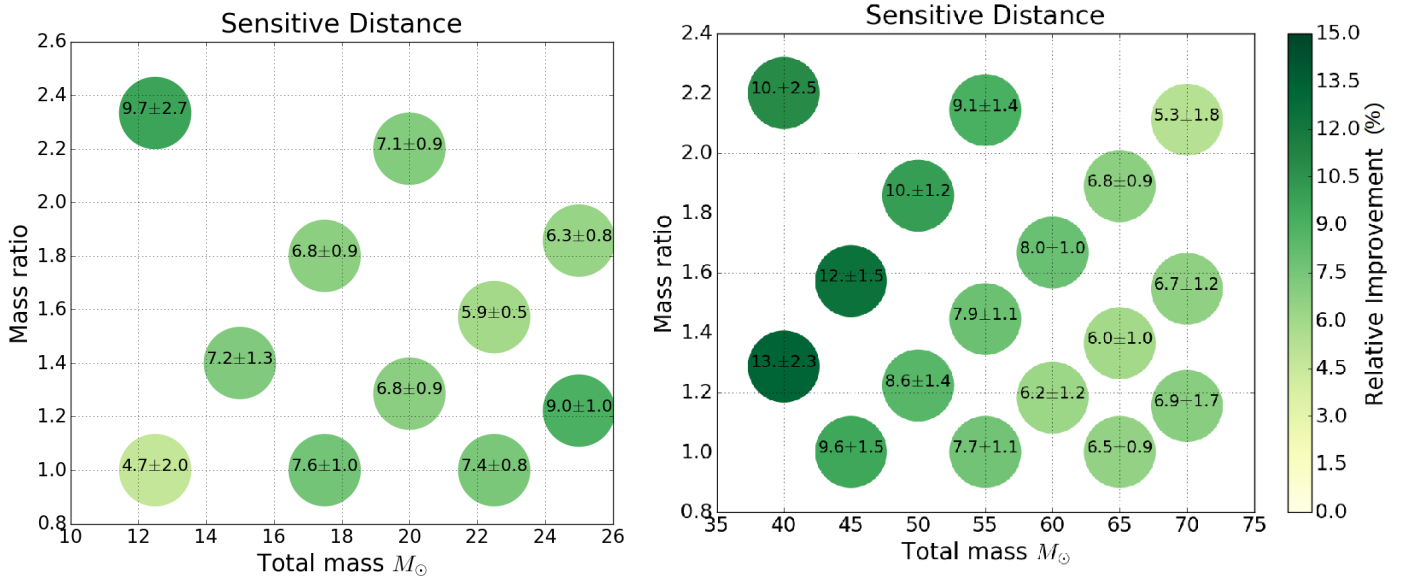


Figure 5.11: Relative improvement in sensitive distance for the R1 (left) and R2 (right) parameter spaces using cWB+WG at $\text{FAR}=10^{-8}$ Hz.

5.5 Comparison study: real noise case

This section delivers further precisions on the stages of the standard cWB search algorithm that improves the search efficiency by removing non-gaussian events. These are known as veto techniques and play a primordial role in the case of a real data analysis as one needs to deal with numerous non-gaussian features. They mainly arise from a variety of instrumental mechanisms. Despite the presence of auxiliary channels recording external disturbances affecting the instrument all transient noises cannot be identified and removed and thus remain in the analysed datasets. So it is important to mitigate the remaining non-Gaussian features while the GW signal search is performed. Specifically for cWB, the presence of loud non-Gaussian glitches affects the estimation of

the PSD but also the way clusters are selected. They lead to triggers with high η_c .

In what follows the existing glitch rejection strategies and selection cuts used by cWB are reviewed. A specific selection cut developed for Wavegraph is presented that combines with cWB vetoes. Finally it is studied how both perform when applied in the context of real data during the first run of the two LIGO instruments.

5.5.1 cWB gating and vetoes

Loud noise events occur often in LIGO-VIRGO data as 10^6 glitches above $SNR = 6$ were observed in 51.5 days of O1 data [142]. For a large fraction of those glitches the underlying cause remains undetermined. Glitches generally exhibit a short time duration comparable to that of the GW signals. This is why they are difficult to reject. A whole "zoology" exists that tries to classify glitches based on their morphology in the time-frequency plane [143]. A detailed description and visualization of the known types of glitches is available in [144].

Gating

Coherent WaveBurst includes a procedure to deal with non-stationary events and discard segments where every large spike occurred. It is called the *gating* procedure and defines a TF window with time width named TWIN and a frequency range from tens Hz to few kHz. cWB computes the total energy of the TF pixels in this window (see Fig 5.12). When the energy goes above a user-defined energy threshold SETHR (Time-integrated energy threshold), then the corresponding time interval (larger width) is not analysed. Noise events removed using the gating procedure are qualified as *super glitches* and as their name indicates are loud enough to be rejected at once. Typical values used by cWB are : $SETHR \sim 10^3$ and $TWIN = 0.5$ s.

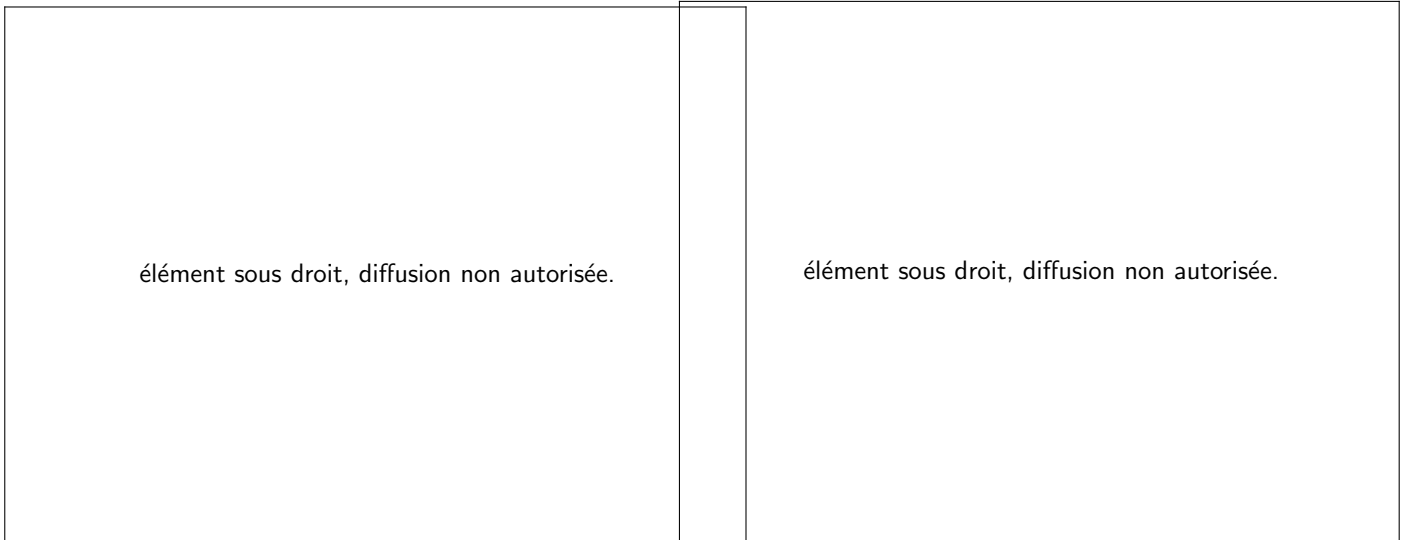


Figure 5.12: Gating procedure as implemented in cWB. (*Left*) Whitened time-frequency map containing two obvious excess power events on which a TF window is drawn. (*Right*) Estimated cluster energy as a function of time. If the TF window energy content goes above a user-defined threshold then it is vetoed as a super-glitch.

Vetoes

In addition to the gating procedure *vetoes* further constraint the admissible shape of the TF cluster. Such vetoes are applied at a later stage after the cluster is computed. This means cWB extract clusters with any morphology provided it passes a collection of selection cuts. The following bullets go through the selection cuts a candidate event (*i.e.* a cluster of pixels) should pass to be marked as a GW event candidate by cWB:

- **Norm cut:** The *norm* selection cut is as the ratio of the reconstructed amount of energy and the total energy over all the decomposition levels within the cWB grid. The logic behind this cut is the hypothesis that glitches present a simple morphology involving a single time-scale. glitches are thus decomposed over wavelets with similar shape and at the same decomposition level. The norm cuts thus aims at rejecting clusters whose energy is not well distributed over the levels.

- **Chi2 cut:** The χ^2 cut is defined as $E_n/N_{pix} \times K$ where E_n is the null energy (see Sec 4.2.2), N_{pix} is the number of pixels in the cluster and K is the number of detectors. The null energy is the energy remaining when the reconstructed signal is subtracted from the data. This cut verifies whether the residual is consistent with pure Gaussian noise. The normalisation comes from the number of degrees of freedoms and ensures the residual energy must be spread all along the cluster.
- **chirp (mass) cut:** This cut consists in fitting a Newtonian model whose TF evolution is only governed by the chirp mass. If the fit yields a non physical chirp mass value $\mathcal{M} < 1 M_\odot$ then the event is rejected.
- **Qveto:** GW signals emitted from coalescing binaries are expected to follow a phase evolution predicted by GR (see chapter 1). While not checking the accordance of the signal with GR it is still possible to evaluate how oscillating is the signal. Such an information is encoded in the *quality factor* of the signal. The approach is quite efficient on abundant blip glitches which appear as very short transient noises spreading on a large frequency band and a small number of oscillations. The *Qveto* thus with a low quality factor rejects the clusters. In practice the *Qveto* quantity measures the relative energy between the true maximum amplitude pixel and the other local maxima. If the energy disbalance is too abrupt then it means the signal energy is concentrated in few pixels. In the opposite case it means the oscillation is sustained and more likely to be associated with a coalescing binary.
- **Lveto** deals with the nature of the GW detectors themselves. Indeed several narrow-band glitches are regularly observed in the data around 60 Hz. They arise due to the imperfect electronic shielding and magnetic coupling to the mirror suspensions. Similarly to the *Qveto* approach (but this time along the frequency axis) the *Lveto* algorithm evaluates the energy spread over several frequency bands. If the energy is too concentrated around a central frequency then the cluster is discarded.

Fig 5.13 displays background and injected GW events together with one of the above selection cuts. These ones perform reasonably well in splitting the two populations. Determining the selection cuts thresholds is not simple in the case where the two populations show an important overlap like for the *Qveto* and norm distributions.

5.5.2 A glitch rejection algorithm for Wavegraph

In addition to those selection cuts we propose a new algorithm for Wavegraph to reject spurious GW candidate events. The selection cuts used by cWB rejects clusters based on time-frequency morphologies heuristically associated to glitches. The clusters obtained with Wavegraph are by construction compatible with the targeted physical model. The graph includes both the phase and amplitude information (see 5.2). The phase information is encoded in the time-frequency and level position of the pixel nodes while the amplitude information is itself carried by the nodes ⁵. This information on the amplitude can be used to separate signal and glitches.

Using the notations of Sec 4.2.2, the WDM coefficient amplitude $w_{norm,k}[i] = w_k[i] / \sum_i w_{k_i}[i]$ is associated with the graph node i where $w_k[i]$ is the noise-scaled template time-frequency map at level k . Graphs contain a large number of overlapping chirp paths. To combine their amplitude profiles we average altogether the $w_{norm,k}[i]$ values coming from all chirp path passing by i , and compute their standard deviation $\sigma_{mod,k}[i]$. These quantities form the model signal amplitude and are stored in the graph (the R1 and R2 graphs in the present case). We estimate the weighted Euclidean distance between the model amplitude contained in the graph $w_{mod,k}$ and the observed signal amplitude O_k using a χ^2 -based test denoted T and called the *consistency test* (CT).

$$T = \frac{1}{N_{pix}} \sum_{(i,k)} \frac{(O_k[i] - A_{mod,k} w_{mod,k}[i])^2}{A_{mod,k}^2 \sigma_{mod,k}[i]^2} \quad (5.9)$$

where N_{pix} is the number of pixels present in the cluster and the overall amplitude $A_{mod,k}$ is computed in order to get the proper scaling by

$$A_{mod,k} = \sum_i \frac{w_{mod,k}[i] O_k[i]}{\|w_{mod,k}\|^2} \quad (5.10)$$

⁵The amplitude uncertainty arising from multiple crossing chirp paths is also stored in the nodes

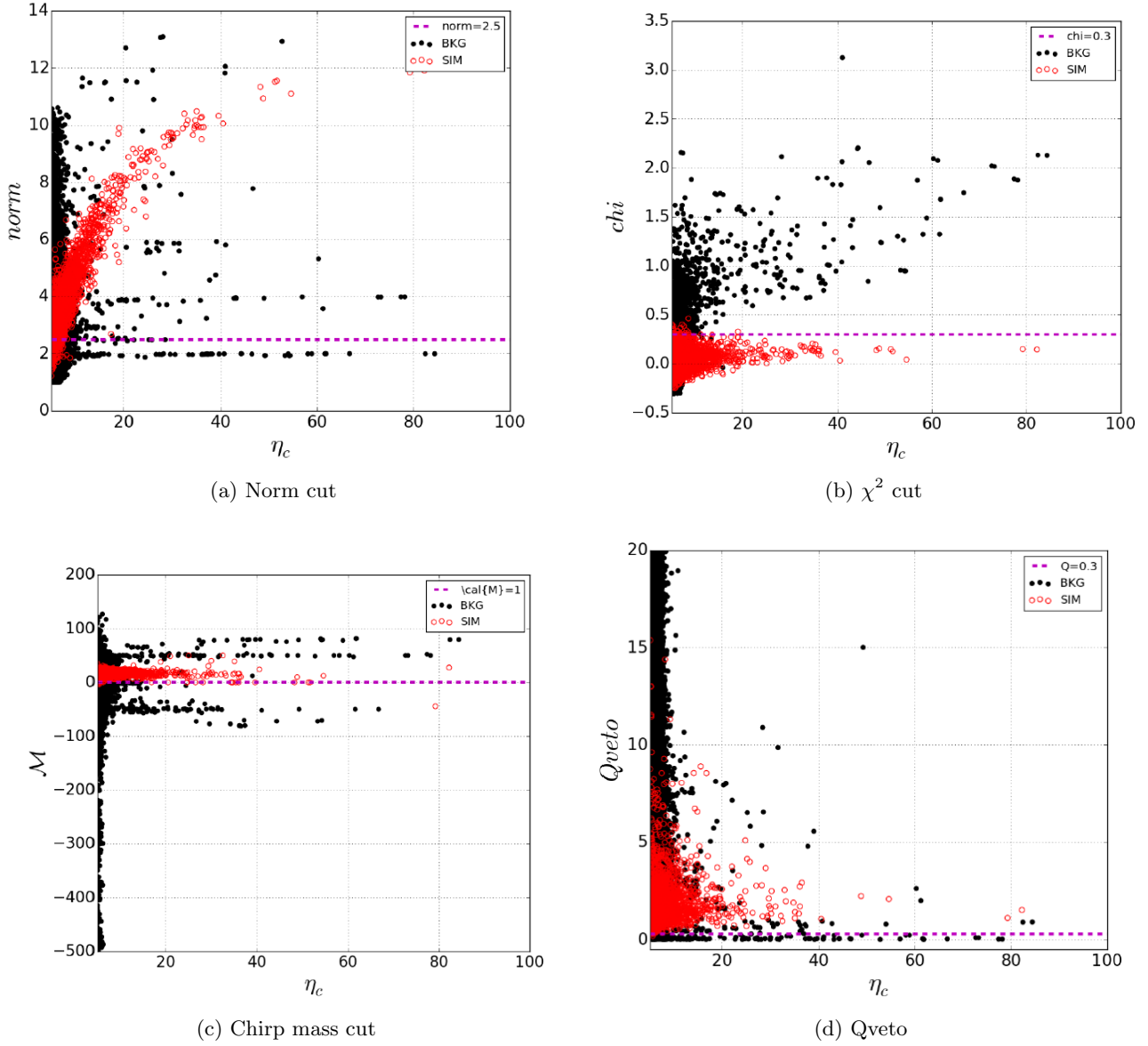


Figure 5.13: Ensemble of vetoes applied in the context of cWB searches (Credits: Gayathri V.)

where $\|w_{mod,k}\|^2 = \sum_i w_{mod,k}^2[z]$ is a normalisation level-dependent constant. The quantity T measures the deviation that may arise between the model and observational data. As shown on Fig 5.14, if a glitch is present in the data then it is expected to show a discrepancy with respect to the template graph. In this case the distance measured by the CT is likely to be large whereas if the candidate event is a true GW the χ^2 distance is expected to be small (provided the cluster lie in the same parameter space as the graph).

To reduce the effect of the level-dependent contribution from the "Gaussian" noise in the summand of Eq (5.9), an offset and rescaling corrections have to be introduced in Eq (5.9) [2]. We will not detail this here. Like other selection cuts the determination of the threshold is a compromise between rejecting a maximum amount of transient noise events while preserving the population of recovered events. Such a trade-off is evidenced by Fig 5.15.

Note that we are not simply cutting upon T but by a strength-scaled version of the consistency test namely T/ρ where ρ denotes here the effective correlated SNR. In the end we choose $T/\rho = 1.5$.

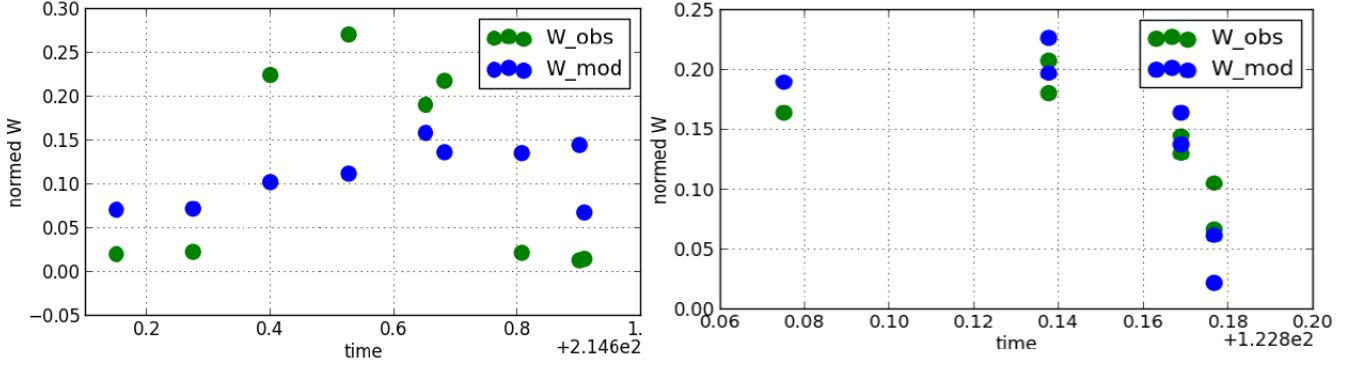


Figure 5.14: Wavegraph consistency test applied to a transient noise event (*left*) and to a GW signal (*right*). The blue points correspond to the model amplitude coefficients stored in the graph while the green points are the amplitude coefficients obtained from the data.

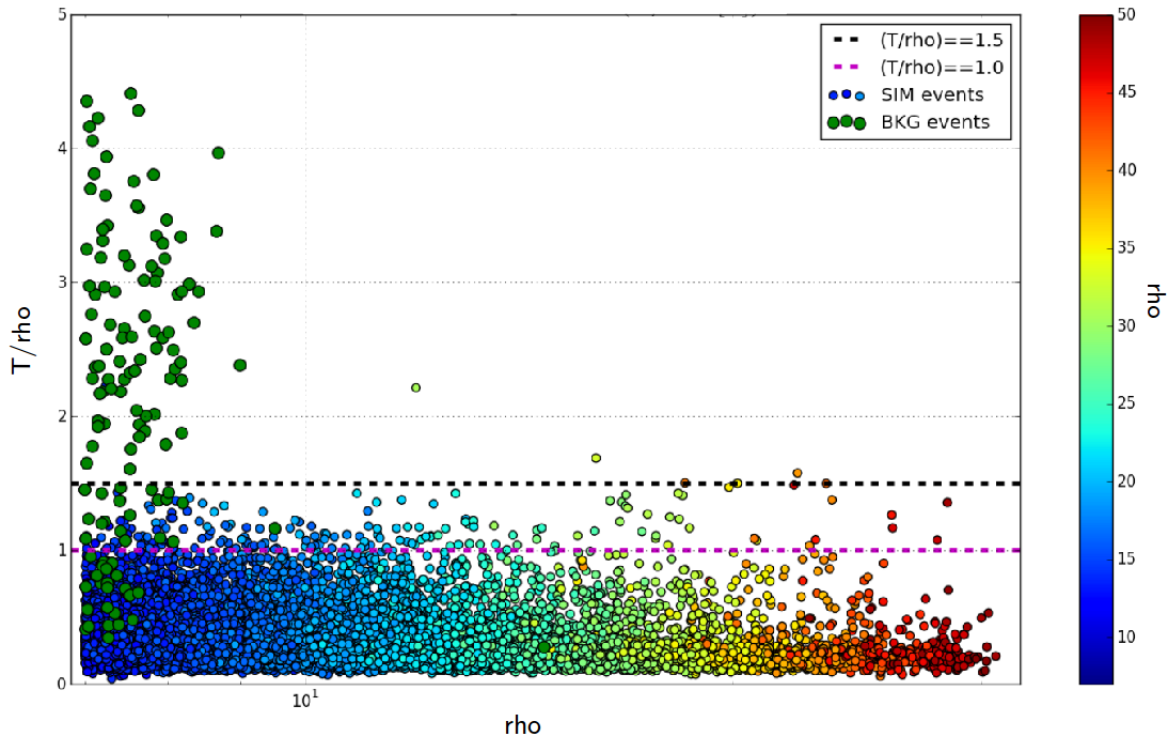


Figure 5.15: Wavegraph consistency test applied to a population of background and simulation events. The two proposed thresholds $T/\rho = 1$ (dashed purple line) and $T/\rho = 1.5$ (dashed black line) illustrate the cutting trade off.

5.5.3 Running Wavegraph with consistency test in O1 data

The background estimation and sensitivity studies are performed here using science data from O1 run. The cWB vetoes, gating and the Wavegraph consistency test are used to mitigate the contribution of transient noises to the background.

Time-frequency graphs

We produced time-frequency graphs for the R2 region using the O1 sensitivity. The parameter space is split in a similar fashion as in the Gaussian noise case so as to allow a direct comparison. The motivation is that the efficiency of the consistency test will likely be better demonstrated if transient noises lie along loud and short duration cWB signals. Total mass covers the 40 - 70 M_{\odot} range with mass ratio $q \leq 2$. The spin values span the entire spin range available for the used `SEOBNRv2_ROM_DoubleSpin` approximant. As the waveform template

density is not too important in this region of the parameter space the required minimum match between two neighbouring templates is fixed to 99 %. The overall setting is the same as the R2 graph shown in the previous study. It has been empirically demonstrated that the consistency test performs better in the case of an augmented statistics over the graph nodes. Indeed by fixing the number of time-shifts to 32 (this value is used in what follows) each template in the bank is processed 32 times with various end times. Although it represents an additional computational cost it will lead to better results in terms of glitch rejection.

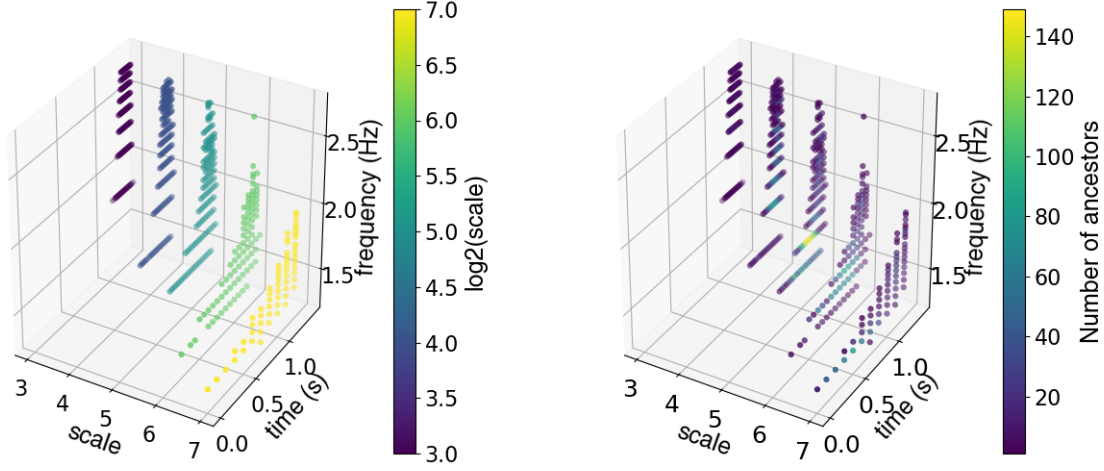


Figure 5.16: Time-frequency graphs used to search for BBH signals with the Wavegraph algorithm in O1 noise

The resulting graph (see Fig 5.16) is composed of 619 nodes which is less than the R2 graph of the Gaussian noise study. The only difference with the Gaussian noise study is the refined cWB grid that is used here. It follows that for a given number of time-shifts, a refined grid yields less nodes due to the degeneracy of the grid. Fig 5.16 also evidences a higher number of ancestors with respect to the previous study (~ 150 here and ~ 90 before). The graph has thus gained in complexity.

Effects of the consistency test on the background

The simulated set of injected signals in O1 data is strictly identical to the Gaussian noise case. Background curves are shown in Fig 5.17 where we demonstrate the effect of the consistency test. The cWB curve is lower than when including WG. The justification for this remains the same as in the previous case: the time-frequency span of WG clusters is larger and thus more prone to noise fluctuations. The application of the CT diminishes the tail of the background by 10% at a reference FAR of 10^{-8} Hz.

Sensitive distance

We look at the sensitivity of the search and more precisely at the impact of the consistency test on the recovery of the search. Indeed the selection cuts imposed when studying the rejection of background noisy events must of course be also used while estimating the distance sensitivity of the search.

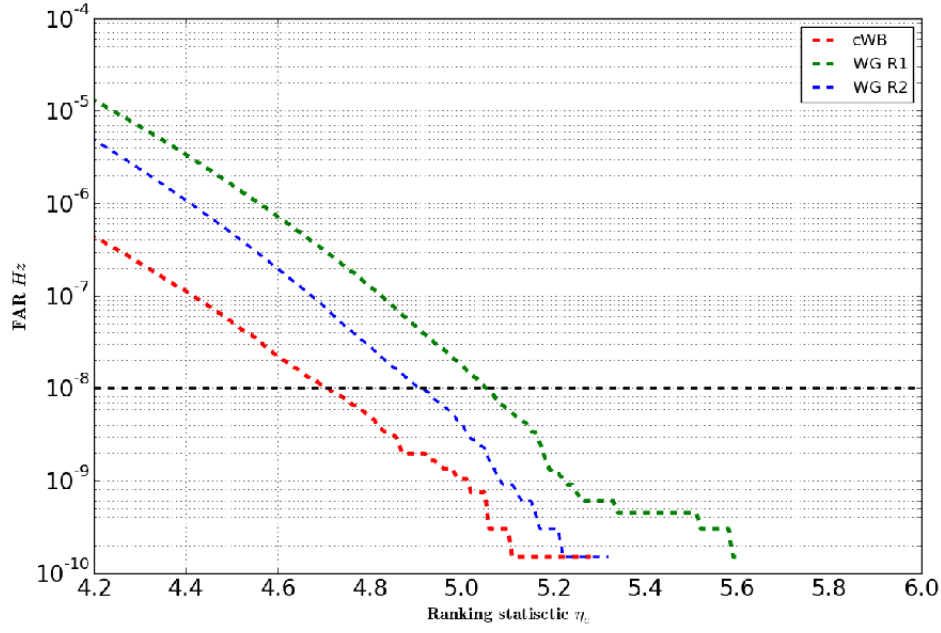


Figure 5.17: Background curve comparison between cWB and cWB+WG for real O1 detector noise. The application of the consistency test reduces the background tail thus reducing the selection threshold on η_c

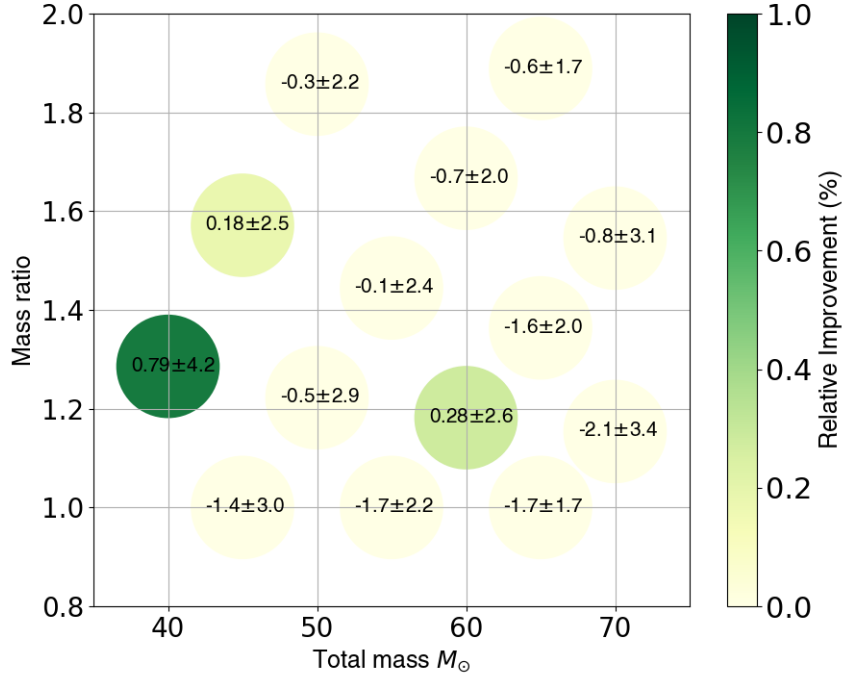


Figure 5.18: Sensitive distance improvement diagram for cWB+WG with respect to cWB alone in BBH searches in O1 data at $\text{FAR}=10^{-8}$ Hz.

Fig 5.18 shows that cWB+WG do not perform as well as cWB+WG alone and this despite the application of the consistency test. The two greenest bins have a mean relative distance below 1 but both are consistent with an improvement within a 1σ confidence interval. A next test would be to repeat the simulation with more injection statistics in order to confirm whether Wavegraph brings any improvement in the probed distance. Indeed, recovering an injected event is a rare event which follows a Poisson statistic. Hence errorbars in Fig 5.18 scale as $1/\sqrt{n}$. Given a lack of statistic it is difficult to state any particular dependency of the improvement with respect to the total mass or the mass ratio.

Chapter 6

Searching for eccentric black hole binaries with Wavegraph

Contents

6.1	Eccentric binary black hole signals	78
6.1.1	Approximant and time-frequency representation	78
6.1.2	Time-frequency graphs	79
6.2	Population model	81
6.3	Comparison study	83
6.3.1	Preliminary study	84
6.3.2	Results with the "fully eccentric" graph	87

In chapter 4 we proposed Wavegraph as a solution for exploring extreme parts of the parameter space. In the present chapter we propose to study Wavegraph behaviour when considering stellar mass black hole binaries whose orbit shows some significant deviations from the circular geometry discussed so far.

In the first part, we first discuss what is the current status of eBBH models, then we discuss some features of eccentric waveform signals in the time-frequency domain. In a second part we present an astrophysically-motivated model that explains a population of eccentric mergers. Finally the third part is devoted to a comparison study between searches in the context of eccentric searches using O1 data.

6.1 Eccentric binary black hole signals

In Sec 2.3.2 we reviewed eccentric systems of stellar mass binary black holes and their gravitational wave emission. In this section we describe how eccentric time-domain waveform signals are modelled and what is their morphology in the time-frequency domain.

6.1.1 Approximant and time-frequency representation

Eccentric waveform models

Gravitational wave emission models for eccentric systems are not yet complete and there are several reasons for this incompleteness. First, models focus on the inspiral part only [145, 146, 138, 147, 148, 85]. While this may be the most interesting fraction of the signal as its eccentricity is still significant before the orbit circularizes, the subsequent merger phase is expected to dominate the SNR in the LIGO/VIRGO band. The inclusion of the final part is in progress through effective-one-body approaches [149, 150] or numerical relativity [146]. A second caveat is the absence of higher order modes. In Sec 2.3.2 we show that orbital modes contributes differently depending on the eccentricity through the $g(n,e)$ function in Eq (2.30). Current eccentric waveform models rely on the lowest order $(\ell, |m|) = (2, 2)$ approximation. As shown in Fig 2.11 the higher the eccentricity the larger the higher order mode contribution. For this reason the $(2, 2)$ order models are not valid beyond $e \sim 0.4$ at $f \sim 20$ Hz. Having higher order modes is important for modelled searches and parameter estimation purposes [151]. High eccentricity ($e > 0.7$) waveform models exist [82, 152] for bounded and unbounded systems but are

applicable in the low frequency range around 10 Hz below the current detector bandwidth.

In this chapter we use the 2PN order inspiral waveform to model eccentric binary black hole mergers. This approximant is described in [85] and is called **EccentricTD** (see Fig 2.10). With a 2PN approximation we can reach quite high eccentricities depending on the low frequency cutoff f_{low} and component masses. For instance, a 10 - 10 M_{\odot} eccentric black hole binary with $f_{low} = 20$ Hz can be generated with eccentricity upto $e = 0.67$. The range of eccentricities spanned by this model essentially covers all GW signals accessible to current and future ground based instruments. Finally, the **EccentricTD** waveform model does not account for spins.

Time-frequency representation of eccentric GW signals

In order to better understand what are the features specific to eccentric signals we look to time-frequency representations.

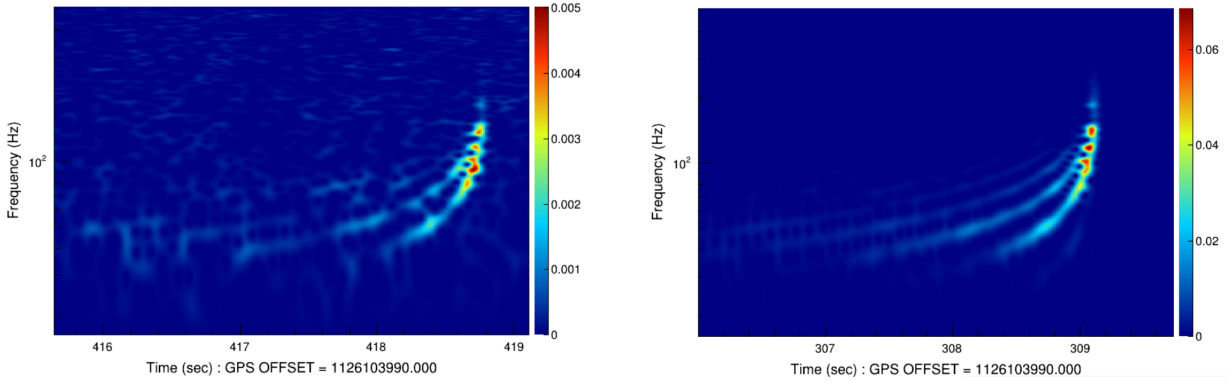


Figure 6.1: Eccentric binary black hole signals in O1 data with SNR=91.8 (*left*) and SNR=207.6 (*right*). The source is a 10 - 10 M_{\odot} non-spinning binary with eccentricity $e = 0.5$ at $f_{low} = 20$ Hz. The orbital mode tails get buried in the instrumental noise as the SNR decreases.

Fig 6.1 displays a GW waveform emitted by a 10 - 10 M_{\odot} non-spinning eccentric binary with eccentricity $e = 0.5$ at $f_{low} = 20$ Hz. The majority of the signal energy is concentrated in the dominating mode $n = 4$ (see $e = 0.5$ curve in Fig 2.11) but a significant amount of energy is present in sub and upper harmonics. The Newtonian order expressions for the GW radiation in Eq (2.20) and Eq (2.21) involve $\sin(n\phi)$ and $\cos(n\phi)$ functions of the orbital phase up to $n = 3$. On the right subplot of Fig 6.1 where the overall signal is louder, one can guess weaker harmonics on either side of the harmonic with $n = 3$ in accordance with Eq (2.30). The harmonics together with the fundamental mode join as the orbit circularises. This is just a consequence of the finite time and frequency resolutions of the cWB TF grid. As a consequence, the late time part of the time-frequency representation looks like that of a circular merger (see middle panel of Fig 5.3). Harmonics become less visible for smaller SNR.

6.1.2 Time-frequency graphs

A better algorithm for pixel selection

To compute the time-frequency clusters of eccentric template waveforms we use a variant of the matching pursuit algorithm used previously in Sec 5.1.2. The *updating matching pursuit* (UMP) is one of the algorithms we tested in [3].

The UMP includes an additional step to the original MP, that consists in updating at each iteration the values of all the pixel coefficients to minimize the residual error. The residual error decays faster thus leading to fewer selected pixels. The overall computational cost is slightly increased by the presence of the new step as it implies transforming back and forth from the time-domain to the time-frequency domain.

Fig 6.2 evidences the difference in sparsity between the MP and the UMP. The UMP needs less pixels to approximate the input signal at a given approximation level. Quantitatively the MP decomposes the waveform shown on Fig 5.3 in 52 iterations (or numbers of pixels) while the UMP achieves the same in 47 iterations. This is a 10% improvement in sparsity. The other algorithms investigated in [3] propose even sparser solutions but

they need a much larger computing cost.

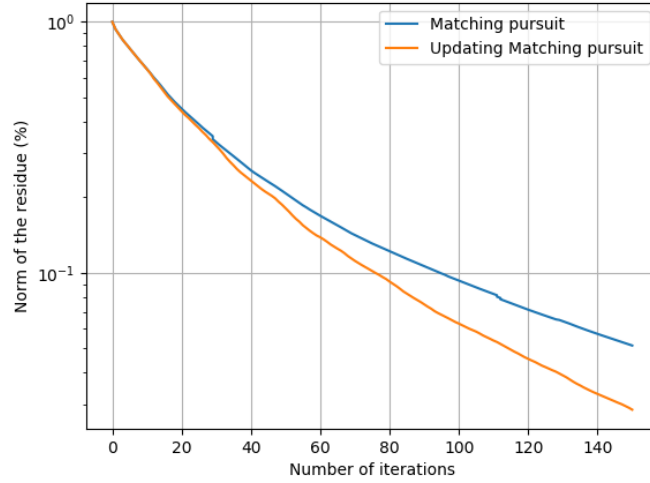


Figure 6.2: Comparison between the convergence of the matching pursuit (blue) and the updating matching pursuit (orange). The test source is a 10 - 10 M_{\odot} non-spinning compact binary with eccentricity $e = 0.5$.

Template bank for eccentric waveforms

Template-dependent searches rely on *a priori* knowledge of the signal that it is looked at in the data. Such a knowledge is encapsulated in a sub-domain of the parameter space describing the source. In the present case the parameter space is the classical circular template bank composed of 9, 11 or 15 dimensions (depending on the the assumption made on the components spins) plus the eccentricity dimension. The chosen waveform approximant **EccentricTD** is then simply an extension of the **TaylorT4** spinless model [84] with eccentricity. It results in a 10-dimension parameter space. The eccentricity parameter induces a larger phase variability in the signal than spins for instance. We expect for new features when computing the graph and also when performing the search in the case of eBBH searches.

We consider a parameter space non-spinning stellar mass black holes in the mass range from 10 to 25 M_{\odot} (with $q \leq 2$). The minimum GW frequency is fixed to $f_{low} = 20$ Hz in agreement with the low frequency cut-off of current instruments. The eccentricity ranges from 0.05 to 0.58. The lower bound is chosen to include quasi-circular inspirals¹ while the upper bound is an intrinsic limit of the **EccentricTD** approximant. The maximum reachable eccentricity depends on the total mass and is determined by the heaviest binary. Quantitatively a 5 M_{\odot} total mass binary with whatever reasonable mass ratio cannot exceeds $e = 0.68$ and a 30 M_{\odot} binary is limited by $e = 0.62$.

As already stated there is not yet strong involvement in searching for eBBH systems using matched filtering searches. Most actual searches for eBBHs concern unmodelled searches [76]. Template placement algorithms are not yet able to handle eccentricity [119]. We have followed a pragmatic approach for building the template bank. We produce a circular template bank described by the **TaylorT4** waveform model and sample the eccentricity axis regularly by steps of 0.05 which we estimate to be a conservative choice that prevent under sampling.

Time-frequency graph

Using the procedure of Sec 5.2 we generate an "eccentric graph", *i.e.* a graph computed from the template bank of the previous section. In what follows we use an analogous appellation for "circular graphs". No time-shifts have been performed in this study. The eccentric graph is displayed in Fig 6.4. It includes 3262 nodes which is comparable to the R2 circular graph shown in Fig 5.7.

¹Technically the generation of an **EccentricTD** waveform with $e = 0$ is not permitted.

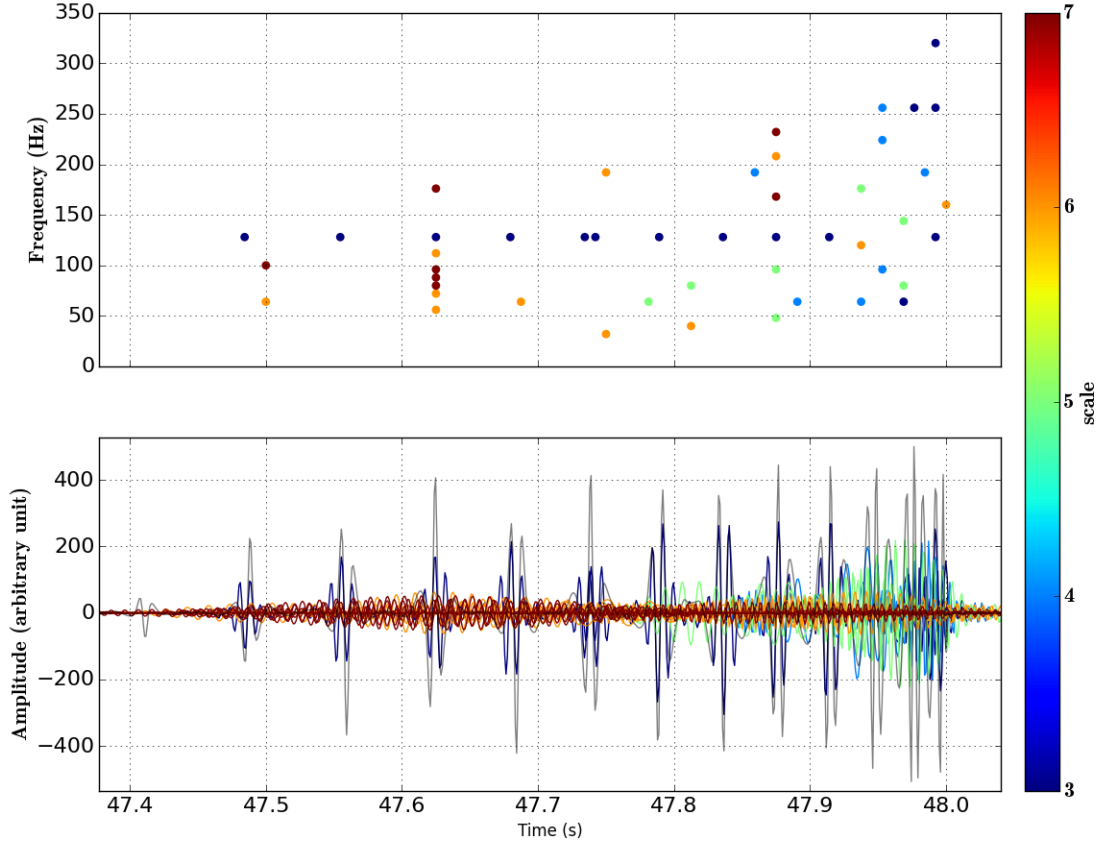


Figure 6.3: Pixel selection resulting from the updating matching-pursuit algorithm in the case of an equal-mass non-spinning eBBH waveform with total mass $20 M_{\odot}$ after whitening by advanced LIGO design sensitivity PSD. The eccentricity of the binary is set to $e = 0.5$. Fixing the termination condition at 20 %, the final cluster collects 47 pixels in accordance with Fig 6.2 (*top*). Time-frequency pixels selected by the updating matching pursuit algorithm (*middle*) and corresponding wavelets (*bottom*).

A striking feature in Fig 6.4 is the presence of constant frequency lines of pixels. These lines match well with the harmonics discussed earlier in Sec 6.1.1. They belong to the sub-population of high eccentricity templates in the template bank since those pixels have a (very) low number of ancestors (see right subplots). It is corroborated by the fact that all these pixels are selected at scale 3 (see left subplot of Fig 6.4 and also Fig 6.3). Said differently these short-duration wavelets better fit the serie of GW bursts during the inspiral (see chapter 1 and Fig 6.3). These pixels appear in line because of the coarse resolution in frequency at low levels. The frequency variations are smaller than the grid resolution and thus appear as a constant frequency (see Fig 6.1).

6.2 Population model

In chapter 5 we did not simulate sources according to a formation model for the compact binaries. Here instead we distribute the injection set according to astrophysically-motivated distributions taken from [76]. This article describes the properties of eccentric binary black holes belonging to the segregating population toward the center of Milky-Way-like galaxies (see Chapter 3) [73].

Following this model, individual masses are drawn from the Salpeter initial mass function [18]. It consists in a power-law distribution of the form $dN/dm \propto m^{-\beta}$ where β is a parameter of the model which also scales with the mass of the central supermassive black hole. In what follows we will fix $\beta = 2$ and consider a central black hole with a mass equal to the one of *SgrA** ($\sim 10^6 M_{\odot}$). The use of the Salpeter mass distribution is not well suited to the modelling of a population composed of compact object since the initial mass function is by

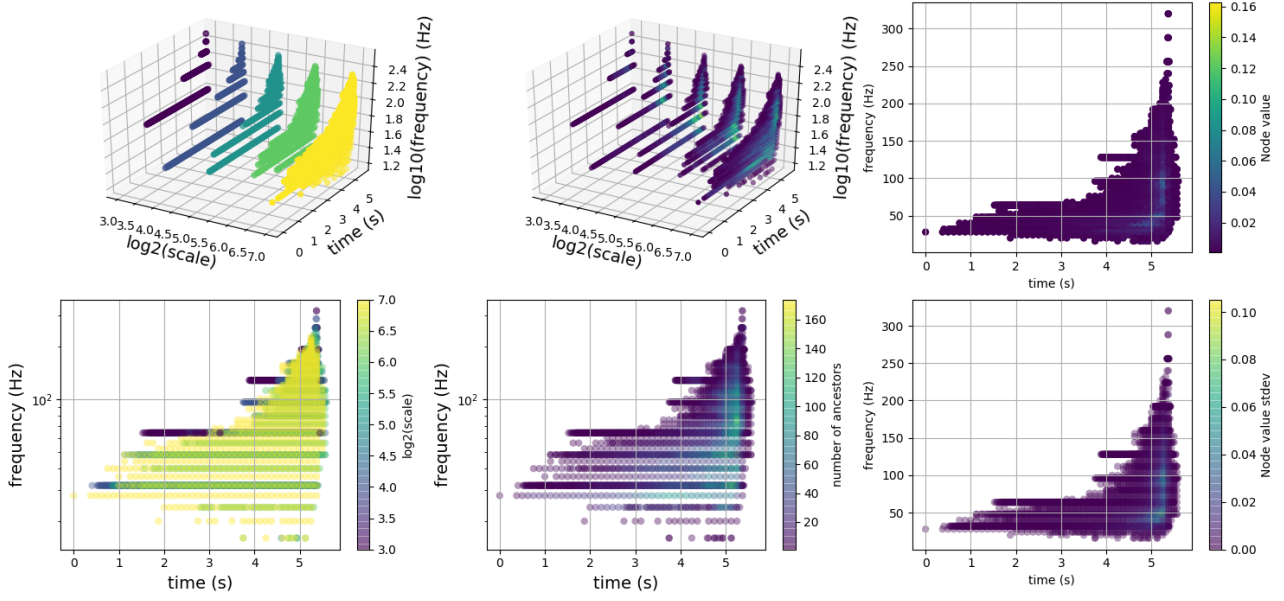


Figure 6.4: Time-frequency graph used to search for eBBH signals with the Wavegraph algorithm.

definition a mass distribution of stars before they enter the main sequence. It would have had a sense if the simulation evolved a population of pre-MS star distributed with the Salpeter distribution until the stage where they turn into a sub-population of black holes. We drawn individual masses between 10 and $25 M_{\odot}$ with a mass ratio of $q \leq 2$. The simulation accounts for the expansion of the Universe and the masses are thus redshifted *i.e.* multiplied by $(1+z)$ where z is the redshift of the source. For this reason the component mass distribution used in the present study and shown on Fig 6.5 ranges from $10 M_{\odot}$ to $\sim 34 M_{\odot}$. This is justified by the fact that the injected signals are emitted until a luminosity distance equal to 2 Gpc which corresponds to $z = 0.37$ using cosmological parameters from Planck [30]. The maximal mass an observer on Earth can observe is thus $25 \times (1 + 0.37) \sim 34 M_{\odot}$.

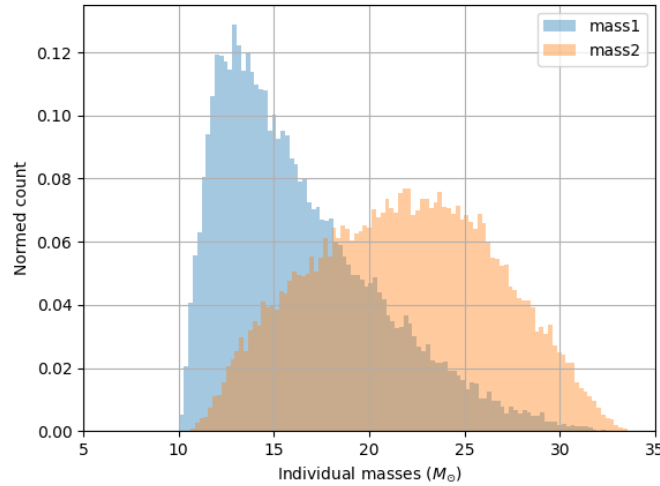


Figure 6.5: Binary component redshifted masses distributions used to generate the injection set.

The luminosity distance distribution is a bimodal distribution different from the one adopted in [76] where they used a r^2 distribution. The positions of the peaks do not correlate with the expected physical distance of over-densities mentioned in [73], but rather to a fiducial source distance which scales with the chirp mass of the source by

$$R_{fig}(\mathcal{M}_c) = 540 \left(\frac{\mathcal{M}_c}{\mathcal{M}_c(25 - 25M_\odot)} \right)^{5/6} \text{ Mpc} \quad (6.1)$$

where $\mathcal{M}_c(25 - 25M_\odot) = 21.76 M_\odot$ is the chirp mass of the most massive binary in the mass parameter space we explore. The idea is to obtain the same efficiency in each mass bin whether the binary is detectable at larger distance or not. Note this also differs with respect to [76] where the mass range goes until $50M_\odot$ which in turn changes the fiducial radius. With Eq (6.1) the position of the first peak is located around 250 Mpc.

A strong correlation exists between the luminosity distance, the eccentricity and the masses distributions. The sub-population of 10 - 10 M_\odot binaries which segregated close to the central object are the ones experiencing the vast majority of dynamical encounters and thus compose the first bulk of the luminosity distance distribution shown on Fig 6.6. The eccentricity distribution presents a bulk composed of binaries in quasi-circular orbits. Those binaries are located quite far away from the central object (at least 1 pc away) and did not experienced sufficient encounters that could make their orbit more eccentric. Another mode not displayed on Fig 6.6 is present at very high eccentricity values that correspond to a population of binaries which have gone through encounters or the Kozai-Lidov mechanism and have not circularised yet. This population is marginal because the timescale needed for a binary to circularise is shorter for larger eccentricities. We decide to retain the eccentricities below $e = 0.58$ and thus get rid of the very high eccentricity population. This complies with the lack of appropriate waveform models.

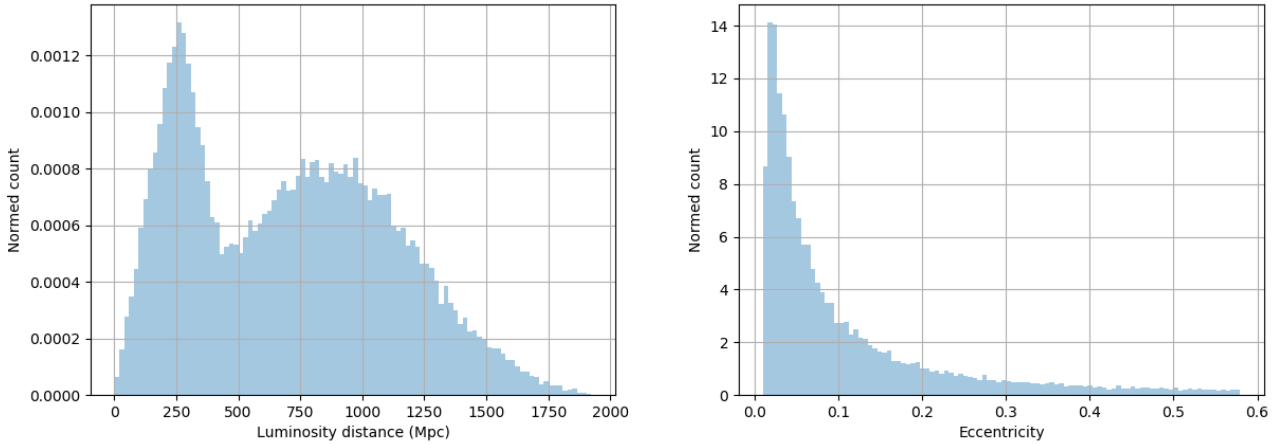


Figure 6.6: Luminosity distance (*left*) and eccentricity (*right*) distributions used to generate the injection set. The eccentricity distribution concerns binaries whose orbital frequency reached 20 Hz.

All remaining parameters describing the population of injected sources are randomly drawn from uniform distributions whose bounds are adapted to the parameter of interest. For instance, the phase at coalescence time is chosen between 0 and 2π rad.

6.3 Comparison study

In [76] cWB is presented as an interesting search for eccentric binary black holes. Along the following lines we propose to show what could be the contribution of Wavegraph. We conduct a comparison between three pipelines: cWB, cWB+WG using a circular graph and cWB with Wavegraph using an eccentric graph. The circular graph is computed with a template bank of quasi-circular **TaylorT4** waveforms and we use the **EccentricTD** waveform model for the eccentric graph. We focus the study on the inspiral part of the signal with a starting frequency $f_{low} = 20$ Hz in agreement with what we used for the graph. All the eccentric signals are injected in real O1 noise data.

6.3.1 Preliminary study

During first trials with eccentric signals with Wavegraph we decided to focus on eccentric waveform models with a low-eccentricity. Typically we take $e = 0.05$ in order to see if some first departures exist between the circular and eccentric graph models. The rest of all the injection and graph settings remain the same.

Results obtained using cWB with the standard cWB selection cuts

When addressing the detection of a new kind of signal with a detection pipeline, it is natural to test the default cuts of the search. As a first step we look at the result obtained by cWB with Wavegraph when using the standard cWB selection cuts. They are listed in Tab 6.3.1.

norm	frequency (Hz)	c_c	Qveto	Lveto	log(chi2)	chirp
> 2.5	$48 < f < 992$	> 0.7	> 0.3	< 5	< 0.2	> 1

Table 6.1: Standard cWB selection cuts for O1 analyses. The norm, Qvet, Lveto, chi2 and chirp selection cuts are defined in Sec 5.5.1 while the c_c cut is defined in Sec 4.2.2. A cut is performed on the frequency support of the isolated cluster which maps with the detection bucket of typical BBH systems. The mentioned inequality symbols concern the population of background and injected events that is conserved.

For this preliminary test we injected eccentric waveform models at Newtonian order with high order corrections waveform. Besides this point all analyses use the same settings. Performing a background estimation and a simulation using fake signals using cWB alone one get the results in Fig 6.7. Left subplot of Fig 6.7 show a clean background curve (no tails) which lead to a selection cut at $\text{FAR} = 10^{-8}$ Hz of $\rho = 6$. Right subplot is similar to Fig 5.9. The additional information on the injected SNR distribution is also shown. cWB misses a fraction of high SNR signal in the injected population. Nevertheless, cWB recovers 7.8% of the overall injections and the farthest recovered injection is located at 2.9 Gpc.

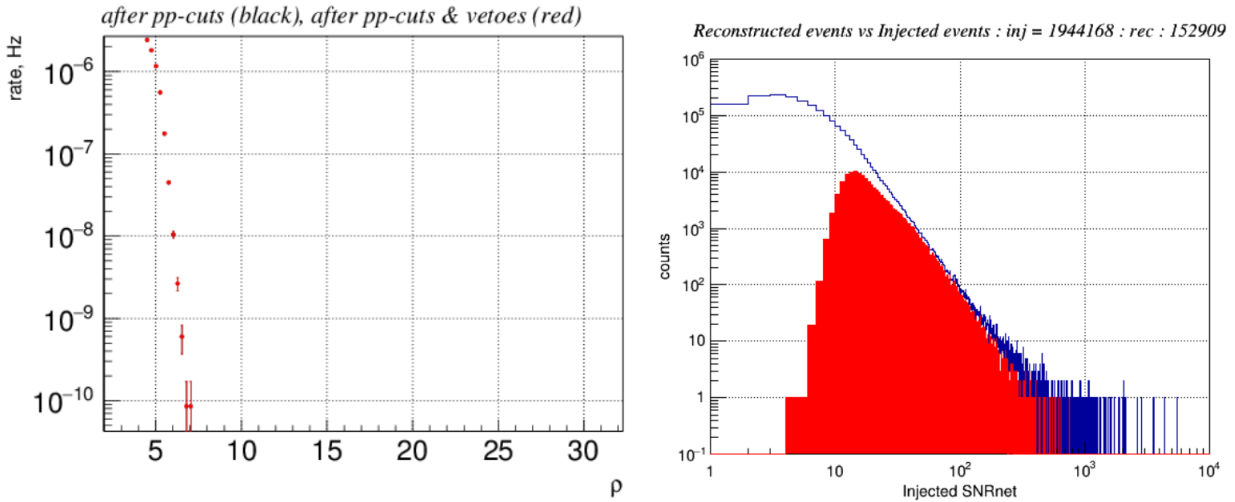


Figure 6.7: Background curve (*left*) and histogram of recovered events (*right*) obtained with cWB alone. The standard cWB selection cuts in Tab 6.3.1 have been applied.

In Fig 6.8 we show analogous results obtained with cWB and WG with a circular graph. The background curve is higher because it has a "bump" of noisy events at $\rho = 6 - 7$. The selection cut has to be increased to $\rho = 6.7$ because of this higher background. There is thus a population of noise events which degrades Wavegraph background in the circular graph case. What is problematic is that they sit in the bulk of the ρ distribution and cannot be simply removed by cWB standard cuts. Wavegraph also misses many injections at all injected SNR values. The most evident losses are at $\text{SNR} \sim 100$. This shrinks the overall detection efficiency of cWB with Wavegraph for a circular graph to $\sim 4.6\%$. Investigations revealed that the cause is the chi2 selection cut in Table 6.3.1. This constraint on the signal shape needs a good signal reconstruction to perform well so that the residual after the reconstructed signal subtraction is consistent with Gaussian noise. In the case where a signal is injected with a high SNR value the signal reconstruction error must reach the $1/\text{SNR}$ level in order

to leave a sufficiently small residual. This is not fulfilled for Wavegraph. One possibility is the discrepancy between the waveform model used to compute the graph (circular and low eccentricity) and the model used for the injection (full eccentricity range). We do not have a definitive explanation for this. Another possibility is that the time-frequency cluster in Wavegraph collects 80% of the signal energy: the remaining 20% may lead to a significant residual incompatible with the chi2 selection cut usage.

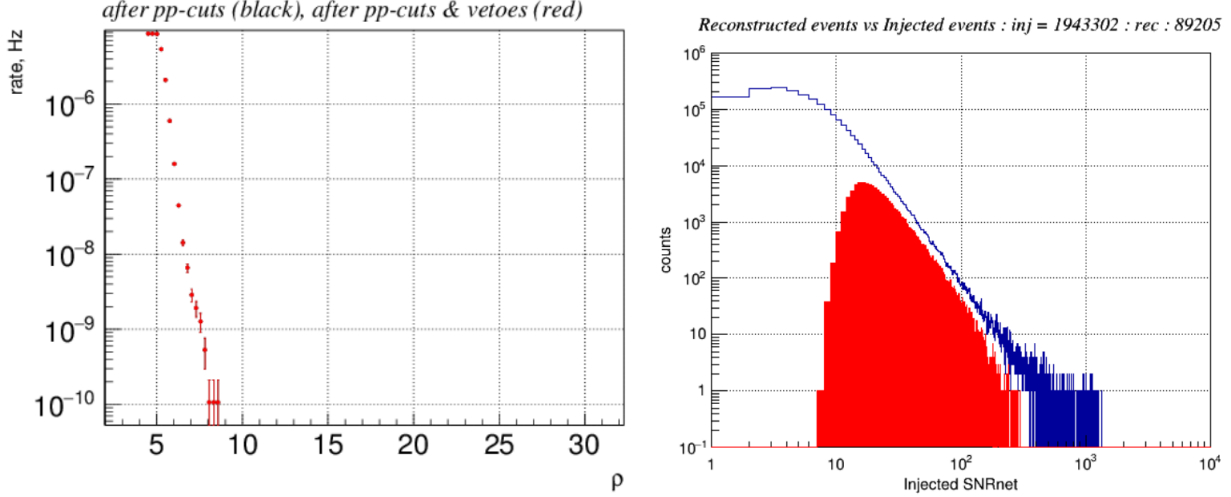


Figure 6.8: Background curve (*left*) and histogram of recovered events (*right*) obtained with cWB+WG with a circular graph. Only standard cWB selection cuts have been applied.

We will replace the chi2 selection cut with alternative tests such as the consistency test introduced in Sec 5.5.2 and the one described in the next section.

Results with the circular graph and introduction of a new TF complexity selection cut

Transient noises exhibit a diversity in their morphologies, but most of them are well localised in the time-frequency domain and thus need a smaller number of wavelets to be approximated compared to GW signals. The number of pixels above the noise level in the time-frequency cluster scales with the signal amplitude [153]. We propose a new selection cut based on the TF complexity as described by the number of pixels that compose the cluster (its size) and that adapts to the signal strength.

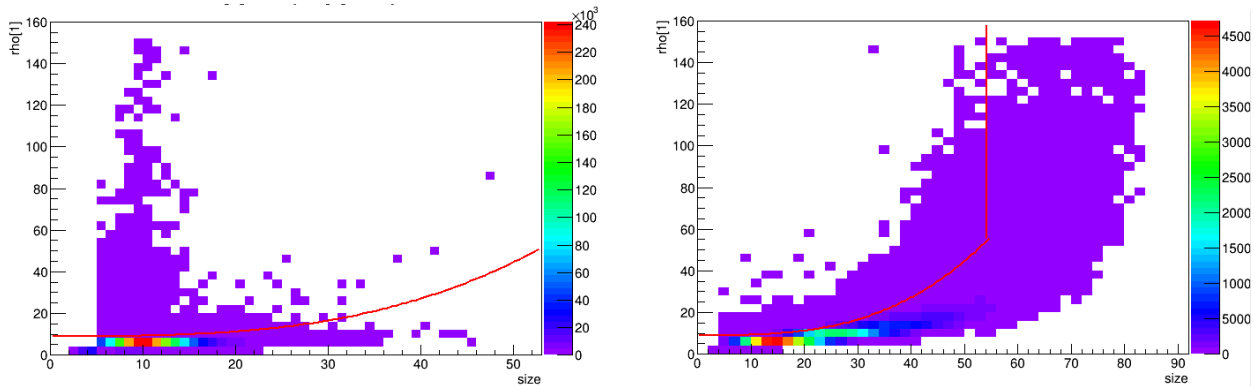


Figure 6.9: Joint distribution of ρ and TF cluster size for background triggers (*left*) and recovered GW events (*right*). Colorbar encodes the number of events in a given bin. Red curve corresponds to the "rho-size cut" curve common to both plots.

Fig 6.9 shows the distribution of the cluster size vs. the signal strength measured by the ρ statistic for background triggers and GW signals. The two distributions are very different and thus favours the application of a selection cut. The red curve in Fig 6.9 corresponds to the "rho-size cut", *i.e.* the boundary to reject low

complexity background triggers and retain high complexity GW signals. the equation of this curve is a cubic polynomial whose expression is $\rho(\text{size}) = 9 + 26(\text{size}/45)^3$. On the left plot one clearly sees that many loud transients can be removed when rejecting events above the red curve. In the right subplot GW events below the red curve are retained. The vertical red line ensure we do not discard too many loud injected signals.

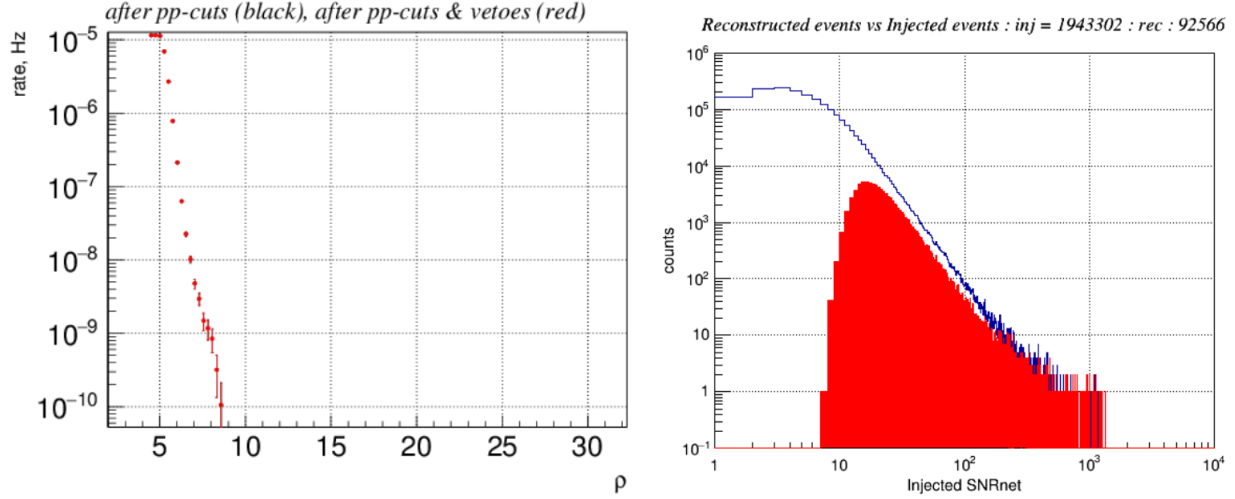


Figure 6.10: Background curve (*left*) and histogram of recovered events (*right*) obtained with cWB+WG with a circular graph. All standard GW selection cuts but the chi2 selection cut have been applied in addition to the consistency test.

The background curve shown on Fig 6.10 do not show an evident improvement: the ρ threshold remains at $\rho = 6.7$. Moreover the bump is still present as well. This is a clue that the combination of the consistency test with the rho-size selection cut does not perform as well as the cWB chi2 cut. The most important difference is that we recover the population of loud events which used to be discarded by the too stringent cut made by the chi2 cut: we recovered $\sim 4\%$ of events. The overall detection efficiency reaches 4.7% and is still inferior to the one of GW alone.

Results with the low eccentric graph

We repeat this analysis with the low eccentricity graph computed with a low eccentricity of $e = 0.05$. We *a priori* do not anticipate any big differences with the circular graph. For this reason we use the very same analytic expression for the rho-size cut. The results are shown on Fig 6.11.

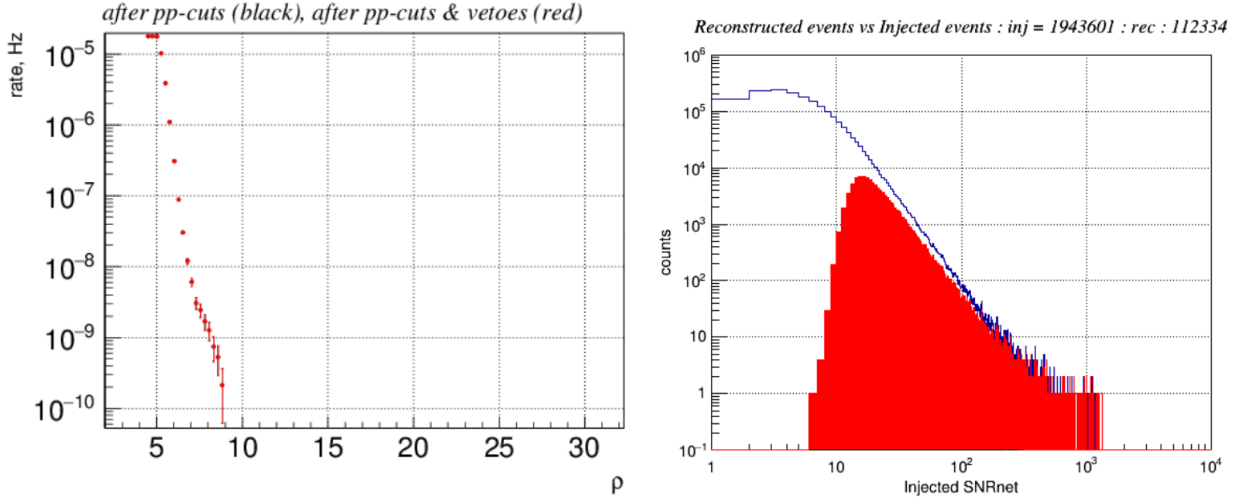


Figure 6.11: Background curve (*left*) and histogram of recovered events (*right*) obtained with cWB+WG with a low eccentricity graph ($e = 0.05$). All standard cWB selection cuts but the chi2 selection cut have been applied in addition to the consistency test.

The background curve is similar to the circular the circular graph (same bump) except a slightly higher background rate which increases the cut to $\rho = 6.9$ (see Fig 6.11). This increase of the background may be due to the slightly larger graph (382 nodes) for the circular graph compared to the low eccentric graph (276 nodes). The low eccentricity graph is able to recover many more injections: +21% relative improvement with respect to the circular graph due to the better match between the model used to compute the graph and the injected waveform. The farthest recovered injection is now at 2.3 Gpc. The still important gap in terms of signal recovery with respect to cWB can be explained by the fact we used a restricted eccentricity graph.

6.3.2 Results with the "fully eccentric" graph

We turn our attention to the graph presented in Fig 6.4 that covers the widest possible eccentricity range with the available waveform models. The circular graph is presented in Fig 5.4. The injected population of sources into O1 real noise data is described previously. The cWB version used in what follows has been updated to include recent developments introduced for the O2 run.

Figure 6.12 shows a re-run of the analysis with cWB alone, with a reference and revised software version. Results obtained with Wavegraph will be compared to this result. The parameter ranges for the injection set, *i.e.* individual masses, luminosity distance and eccentricity remain the same.

Results with cWB and Wavegraph obtained with the standard selection cuts

Thanks to an improved reconstruction scheme leading to a better chi2 rejection efficiency, cWB background curve falls faster than in the preliminary study resulting in a threshold $\rho = 6$ at $\text{FAR} = 10^{-8}$ Hz. However the chi2 cut still eliminates loud injections. The overall efficiency is 18%.

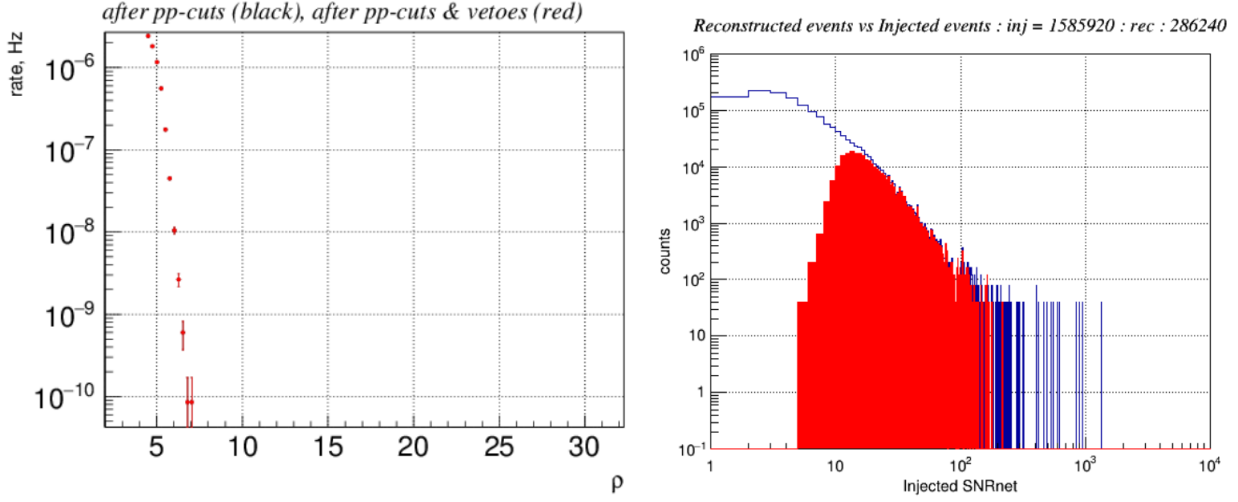


Figure 6.12: Background curve (*left*) and histogram of recovered events (*right*) obtained with cWB alone with the standard selection cuts. Note both cWB version and the injection set have changed with respect to the preliminary study.

The same analyses are repeated with Wavegraph using the eccentric graph with $0.05 < e < 0.58$. For the sake of completeness we present in Fig 6.13 the results obtained with the cWB standard cuts.

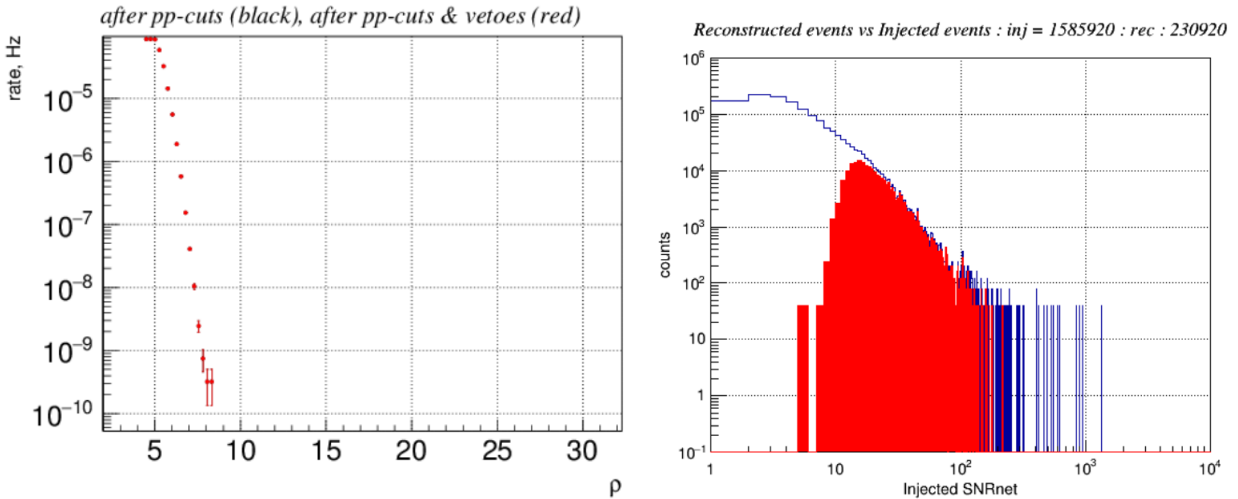


Figure 6.13: Background curve (*left*) and histogram of recovered events (*right*) obtained with cWB+WG with the full eccentric graph using the standard cWB selection cuts. Note that both cWB version and the injection set have changed with respect to the preliminary study.

The background curve is still slightly higher for cWB+WG but the bump is not present anymore. The threshold is $\rho = 7.3$ at $\text{FAR} = 10^{-8}$ Hz which translates the fact we are using a larger graph. for the simulation, the presence of the chi2 selection cut prevents us from retaining injections at high SNR. Comparing with Fig 6.11 we recover 120,000 more injections in spite of the effect of the chi2 selection cut. We should design a more specific cut for Wavegraph that can replace the chi2 selection cut. We suppose this will cure the loss of high SNR events.

Investigations of combined non-linear selection cuts

During the preliminary study, we experimented selection cuts that combined different event parameters (ρ and cluster size). In this section we propose to elaborate a new set of selection cuts by combining parameters and features, and optimizing the combinations to get better performances. We follow an heuristic and procedural approach. We tested several non-linear combinations of cWB parameters. Such an approach is inspired from machine learning where artificial and non-physical non-linearities are introduced among the features of interest.

Concretely, we looked at the background and recovered signal distributions for a common non-linear cut. Such a cut is invented so as to split the two distributions. Following this procedure it becomes possible to separate features. Selection cuts listed in Tab 6.3.2 achieve a quite satisfactory trade off: minimizing spurious events and maximizing recovered events.

Selection cuts	Thresholds
c_c	> 0.7
T/ρ^2	< 0.3
$Qveto[0] \times chirp[1]$	$[1, 316]$
$Lveto[1] \times chirp[1]$	$[-45, 5]^c$
$chirp[1] \times Qveto[0]^5$	$< 2.5 \times 10^4$
$Qveto[0] + Qveto[1]$	$[3, 25]$
$Lveto[0] \times chirp[1]$	$[18.2, 65.6]$
$Lveto[0] \times Lveto[1]$	< 3684

Table 6.2: Wavegraph non-linear selection cuts. The mentioned inequality symbols concern the population of background and injected events that is conserved. The set E^c designates the complement of E .

Obviously selection cuts in Tab 6.3.2 do not have any physical meaning (except the c_c and the CT cuts) but we claim they serve detection efficiency purposes. On Fig 6.14 are displayed the results when applying the selection cuts enumerated in Tab 6.3.2. Note the rho-size cut have been dropped since it does not perform well with the new adopted graph.

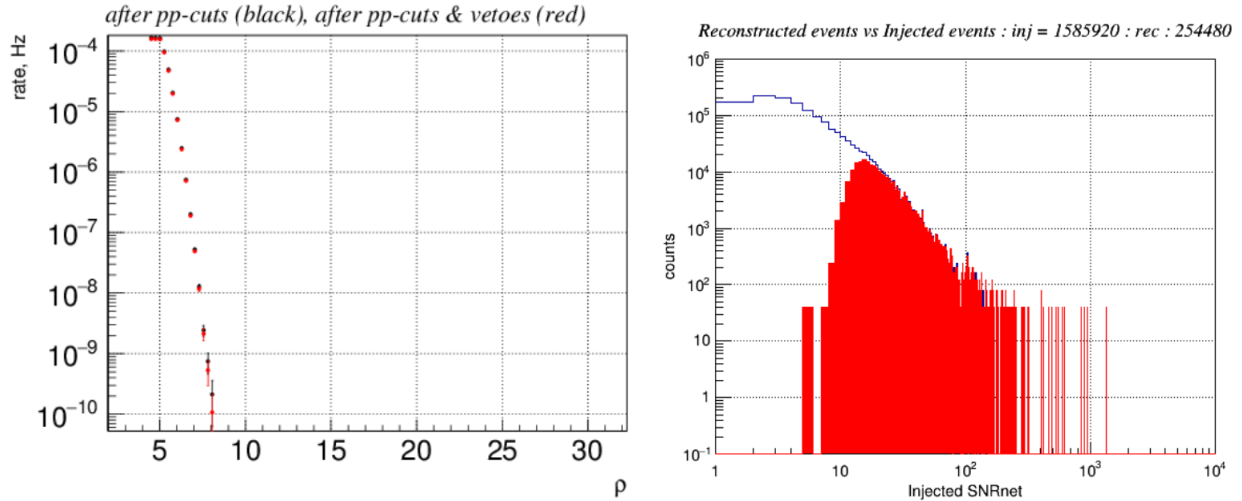


Figure 6.14: Background curve (*left*) and histogram of recovered events (*right*) obtained with cWB+WG with the wide eccentricity graph. Only selection cuts figuring in Tab 6.3.2 have been applied. Note both cWB version and the injection set have changed with respect to the preliminary study.

Using the non-linear cuts we arrived to a clean background curve where the "bump" is absent. At $FAR = 10^{-8}$ Hz, the threshold is $\rho = 7.3$. This is the best threshold we could find with the other trials to further reduce the background level. With this threshold, the number of recovered injections has increased by 10% and the overall detection efficiency reaches 16%. This shows there is a benefit in using supplementary cuts that will remove more background. Loud events are also better recovered than with the eccentric graph and standard cWB cuts.

One may ask whether the fact of procedurally finding the best of selection cuts together with their associated threshold values can be considered as over-fitting, *i.e.* the fact of designing a search so that it is too sensitive to the used data. In this context, sensitive is meant as too close from the simulated data. With our approach we claim the designed cuts do not over-fit the data. When a machine-learning algorithm is said to over-fit, it is because the model (let us say a neural network) complexity is so large that it fits noise features. In other words, the trained model does not perform as well when ran on another training set. The neural network is evaluated through its efficiency on the test set. However the choice of the non-linear cuts for Wavegraph is the result of a simultaneous compromise: there are two figures-of-merit. One is the rejection of noisy features while

the second concerns only the GW signal recovery. It is worth mentioning that the same set of selection cuts shown in Tab 6.3.2 have been used at the occasion of a new Monte-Carlo simulation with another injection set and another background study. This proves the non-linear cuts are not specific to the simulated data set we produced at the first trial.

Of course this approach needs to be automated. A possible algorithm to do so would be to specify a set of non-linear cuts and then run an optimisation algorithm that would determine the optimal thresholds for each proposed non-linear cut.

Other figures of merit

We finish the presentation of the results obtained by cWB+WG by a series of diagnostic figures that would help determining the reason of the lack in recovery. Other trends specific to Wavegraph will be verified that have already been noticed in chapter 5 like the c_c distribution.

Fig 6.15 shows that Wavegraph brings few percent level improvements in the sensitive distance in low-mass range. Mass bins below total mass $40M_\odot$ show an improvement. For three of them located at $(q, M) = (1.0, 35M_\odot)$, $(1.4, 30M_\odot)$ and $(1.8, 35M_\odot)$, the relative improvement reaches at least 2% with a 1σ significance. In the eBBH case, there is a clear dependency on the total mass and almost no dependency on the mass ratio. A possible explanation is that lighter binaries spend more time in the time-frequency domain and their specific TF trends is better caught by the graph. Note also those binaries are located closer (up to ~ 1.2 Gpc) due to the injection scaling.

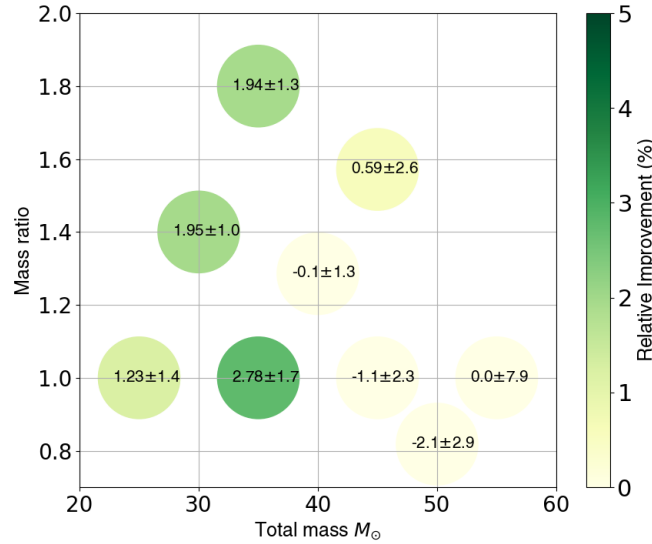


Figure 6.15: Relative improvement in sensitive distance using cWB+WG together with the wide eccentricity graph at $\text{FAR}=10^{-8}$ Hz.

Fig 6.16 shows an histogram of the correlation network coefficient (defined in chapter 4) for cWB alone and cWB+WG for the wide eccentricity graph. Clearly the results obtained in the Gaussian noise case (see Fig 5.11) are not reproduced in the context of eBBH searches. It can be explained by two contributing factors. First, the eccentric graph have more nodes with higher number of ancestors. It means the graph is more interconnected than the circular graph. When extracting the maximum incoherent energy path in the graph, the dynamic programming algorithm evaluates what pixels to add in order to collect the best amount of energy. In the ideal case where no noise is present, the maximum energy path will go through the pixels along the chirp signal in the TF domain (as the energy is only concentrated in the signal). In the real noise case, noise fluctuations or transient noises create spurious excesses around the GW signal. It happens pixels extracted by WG collect those noise artifacts. The dynamic programming algorithm can hence select those latter pixels because they carry more energy than the GW signal. As a consequence, the extracted path deviates from the one that could have been extracted in noiseless conditions. It means the path selected by the dynamic programming algorithm is susceptible to deviate from a physical time-frequency pattern because of the presence of a noise transient.

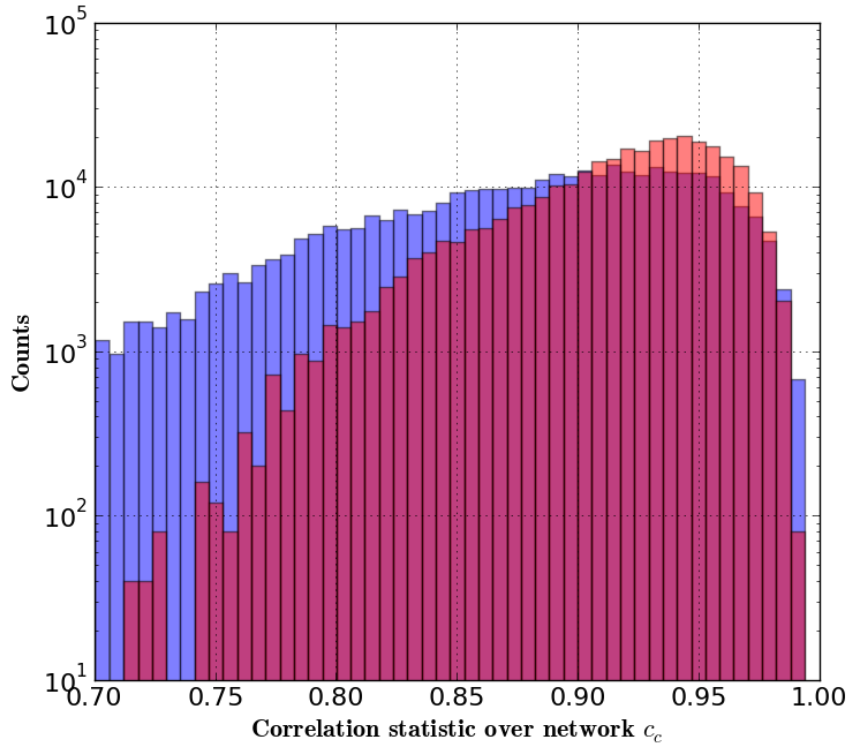


Figure 6.16: Network correlation coefficient distribution for cWB alone (*light red*) and cWB+WG (*light blue*).

A second explanation comes from the ordering rule according to which pixels selected by the UMP are sorted. The time-only ordering rule we applied is illustrated in Fig 6.17 with an example eccentric waveform template. The linking between pixels does not follow the frequency evolution because of the various harmonics. These two arguments combined explain the internal structure of the eccentric graph. The correlation of each pixel is not as high as the one shown for the circular graph.

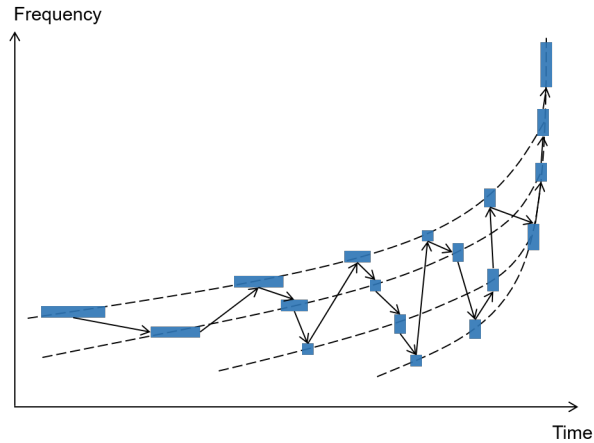


Figure 6.17: Time ordering

In order to compare the quality of the reconstructed GW signal we introduce the *overlap factor* denoted \mathcal{O} and defined as

$$\mathcal{O}(h_{inj}, h_{rec}) = \frac{\langle h_{inj} | h_{rec} \rangle}{\sqrt{\langle h_{inj} | h_{inj} \rangle \langle h_{rec} | h_{rec} \rangle}} \quad (6.2)$$

where $\langle .|. \rangle$ is the scalar product defined in Eq (4.21). The overlap factor estimates the match between the injected signal h_{inj} and the recovered signal h_{rec} . The recovered signal is the averaged reconstructed signal from each detector. By definition the overlap factor can take values between 0 and 1. It quantifies the reconstruction efficiency of a search. In Fig 6.18 we show the overlap factor in function of the injected SNR. As expected the overlap factor goes to 1 when the injected SNR is high. CWB and cWB have a comparable reconstruction efficiency: the overlap factor sharply increases until reaching a plateau. The overlap factor is above 0.9 when the injected SNR is above 20 and never goes below 0.7. CWB+WG shows a variable overlap factor (large spread) due to the low statistic of recovered events but also because of the bad pixel selection evidenced in Fig 6.16.

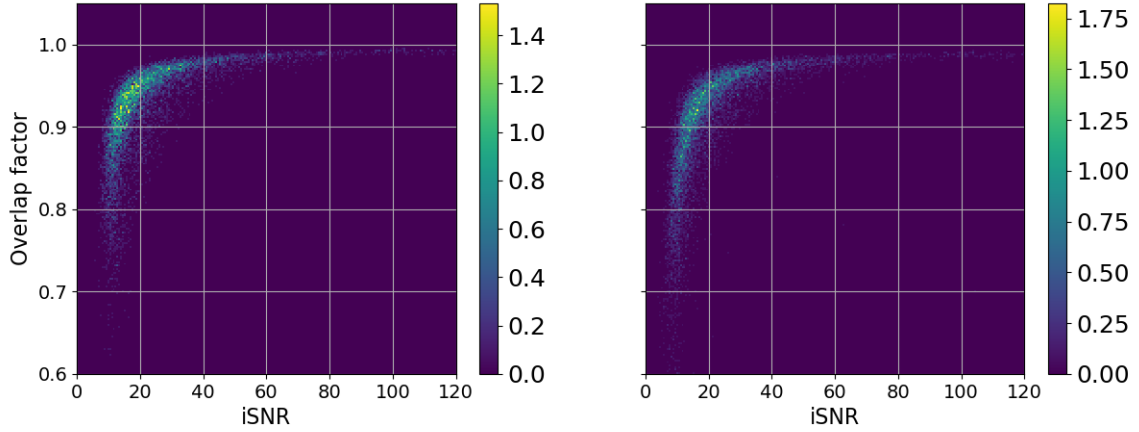


Figure 6.18: 2D histogram of the overlap factor and the injected SNR for cWB (*left*) and cWB+WG with the wide eccentricity graph (*right*). The bin values have been normed so as to sum to one.

Chapter 7

Conclusion

Contents

7.1 Lesson learned and perspectives with Wavegraph	93
7.1.1 Lessons learned and possible improvements	93
7.1.2 Extensions and future prospects	94
7.2 The futures of gravitational wave experiments	95

The first chapters of this thesis give a contextual review concerning gravitational waves: their prediction by general relativity, their astrophysical sources, the instruments (laser interferometers) that have made their first direct detection. We also review the main data analysis approaches used in the LIGO and VIRGO collaborations to detect them in the observational data.

We conclude this initial review by underlining the limits of current modeled and unmodeled gravitational wave transient searches. For compact binary mergers, we noted that the extreme regions of the parameter space (e.g., large eccentricities) remains fairly unexplored by dedicated and sensitive searches.

7.1 Lesson learned and perspectives with Wavegraph

The second part of the thesis presents the unmodeled search pipeline called “coherent WaveBurst”. In an attempt to mitigate the limitations described above we introduce Wavegraph, a new and original time-frequency clustering scheme for cWB. Wavegraph leverages the astrophysical knowledge extracted from the phase evolution of the targeted class of gravitational-wave waveforms.

The performances of Wavegraph is evaluated in different contexts. In chapter 5 we show how Wavegraph performs in Gaussian noise and in real instrumental noise. In Gaussian noise, we show that Wavegraph improves by 7 – 8% over cWB alone the relative distance reached for binary black hole mergers. Assuming a uniform source distribution, this leads to an increase of 20 – 25% in the detection rate for those sources. Wavegraph also allows a better reconstruction of the detected signals.

In real instrumental noise (O1 LIGO science run) we show that Wavegraph is quite sensitive to transient noise. The noise rejection capabilities of Wavegraph and the consistency test introduced in chapter 5 are not sufficient. Wavegraph leads to a small or zero improvement for the searches of circular and eccentric binary black hole searches in real instrumental noise.

7.1.1 Lessons learned and possible improvements

This section lists lessons learned and possible improvements of the Wavegraph algorithm:

- **Reduce the graph connectivity** – The time-frequency pixels from all waveform templates are gathered and merged together in the graph. This leads to many interconnections between the graph nodes. Energy excesses arising from noise transients may divert the path with maximal incoherent energy in the graph from a “physical route”, compatible with one of the considered waveform templates, but rather build up a

non-physical path by stitching sub-clusters of pixels from different templates that happen to be connected together. This is particularly true for the eccentric binary graphs, where the connectivity is much larger than in the circular case. Those possibly low-correlation pixels introduce errors in the reconstructed signal and leads to an higher noise background. Reducing the graph connectivity by increasing again the signal representation sparsity may help. Indeed approximating the signal with fewer pixels would result in reduced probabilities of forming ancestors.

- **Use better/more physical pixel ordering** – Nodes in the eccentric graph are sorted with a “increasing in time” only ordering rule (no ordering in frequency, see Fig 6.17) that was selected as a simple solution because the waveform phase does not have a monotonic evolution. It is natural to think that ordering the pixels from harmonic modes separately as shown in Fig. 7.1 would do a better job. Such ordering could be implemented using the analytical expressions for the GW modes at fixed n , see Eqs. (19)-(20) of [154]. Each mode is a monotonic chirp that can be processed with the “increasing in time and in frequency” ordering rule used in the circular/quadrupolar case. Once all pixels from every modes have been selected, one would merge them in a single time-frequency pattern. The rest of the Wavegraph would remain the same.
- **Adapt the range of time-frequency resolutions to the waveform variability** – For simplicity, we used a flat range of time-frequency resolutions (five levels, from 3 to 7) to decompose the GW signal waveforms. This setting has been indifferently applied in the circular or eccentric binary cases. However we observe that resolution levels are differently populated depending on the eccentricity. For low eccentricity waveforms the pixel distribution is analogue to the one shown in Fig 5.4, whereas for high eccentricities low levels are more occupied as a result of the the phase/amplitude waveform variability. As a consequence the range of time-frequency resolutions could be adapted to the range of eccentricity.
- **Use polarisation selection cuts** – In [76], alongwith the chirp selection cut presented earlier, the authors also consider a cut that selects elliptically polarised signals. Eq. (2.20) includes an additional dependence to the orbital plane inclination through the $\sin^2 \iota \Psi(e, \phi)$ term. In the quasi-circular orbit case the function $\Psi(e, \phi)$ vanishes. This means that for an optimally oriented binary ($\iota = 0$) the polarisation is circular. In the more general case where the eccentricity is not zero the polarization becomes elliptical. So cutting on the observed polarisation as estimated by cWB can increase our confidence in detecting an eccentric binary black hole merger.
- **Machine learning for transient noise rejection** – We designed a set of non-linear cuts for Wavegraph to preserve as much as possible the population of recovered injections while rejecting transient noises. Its application in the case of eBBH searches (see chapter 6) gave us a clue on how convenient the introduction of non-physical non-linearities could benefit to the purposes of the detection. The procedural approach we followed so far can be automated and extended by designing a machine learning algorithm [155]. Indeed this class of algorithms also introduce artificial non-linearities between each layer of neurons to better perform a feature distinction. Designing a neural network dedicated to eccentric BBH searches would take advantage of the well structured shape of the time-frequency cluster. This would help a classifier in the rejection of noise transient events.

Beyond the algorithmic improvements listed above, a major advance is expected from complete inspiral, merger and ringdown eccentric waveform, that are not available yet, as a large fraction of the SNR is expected to come from the merger part of the waveform (currently missing in the inspiral-only waveform models we used here).

7.1.2 Extensions and future prospects

The Wavegraph method is general and could be applied to a wider class of signals than the sole binary mergers considered in this thesis. Figs. 7.2 and 7.3 present two examples. Fig. 7.2 shows the time-frequency pattern associated to the GW waveform model of a *standing accretion shock instability* (SASI) driven supernova obtained from numerical relativity, hydrodynamic core-collapse simulations [156]. The Wavegraph parameters such as the range of the resolution levels should be tuned according to the signal. Here we used the standard resolution range applied for compact binaries. Fig. 7.3 shows the time-frequency pattern of an accretion disk instability waveform [157]. Clearly the signal frequency ramps down from 209 to 110 Hz over 10 sec approximately. We used resolution levels ranging from 7 to 10 that extends to higher frequency resolution/longer duration wavelets that better match with the large signal spread in time and slow frequency variation.

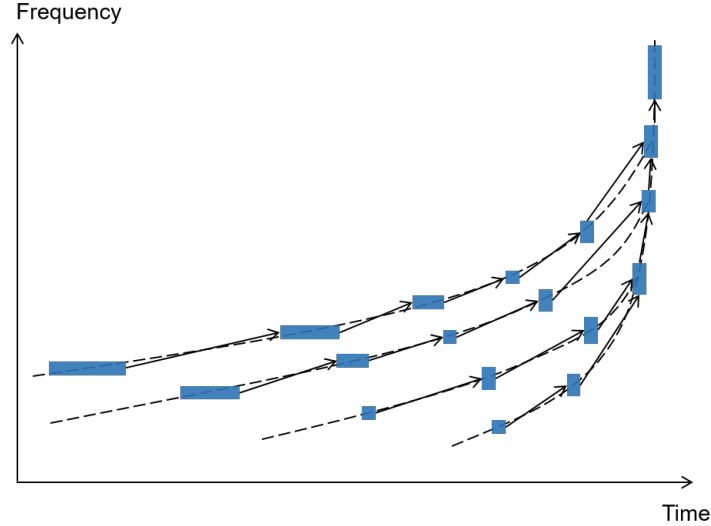


Figure 7.1: Ordering harmonic modes separately

7.2 The futures of gravitational wave experiments

The detections made during the first runs of second generation detectors lead us to the frontier of strong gravitational field physics, high energy astrophysics and multi-messenger astronomy. While we soon expect more discoveries with those instruments, this science will be further extended by a network of third generation instruments and the space mission LISA.

By using longer arms possibly built underground, a larger laser power and advanced technologies such as squeezed light, or cryogenic optics, the European Einstein Telescope [158] and the US Cosmic Explorer [159] aim at a factor of ~ 10 improvement in strain sensitivity (i.e., few $10^{-24} \text{ Hz}^{-1/2}$ at 100 Hz) and a wider observational frequency window ($\sim 1 \text{ Hz} - 10 \text{ kHz}$). Such sensitivity will allow to detect a BBH of total mass above $10M_{\odot}$ up to large cosmological distances.

The Laser Interferometry Space Antenna mission [160] is a constellation of three satellites that form a triangle with free falling test masses with 2.5 million km arms. The tiny relative distance variation between pairs of test masses will be measured using interferometry, thus allowing the observation of gravitational waves in the frequency range between 0.1 mHz and 100 mHz. LISA will observe various astrophysical sources, especially supermassive black holes upto large redshifts. Thanks to the recent success of the technology demonstrator LISA PATHFINDER [161, 162], LISA is on-track for a launch currently planned around 2034.

Both those future observatories are expected to detect a large and diverse population of sources, some of which could be unknown. Thanks to their enhanced sensitivity at low frequencies the future ground-based detectors may be able to observe the inspiral part of highly eccentric binary merger [82] (Typically a stellar mass BH binaries with $e \sim 0.9$ would reach the last stable orbit around 10 Hz). One of the important target for LISA are extreme-mass ratio inspirals formed by a stellar-mass object orbiting a supermassive black hole. The combined effects of large mass ratio and eccentricity leads to strong relativistic effects resulting in a complex orbital evolution and thus a complex waveform phasing which is currently not completely modeled. Those are cases where the ideas behind Wavegraph could be useful.

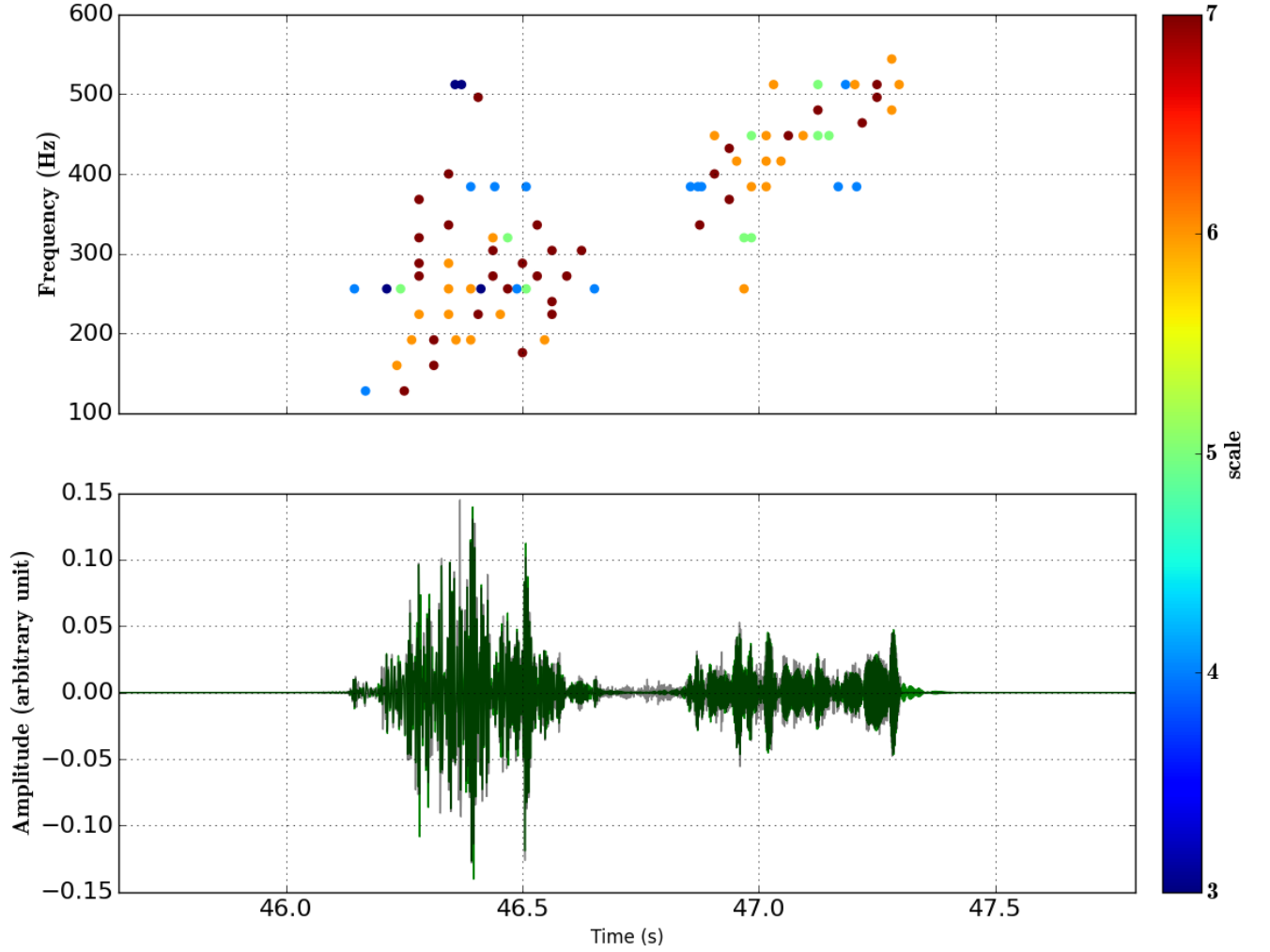


Figure 7.2: Time-frequency cluster obtained with the updating matching pursuit algorithm applied to the GW waveform model for a simulated SASI driven supernova [156]. The progenitor is a $15M_{\odot}$ massive star located at 10 kpc. The approximation error of the UMP is fixed to 20% and the decomposition results in 128 collected pixels. The bottom panel shows the associated approximation in dark green superimposed to the original waveform in grey.

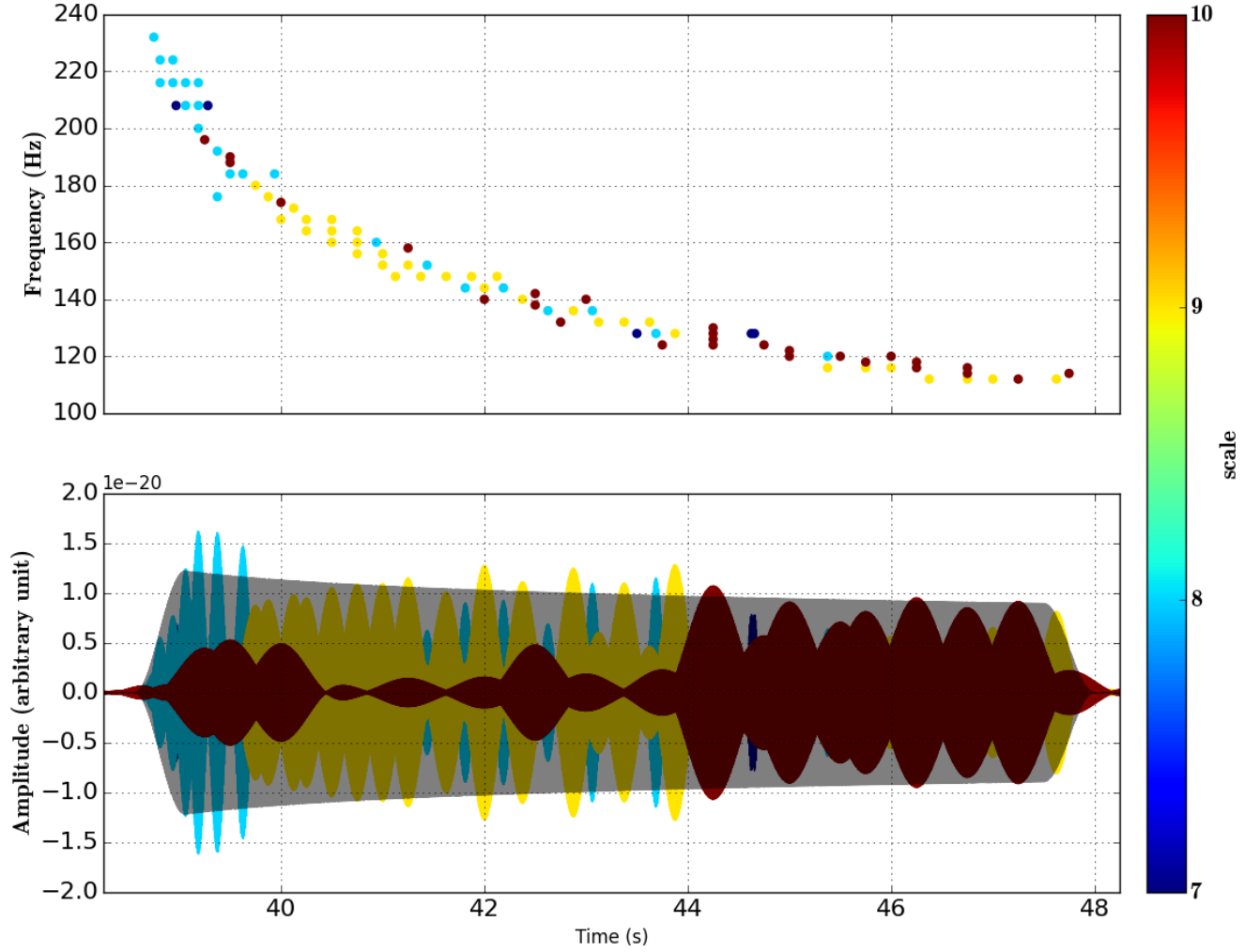


Figure 7.3: Time-frequency cluster obtained with the updating matching pursuit algorithm applied to the GW waveform model associated to an accretion disk instability which develops in a newly formed $10M_{\odot}$ black hole with spin $a = 0.95$ surrounded by a $1.5M_{\odot}$ accretion disk [157]. The bottom plot shows the extracted wavelets (time domain) by WG and how they describe the signal (light black). The approximation error of the UMP is fixed to 10% and the decomposition results in 89 time-frequency pixels.

Appendix

Appendix A: Choice of the approximation error level in the matching pursuit algorithm

It might seem surprising such a high error δ is sufficient in recovering and/or reconstructing a signal in noisy conditions. In order to demonstrate it is still a safe threshold, several clusters of pixels have been computed scanning several values for $1 - \delta = 60\%, 70\%, 80\%, 90\%$ for a given spinning CBC signal. Then the very same signal is injected into Gaussian noise and analysed by cWB with Wavegraph. Unless it is not yet clear for the reader how the search is performed it is claimed that the results shown in Table (7.2) are representative of the overall behaviour of the algorithm.

$1 - \delta$ (%)	Number of pixels in the cluster	Cluster duration (s)	recovered SNR
60	7	0.33	16.4
70	16	0.40	33.5
80	29	0.65	38.3
90	56	1.31	39.3

Table 7.1: Comparison of the signal recovery by cWB with Wavegraph of a spinning CBC signal with ($m_1 = 32M_\odot, m_2 = 26M_\odot, \chi_1 = 0.90, \chi_2 = -0.11$) buried in Gaussian noise. Even in non signal-free conditions, taking $\delta = 80\%$ is a good compromise between sparsity and SNR reconstruction.

Table (7.2) contains quantitative results regarding a single injection recovered thanks to 4 different clusters with varying approximation error values. Unsurprisingly the number of pixels along with the time duration of the signal attached to the cluster both increase as $1 - \delta$ increases. Also collecting more pixels means collecting more SNR as pixels do carry energy. However values show what has already been highlighted in Fig (5.3): it exists a plateau in reconstructed energy where a lot of iterations are needed to reach a high reconstruction level hence impacting sparsity. Regarding the last two rows, twice more pixels are needed to go from $1 - \delta = 80\%$ to 90% while the improvement in recovered SNR is only of $\sim 2\%$. So staying with $1 - \delta = 80\%$ still is a good compromise.

Appendix B: stationary phase approximation derivation

In this section we detail the derivation of Eq (5.3) following computation of [139]. For this we start from Eq (5.2) which can be rewritten as:

$$\rho_0^2 = \left| \int df \tilde{A}(f) e^{\Phi(f)} \right|^2 \quad (7.1)$$

where the integrand amplitude $\tilde{A}(f)$ and phase $\Phi(f)$ are defined as:

$$\tilde{A}(f) = (2\pi)^{1/4} \sqrt{\sigma_0} A(f) / S_n(f) \quad (7.2)$$

$$\Phi(f) = -\pi^2 \sigma_0^2 (f - f_0)^2 + i [\Psi(f) + 2\pi f t_0] \quad (7.3)$$

We recall that $S_n(f)$ is the one-sided power spectral density and that $A(f)$ and $\Psi(f)$ are the signal amplitude and phase respectively. The first term in the signal phase comes from the expression of a sine-gaussian wavelet in the frequency domain given by Eq (5.1). The integral appearing in Eq (7.1) can be estimated using the *stationary phase oscillation* (SPA). Indeed, one can expand the integrand phase as:

$$\Psi(f) \approx \Psi(f_0) + \alpha(f - f_0) + \beta(f - f_0)^2 \quad (7.4)$$

Replacing Eq (7.4) in Eq (7.3) and defining $\zeta = f - f_0$, the integrand phase becomes:

$$\Phi(f) = (i\beta - \pi^2\sigma_0^2)\zeta^2 + i[\Psi(f_0) + \alpha]\zeta + i2\pi ft_0 \quad (7.5)$$

when expanding $\Phi(f)$ around a central frequency f_0 and assuming $|\zeta| \ll 1$. Again replacing Eq (7.5) in Eq (7.1) the amplitude energy expression becomes:

$$\rho_0^2 = \left| \int df \left[\frac{(2\pi)^{1/4} \sqrt{\sigma_0} A(f)}{S_n(f)} \right] e^{(i\beta - \pi^2\sigma_0^2)\zeta^2 + i[2\pi t_0 + \alpha]\zeta} \right|^2 \quad (7.6)$$

Note we ignored the constant phase term as it does not affect the final result. Assuming slow variations for $A(f)$ in an interval centered on f_0 , Eq (7.6) reduces to a Gaussian integral of the form:

$$\forall \xi, \alpha \in \mathbb{C}, \quad \int_{-\infty}^{+\infty} dx e^{\frac{1}{2}i\alpha x^2} e^{i\xi x} = \sqrt{\frac{2\pi i}{\alpha}} e^{\frac{-i\xi^2}{2\alpha}} \quad (7.7)$$

As a consequence, Eq (7.6) reduces to

$$\rho_0^2 = \sqrt{2\pi}\sigma_0 \left| \frac{A(f_0)}{S_n(f_0)} \right|^2 \left| \int df e^{(i\beta - \pi^2\sigma_0^2)\zeta^2 + i[2\pi t_0 + \alpha]\zeta} \right|^2 = \sqrt{2\pi}\sigma_0 \left| \frac{A(f_0)}{S_n(f_0)} \right|^2 \frac{\pi}{|\pi^2\sigma_0^2 - i\beta|} e^{\operatorname{Re} \left[\frac{(\alpha + 2\pi t_0)^2}{4(\pi^2\sigma_0^2 - i\beta)} \right]} \quad (7.8)$$

One realises that the argument in the exponential vanishes when $t_0 = \tau(f_0) = -\alpha/(2\pi)$. Introducing this quantity, yields Eq (5.3).

Bibliography

- [1] P. Bacon, V. Gayathri, E. Chassande-Mottin, A. Pai, F. Salemi, and G. Vedovato, “Driving unmodeled gravitational-wave transient searches using astrophysical information,” *Physical Review D*, vol. 98, p. 024028, July 2018.
- [2] V. Gayathri, P. Bacon, E. Chassande-Mottin, A. Pai, F. Salemi, and G. Vedovato, “Applying wavegraph in real noise.” in preparation, 2018.
- [3] Q. Bammey, P. Bacon, E. Chassande-Mottin, A. Fraysse, and S. Jaffard, “Sparse Time-Frequency Representation of Gravitational-Wave Signals in Unions of Wilson Bases,” *Proceeding of Eusipco conference, Rome*, 2018.
- [4] A. Einstein, “Zur elektrodynamik bewegter korper,” *Annalen der Physik*, vol. 322, <https://onlinelibrary.wiley.com/doi/pdf/10.1002/andp.19053221004>, no. 10, pp. 891–921, 1905.
- [5] A. Einstein, “Die formale grundlage der relativitätstheorie,” *Sitzungsberichte . K. Preuss. Akad. Wiss.*, pp. 1066–1077, 1914.
- [6] A. Einstein, “Näherungsweise integration der feldgleichungen der gravitation,” *Sitzungsberichte . K. Preuss. Akad. Wiss.*, p. 688, 1916.
- [7] J. A. Wheeler and K. W. Ford, “Geons, Black Holes, and Quantum Foam: A Life in Physics,” 1998.
- [8] J. D. Jackson and L. B. Okun, “Historical roots of gauge invariance,” *Rev. Mod. Phys.*, vol. 73, pp. 663–680, Sep 2001.
- [9] M. Maggiore, *Gravitational waves*. Oxford: Oxford Univ. Press, 2008.
- [10] E.ourgoulhon, *Relativité générale*. 2014.
- [11] D. Kennefick, *Traveling at the Speed of Thought: Einstein and the Quest for Gravitational Waves*. Princeton University Press, 2007.
- [12] B. P. Abbott *et al.*, “Observation of gravitational waves from a binary black hole merger,” *Phys. Rev. Lett.*, vol. 116, p. 061102, Feb 2016.
- [13] J. Veitch *et al.*, “Parameter estimation for compact binaries with ground-based gravitational-wave observations using the LALInference software library,” *Physical Review D*, vol. 91, 1409.7215, p. 042003, Feb. 2015.
- [14] B. P. Abbott *et al.*, “Properties of the Binary Black Hole Merger GW150914,” *Physical Review Letters*, vol. 116, 1602.03840, p. 241102, June 2016.
- [15] B. P. Abbott *et al.*, “Tests of General Relativity with GW150914,” *Physical Review Letters*, vol. 116, 1602.03841, p. 221101, June 2016.
- [16] K. Belczynski, V. Kalogera, F. A. Rasio, R. E. Taam, A. Zezas, T. Bulik, T. J. Maccarone, and N. Ivanova, “Compact Object Modeling with the StarTrack Population Synthesis Code,” *Astrophysical Journal*, vol. 174, astro-ph/0511811, pp. 223–260, Jan. 2008.
- [17] J. Abadie *et al.*, “Predictions for the rates of compact binary coalescences observable by ground-based gravitational-wave detectors,” *Classical and Quantum Gravity*, vol. 27, 1003.2480, p. 173001, Sept. 2010.
- [18] E. E. Salpeter, “The Luminosity Function and Stellar Evolution.,” *Astrophysical Journal*, vol. 121, p. 161, Jan. 1955.

- [19] B. P. Abbott *et al.*, “GW151226: Observation of Gravitational Waves from a 22-Solar-Mass Binary Black Hole Coalescence,” *Phys. Rev. Lett.*, vol. 116, p. 241103, Jun 2016.
- [20] LIGO collaboration website <https://www.ligo.caltech.edu/image/>.
- [21] B. P. Abbott *et al.*, “GW170104: Observation of a 50-Solar-Mass Binary Black Hole Coalescence at Redshift 0.2,” *Physical Review Letters*, vol. 118, 1706.01812, p. 221101, June 2017.
- [22] B. P. Abbott *et al.*, “GW170608: Observation of a 19 Solar-mass Binary Black Hole Coalescence,” *Astrophysical Journal Letters*, vol. 851, 1711.05578, p. L35, Dec. 2017.
- [23] B. P. Abbott *et al.*, “GW170814: A Three-Detector Observation of Gravitational Waves from a Binary Black Hole Coalescence,” *Phys. Rev. Lett.*, vol. 119, p. 141101, Oct 2017.
- [24] B. P. Abbott *et al.*, “GW170817: Observation of Gravitational Waves from a Binary Neutron Star Inspiral,” *Phys. Rev. Lett.*, vol. 119, p. 161101, Oct 2017.
- [25] B. P. Abbott *et al.*, “GW170817: Measurements of neutron star radii and equation of state,” *ArXiv e-prints*, 1805.11581, May 2018.
- [26] B. P. Abbott *et al.*, “Upper Limits on the Rates of Binary Neutron Star and Neutron Star-Black Hole Mergers from Advanced LIGOs First Observing Run,” *Astrophysical Journal Letters*, vol. 832, 1607.07456, p. L21, Dec. 2016.
- [27] W. D. Arnett, J. N. Bahcall, R. P. Kirshner, and S. E. Woosley, “Supernova 1987A,” *Annual review of astronomy and astrophysics*, vol. 27, pp. 629–700, 1989.
- [28] B. P. Abbott *et al.*, “Multi-messenger Observations of a Binary Neutron Star Merger,” *Astrophysical Journal Letters*, vol. 848, 1710.05833, p. L12, Oct. 2017.
- [29] A. G. Riess, L. M. Macri, S. L. Hoffmann, D. Scolnic, S. Casertano, A. V. Filippenko, B. E. Tucker, M. J. Reid, D. O. Jones, J. M. Silverman, R. Chornock, P. Challis, W. Yuan, P. J. Brown, and R. J. Foley, “A 2.4% Determination of the Local Value of the Hubble Constant,” *Astrophysical Journal*, vol. 826, 1604.01424, p. 56, July 2016.
- [30] Planck Collaboration, “Planck intermediate results. XLVI. Reduction of large-scale systematic effects in HFI polarization maps and estimation of the reionization optical depth,” *Astronomy and Astrophysics*, vol. 596, 1605.02985, p. A107, Dec. 2016.
- [31] B. P. Abbott *et al.*, “Gravitational Waves and Gamma-Rays from a Binary Neutron Star Merger: GW170817 and GRB 170817A,” *Astrophysical Journal Letters*, vol. 848, 1710.05834, p. L13, Oct. 2017.
- [32] C. Freiburghaus, S. Rosswog, and F.-K. Thielemann, “r-process in neutron star mergers,” *Astrophysical Journal Letters*, vol. 525, no. 2, p. L121, 1999.
- [33] R. B. Larson, “The physics of star formation,” *Reports on Progress in Physics*, vol. 66, astro-ph/0306595, pp. 1651–1697, Oct. 2003.
- [34] A. H. Joy, “No. 709. T Tauri variable stars,” *Contributions from the Mount Wilson Observatory / Carnegie Institution of Washington*, vol. 709, pp. 1–28, 1945.
- [35] K. L. Luhman, “The Formation and Early Evolution of Low-Mass Stars and Brown Dwarfs,” *Annual Review of Astronomy and Astrophysics*, vol. 50, 1208.5800, pp. 65–106, Sept. 2012.
- [36] E. Hertzsprung, “Ueber die Verwendung photographischer effektiver Wellenlaengen zur Bestimmung von Farbaequivalenten,” *Publikationen des Astrophysikalischen Observatoriums zu Potsdam*, vol. 63, 1911.
- [37] E. E. Salpeter, “Nuclear reactions in the stars. i. proton-proton chain,” *Phys. Rev.*, vol. 88, pp. 547–553, Nov 1952.
- [38] M. Catelan, J. A. de Freitas Pacheco, and J. E. Horvath, “The Helium-Core Mass at the Helium Flash in Low-Mass Red Giant Stars: Observations and Theory,” *Astrophysical Journal*, vol. 461, astro-ph/9509062, p. 231, Apr. 1996.
- [39] D. Koester and G. Chanmugam, “Physics of white dwarf stars,” *Reports on Progress in Physics*, vol. 53, no. 7, p. 837, 1990.

- [40] S. Woosley and T. Janka, “The physics of core-collapse supernovae,” *Nature Physics*, vol. 1, astro-ph/0601261, pp. 147–154, Dec. 2005.
- [41] S. J. Smartt, “Progenitors of Core-Collapse Supernovae,” *Annual Review of Astronomy and Astrophysics*, vol. 47, 0908.0700, pp. 63–106, Sept. 2009.
- [42] D. L. Meier, R. I. Epstein, W. D. Arnett, and D. N. Schramm, “Magnetohydrodynamic phenomena in collapsing stellar cores,” *Astrophysical Journal*, vol. 204, pp. 869–878, Mar. 1976.
- [43] A. Burrows, E. Livne, L. Dessart, C. D. Ott, and J. Murphy, “Features of the Acoustic Mechanism of Core-Collapse Supernova Explosions,” *Astrophysical Journal*, vol. 655, astro-ph/0610175, pp. 416–433, Jan. 2007.
- [44] F. Daigne, *Objets compacts et phénomènes associés*. 2016.
- [45] W. Baade and F. Zwicky, “On Super-novae,” *Proceedings of the National Academy of Science*, vol. 20, pp. 254–259, May 1934.
- [46] J. R. Oppenheimer and G. M. Volkoff, “On massive neutron cores,” *Phys. Rev.*, vol. 55, pp. 374–381, Feb 1939.
- [47] S. K. Gupta, P. V. Ramana Murthy, B. V. Sreekantan, and S. C. Tonwar, “High-energy pulsed gamma rays from pulsars,” *Astrophysical Journal*, vol. 221, pp. 268–273, Apr. 1978.
- [48] S. L. Shapiro and S. A. Teukolsky, *Black holes, white dwarfs, and neutron stars: The physics of compact objects*. Wiley-Interscience, 1983.
- [49] C. Heinicke and F. W. Hehl, “Schwarzschild and Kerr solutions of Einstein’s field equation: An Introduction,” *International Journal of Modern Physics D*, vol. 24, 1503.02172, pp. 1530006–214, Dec. 2015.
- [50] E. Newman and T. Adamo, “Kerr-Newman metric,” *Scholarpedia*, vol. 9, 1410.6626, p. 31791, 2014.
- [51] V. Kalogera, K. Belczynski, C. Kim, R. O’Shaughnessy, and B. Willems, “Formation of double compact objects,” *Physics Reports*, vol. 442, astro-ph/0612144, pp. 75–108, Apr. 2007.
- [52] S. E. de Mink, M. Cantiello, N. Langer, and O. R. Pols, “Chemically Homogeneous Evolution in Massive Binaries,” vol. 1314 of *American Institute of Physics Conference Series*, pp. 291–296, Dec. 2010, 1010.2177.
- [53] S. E. de Mink and I. Mandel, “The chemically homogeneous evolutionary channel for binary black hole mergers: rates and properties of gravitational-wave events detectable by advanced LIGO,” *Monthly Notices of the Royal Astronomical Society*, vol. 460, 1603.02291, pp. 3545–3553, Aug. 2016.
- [54] T. M. Tauris and E. P. J. van den Heuvel, *Formation and evolution of compact stellar X-ray sources*, in *Compact stellar X-ray sources* (W. H. G. Lewin and M. van der Klis, eds.), pp. 623–665. Apr. 2006.
- [55] P. P. Eggleton, “Approximations to the radii of Roche lobes,” *Astrophysical Journal*, vol. 268, p. 368, May 1983.
- [56] P. A. Crowther, “Physical Properties of Wolf-Rayet Stars,” *Annual Review of Astronomy and Astrophysics*, vol. 45, astro-ph/0610356, pp. 177–219, Sept. 2007.
- [57] K. A. Postnov and L. R. Yungelson, “The Evolution of Compact Binary Star Systems,” *Living Reviews in Relativity*, vol. 17, 1403.4754, p. 3, May 2014.
- [58] K. S. Thorne and A. N. Zytow, “Stars with degenerate neutron cores. I - Structure of equilibrium models,” *Astrophysical Journal*, vol. 212, pp. 832–858, Mar. 1977.
- [59] J.-P. Zahn, “Circulation and turbulence in rotating stars,” *Astronomy and Astrophysics*, vol. 265, pp. 115–132, Nov. 1992.
- [60] I. Mandel and S. E. de Mink, “Merging binary black holes formed through chemically homogeneous evolution in short-period stellar binaries,” *Monthly Notices of the Royal Astronomical Society*, vol. 458, 1601.00007, pp. 2634–2647, May 2016.
- [61] P. Marchant, N. Langer, P. Podsiadlowski, T. M. Tauris, and T. J. Moriya, “A new route towards merging massive black holes,” *Astronomy and Astrophysics*, vol. 588, 1601.03718, p. A50, Apr. 2016.

- [62] L. Blanchet, “Gravitational Radiation from Post-Newtonian Sources and Inspiralling Compact Binaries,” *Living Reviews in Relativity*, vol. 17, 1310.1528, p. 2, Feb. 2014.
- [63] L. Lehner, “Numerical relativity: a review,” *Classical and Quantum Gravity*, vol. 18, gr-qc/0106072, pp. R25–R86, Sept. 2001.
- [64] K. D. Kokkotas and B. G. Schmidt, “Quasi-Normal Modes of Stars and Black Holes,” *Living Reviews in Relativity*, vol. 2, gr-qc/9909058, p. 2, Sept. 1999.
- [65] J. M. Bardeen and J. A. Petterson, “The Lense-Thirring Effect and Accretion Disks around Kerr Black Holes,” *Astrophysical Journal Letters*, vol. 195, p. L65, Jan. 1975.
- [66] P. C. Peters and J. Mathews, “Gravitational radiation from point masses in a keplerian orbit,” *Phys. Rev.*, vol. 131, pp. 435–440, Jul 1963.
- [67] M. C. Miller and D. P. Hamilton, “Four-Body Effects in Globular Cluster Black Hole Coalescence,” *Astrophysical Journal*, vol. 576, astro-ph/0202298, pp. 894–898, Sept. 2002.
- [68] E. B. Ford, B. Kozinsky, and F. A. Rasio, “Secular Evolution of Hierarchical Triple Star Systems,” *Astrophysical Journal*, vol. 535, pp. 385–401, May 2000.
- [69] L. Wen, “On the eccentricity distribution of coalescing black hole binaries driven by the kozai mechanism in globular clusters,” *Astrophysical Journal*, vol. 598, no. 1, p. 419, 2003.
- [70] F. Antonini, S. Toonen, and A. S. Hamers, “Binary Black Hole Mergers from Field Triples: Properties, Rates, and the Impact of Stellar Evolution,” *Astrophysical Journal*, vol. 841, 1703.06614, p. 77, June 2017.
- [71] F. Antonini and H. B. Perets, “Secular Evolution of Compact Binaries near Massive Black Holes: Gravitational Wave Sources and Other Exotica,” *Astrophysical Journal*, vol. 757, 1203.2938, p. 27, Sept. 2012.
- [72] M. P. Muno, E. Pfahl, F. K. Baganoff, W. N. Brandt, A. Ghez, J. Lu, and M. R. Morris, “An overabundance of transient X-ray binaries within 1 parsec of the galactic center,” *Astrophysical Journal Letters*, vol. 622, no. 2, p. L113, 2005.
- [73] R. M. O’Leary, B. Kocsis, and A. Loeb, “Gravitational waves from scattering of stellar-mass black holes in galactic nuclei,” *Monthly Notices of the Royal Astronomical Society*, vol. 395, 0807.2638, pp. 2127–2146, June 2009.
- [74] I. Bartos, B. Kocsis, Z. Haiman, and S. Márka, “Rapid and Bright Stellar-mass Binary Black Hole Mergers in Active Galactic Nuclei,” *The Astrophysical Journal*, vol. 835, 1602.03831, p. 165, Feb. 2017.
- [75] B. P. Abbott, R. Abbott, T. D. Abbott, M. R. Abernathy, F. Acernese, K. Ackley, C. Adams, T. Adams, P. Addesso, R. X. Adhikari, and et al., “Astrophysical Implications of the Binary Black-hole Merger GW150914,” *Astrophysical Journal Letters*, vol. 818, 1602.03846, p. L22, Feb. 2016.
- [76] V. Tiwari *et al.*, “Proposed search for the detection of gravitational waves from eccentric binary black holes,” *Physical Review D*, vol. 93, 1511.09240, p. 043007, Feb. 2016.
- [77] L. Barack *et al.*, “Black holes, gravitational waves and fundamental physics: a roadmap,” *ArXiv e-prints*, 1806.05195, June 2018.
- [78] C. L. Rodriguez, S. Chatterjee, and F. A. Rasio, “Binary black hole mergers from globular clusters: Masses, merger rates, and the impact of stellar evolution,” *Physical Review D*, vol. 93, 1602.02444, p. 084029, Apr. 2016.
- [79] P. C. Peters, “Gravitational radiation and the motion of two point masses,” *Phys. Rev.*, vol. 136, pp. B1224–B1232, Nov 1964.
- [80] B. Mikóczi, B. Kocsis, P. Forgács, and M. Vasúth, “Parameter estimation for inspiraling eccentric compact binaries including pericenter precession,” *Physical Review D*, vol. 86, 1206.5786, p. 104027, nov 2012.
- [81] E. Poisson and C. Will, *Gravity: Newtonian, Post-Newtonian, Relativistic*. Cambridge University Press, London, 2014.
- [82] N. Loutrel and N. Yunes, “Eccentric gravitational wave bursts in the post-Newtonian formalism,” *Classical and Quantum Gravity*, vol. 34, 1702.01818, p. 135011, July 2017.

- [83] K. Martel and E. Poisson, “Gravitational waves from eccentric compact binaries: Reduction in signal-to-noise ratio due to nonoptimal signal processing,” *Physical Review D*, vol. 60, gr-qc/9907006, p. 124008, Dec. 1999.
- [84] A. Buonanno, B. R. Iyer, E. Ochsner, Y. Pan, and B. S. Sathyaprakash, “Comparison of post-Newtonian templates for compact binary inspiral signals in gravitational-wave detectors,” *Physical Review D*, vol. 80, 0907.0700, p. 084043, Oct. 2009.
- [85] S. Tanay, M. Haney, and A. Gopakumar, “Frequency and time-domain inspiral templates for comparable mass compact binaries in eccentric orbits,” *Physical Review D*, vol. 93, 1602.03081, p. 064031, Mar. 2016.
- [86] R. A. Hulse and J. H. Taylor, “Discovery of a pulsar in a binary system,” *Astrophysical Journal*, vol. 195, pp. L51–L53, Jan. 1975.
- [87] T. Tenev and M. Horstemeyer, “The Mechanics of Spacetime - A Solid Mechanics Perspective on the Theory of General Relativity,” *ArXiv e-prints*, 1603.07655, Mar. 2016.
- [88] P. Weber, *General Relativity and Gravitational Waves*. Interscience Publishers Inc., New York, 1961.
- [89] M. E. Gertsenshtein and V. I. Pustovoit, “On the Detection of Low Frequency Gravitational Waves,” *Sov. Phys. JETP*, vol. 16, p. 433, 1962.
- [90] G. E. Moss, L. R. Miller, and R. L. Forward, “Photon-noise-limited laser transducer for gravitational antenna,” *Appl. Opt.*, vol. 10, pp. 2495–2498, Nov 1971.
- [91] R. Weiss, “Electromagnetically coupled broadband gravitational antenna,” *Quarterly Progress Report, Research Laboratory of Electronics*, vol. 105, p. 54, 1972.
- [92] C. Misner, K. Thorne, and J. Wheeler, *Gravitation*, W. H. Freeman, ed. Gravitation, 1973.
- [93] M. Pitkin, S. Reid, S. Rowan, and J. Hough, “Gravitational Wave Detection by Interferometry (Ground and Space),” *Living Reviews in Relativity*, vol. 14, 1102.3355, p. 5, July 2011.
- [94] D. M. Eardley, D. L. Lee, A. P. Lightman, R. V. Wagoner, and C. M. Will, “Gravitational-wave observations as a tool for testing relativistic gravity,” *Phys. Rev. Lett.*, vol. 30, pp. 884–886, Apr 1973.
- [95] B. P. Abbott, R. Abbott, R. Adhikari, P. Ajith, B. Allen, G. Allen, R. S. Amin, S. B. Anderson, W. G. Anderson, M. A. Arain, and et al., “LIGO: the Laser Interferometer Gravitational-Wave Observatory,” *Reports on Progress in Physics*, vol. 72, 0711.3041, p. 076901, July 2009.
- [96] T. Accadia, F. Acernese, M. Alshourbagy, P. Amico, F. Antonucci, S. Aoudia, N. Arnaud, C. Arnault, K. G. Arun, P. Astone, and et al., “Virgo: a laser interferometer to detect gravitational waves,” *Journal of Instrumentation*, vol. 7, p. 3012, Mar. 2012.
- [97] B. Willke *et al.*, “The GEO 600 gravitational wave detector,” *Classical and Quantum Gravity*, vol. 19, 03 2002.
- [98] M. Ando *et al.*, “Stable operation of a 300-m laser interferometer with sufficient sensitivity to detect gravitational-wave events within our galaxy,” *Phys. Rev. Lett.*, vol. 86, pp. 3950–3954, Apr 2001.
- [99] B. P. Abbott *et al.*, “Prospects for observing and localizing gravitational-wave transients with Advanced LIGO, Advanced Virgo and KAGRA,” *Living Reviews in Relativity*, vol. 21, p. 3, Apr. 2018.
- [100] J. Aasi *et al.*, “Advanced LIGO,” *Classical and Quantum Gravity*, vol. 32, 1411.4547, p. 074001, Apr. 2015.
- [101] F. Acernese *et al.*, “Advanced Virgo: a second-generation interferometric gravitational wave detector,” *Classical and Quantum Gravity*, vol. 32, 1408.3978, p. 024001, Jan. 2015.
- [102] C. S. Unnikrishnan, “IndIGO and Ligo-India Scope and Plans for Gravitational Wave Research and Precision Metrology in India,” *International Journal of Modern Physics D*, vol. 22, 1510.06059, p. 1341010, Jan. 2013.
- [103] K. Somiya, “Detector configuration of KAGRA-the Japanese cryogenic gravitational-wave detector,” *Classical and Quantum Gravity*, vol. 29, 1111.7185, p. 124007, June 2012.

- [104] Y. Aso, Y. Michimura, K. Somiya, M. Ando, O. Miyakawa, T. Sekiguchi, D. Tatsumi, and H. Yamamoto, “Interferometer design of the KAGRA gravitational wave detector,” *Physical Review D*, vol. 88, 1306.6747, p. 043007, Aug. 2013.
- [105] S. Goldwasser, “Wavelet graphs for the direct detection of Gravitational Waves,” Feb. 2017.
- [106] S. Konar, D. Mukherjee, D. Bhattacharya, and P. Sarkar, “Gravitational waves from surface inhomogeneities of neutron stars,” *Physical Review D*, vol. 94, 1610.08047, p. 104036, Nov. 2016.
- [107] B. Abbott *et al.*, “Upper limits on gravitational wave emission from 78 radio pulsars,” *Phys. Rev. D*, vol. 76, p. 042001, Aug 2007.
- [108] T. Regimbau and V. Mandic, “Astrophysical sources of a stochastic gravitational-wave background,” *Classical and Quantum Gravity*, vol. 25, 0806.2794, p. 184018, Sept. 2008.
- [109] C. Caprini, “Stochastic background of gravitational waves from cosmological sources,” in *Journal of Physics Conference Series*, vol. 610 of *Journal of Physics Conference Series*, p. 012004, May 2015, 1501.01174.
- [110] B. S. Sathyaprakash and B. F. Schutz, “Physics, Astrophysics and Cosmology with Gravitational Waves,” *Living Reviews in Relativity*, vol. 12, 0903.0338, p. 2, Mar. 2009.
- [111] E. F. D. Evangelista and J. C. N. de Araujo, “Stochastic background of gravitational waves generated by eccentric neutron star binaries,” *Monthly Notices of the Royal Astronomical Society*, vol. 449, 1504.02700, pp. 2700–2705, May 2015.
- [112] V. B. Ignatiev, A. G. Kuranov, K. A. Postnov, and M. E. Prokhorov, “Orbital Eccentricity Effects on the Stochastic Gravitational Wave Background from Coalescing Binary Neutron Stars,” *ArXiv Astrophysics e-prints*, astro-ph/0106569, June 2001.
- [113] M. Coughlin, P. Earle, J. Harms, S. Biscans, C. Buchanan, E. Coughlin, F. Donovan, J. Fee, H. Gabbard, M. Guy, N. Mukund, and M. Perry, “Limiting the effects of earthquakes on gravitational-wave interferometers,” *Classical and Quantum Gravity*, vol. 34, 1611.09812, p. 044004, Feb. 2017.
- [114] E. Thrane, N. Christensen, and R. M. S. Schofield, “Correlated magnetic noise in global networks of gravitational-wave detectors: Observations and implications,” *Physical Review D*, vol. 87, 1303.2613, p. 123009, June 2013.
- [115] S. A. Usman *et al.*, “The PyCBC search for gravitational waves from compact binary coalescence,” *Classical and Quantum Gravity*, vol. 33, 1508.02357, p. 215004, Nov. 2016.
- [116] S. Privitera, S. R. P. Mohapatra, P. Ajith, K. Cannon, N. Fotopoulos, M. A. Frei, C. Hanna, A. J. Weinstein, and J. T. Whelan, “Improving the sensitivity of a search for coalescing binary black holes with nonprecessing spins in gravitational wave data,” *Physical Review D*, vol. 89, 1310.5633, p. 024003, Jan. 2014.
- [117] B. Allen, “ χ^2 time-frequency discriminator for gravitational wave detection,” *Physical Review D*, vol. 71, gr-qc/0405045, p. 062001, Mar. 2005.
- [118] T. Damour, *The General Relativistic Two Body Problem and the Effective One Body Formalism*, in *General Relativity, Cosmology and Astrophysics* (J. Bičák and T. Ledvinka, eds.), p. 111. 2014.
- [119] I. W. Harry, B. Allen, and B. S. Sathyaprakash, “Stochastic template placement algorithm for gravitational wave data analysis,” *Physical Review D*, vol. 80, 0908.2090, p. 104014, Nov. 2009.
- [120] T. Dal Canton and I. W. Harry, “Designing a template bank to observe compact binary coalescences in Advanced LIGO’s second observing run,” *ArXiv e-prints*, 1705.01845, May 2017.
- [121] D. Sivia and J. Skilling, *Data analysis: A bayesian tutorial*. 2nd ed., June 2006.
- [122] S. Sharma, “Markov Chain Monte Carlo Methods for Bayesian Data Analysis in Astronomy,” *Annual Review of Astronomy and Astrophysics*, vol. 55, 1706.01629, pp. 213–259, Aug. 2017.
- [123] W. D. Vousden, W. M. Farr, and I. Mandel, “Dynamic temperature selection for parallel tempering in Markov chain Monte Carlo simulations,” *Monthly Notices of the Royal Astronomical Society*, vol. 455, 1501.05823, pp. 1919–1937, Jan. 2016.

- [124] D. E. Holz and S. A. Hughes, “Using Gravitational-Wave Standard Sirens,” *The Astrophysical Journal*, vol. 629, astro-ph/0504616, pp. 15–22, Aug. 2005.
- [125] B. P. Abbott, R. Abbott, T. D. Abbott, F. Acernese, K. Ackley, C. Adams, T. Adams, P. Addesso, R. X. Adhikari, V. B. Adya, and et al., “A gravitational-wave standard siren measurement of the Hubble constant,” *Nature*, vol. 551, 1710.05835, pp. 85–88, Nov. 2017.
- [126] H.-Y. Chen, D. E. Holz, J. Miller, M. Evans, S. Vitale, and J. Creighton, “Distance measures in gravitational-wave astrophysics and cosmology,” *ArXiv e-prints*, 1709.08079, Sept. 2017.
- [127] G. Dalya, G. Galgoczi, L. Dobos, Z. Frei, I. S. Heng, R. Macas, C. Messenger, P. Raffai, and R. S. de Souza, “GLADE: A Galaxy Catalogue for Multi-Messenger Searches in the Advanced Gravitational-Wave Detector Era,” *Monthly Notices of the Royal Astronomical Society*, vol. 479, 1804.05709, pp. 2374–2381, June 2018.
- [128] T. Kuroda, K. Kotake, K. Hayama, and T. Takiwaki, “Correlated signatures of gravitational-wave and neutrino emission in three-dimensional general-relativistic core-collapse supernova simulations,” *The Astrophysical Journal*, vol. 851, no. 1, p. 62, 2017.
- [129] H. Andresen, B. Müller, E. Müller, and H.-T. Janka, “Gravitational wave signals from 3D neutrino hydrodynamics simulations of core-collapse supernovae,” *Monthly Notices of the Royal Astronomical Society*, vol. 468, 1607.05199, pp. 2032–2051, June 2017.
- [130] D. Gabor, “Theory of communication. Part 1: The analysis of information,” *The Institution of Electrical Engineers*, pp. 429–441, Nov 1946.
- [131] S. Mallat, *A Wavelet Tour of Signal Processing, Third Edition: The Sparse Way*. Orlando, FL, USA: Academic Press, Inc., 3rd ed., 2008.
- [132] S. Klimenko, S. Mohanty, M. Rakhmanov, and G. Mitselmakher, “Constraint likelihood analysis for a network of gravitational wave detectors,” *Physical Review D*, vol. 72, gr-qc/0508068, p. 122002, Dec. 2005.
- [133] S. Klimenko, I. Yakushin, A. Mercer, and G. Mitselmakher, “A coherent method for detection of gravitational wave bursts,” *Classical and Quantum Gravity*, vol. 25, 0802.3232, p. 114029, June 2008.
- [134] S. Klimenko, G. Vedovato, M. Drago, F. Salemi, V. Tiwari, G. A. Prodi, C. Lazzaro, K. Ackley, S. Tiwari, C. F. Da Silva, and G. Mitselmakher, “Method for detection and reconstruction of gravitational wave transients with networks of advanced detectors,” *Physical Review D*, vol. 93, 1511.05999, p. 042004, Feb. 2016.
- [135] V. Nacula, S. Klimenko, and G. Mitselmakher, “Transient analysis with fast wilson-daubechies time-frequency transform,” *Journal of Physics: Conference Series*, vol. 363, no. 1, p. 012032, 2012.
- [136] I. Daubechies, S. Jaffard, and J.-L. Journe, “A simple Wilson orthonormal basis with exponential decay,” Mar 1990.
- [137] V. Connaughton *et al.*, “Fermi GBM Observations of LIGO Gravitational-wave Event GW150914,” *Astrophysical Journal Letters*, vol. 826, 1602.03920, p. L6, July 2016.
- [138] T. Damour, A. Gopakumar, and B. R. Iyer, “Phasing of gravitational waves from inspiralling eccentric binaries,” *Physical Review D*, vol. 70, gr-qc/0404128, p. 064028, Sept. 2004.
- [139] E. Chassande-Mottin, E. Lebigot, H. Magaldi, E. Chase, A. Pai, G. V, and G. Vedovato, “Wavelet graphs for the direct detection of gravitational waves,” *ArXiv e-prints*, 1710.09256, Oct. 2017.
- [140] I. T. Jolliffe and J. Cadima, “Principal component analysis: a review and recent developments,” *Philosophical Transactions of the Royal Society of London Series A*, vol. 374, p. 20150202, Apr. 2016.
- [141] R. Bellman, “The theory of dynamic programming,” *Bull. Amer. Math. Soc.*, vol. 60, pp. 503–515, 11 1954.
- [142] J. Powell, “Parameter estimation and model selection of gravitational wave signals contaminated by transient detector noise glitches,” *Classical and Quantum Gravity*, vol. 35, 1803.11346, p. 155017, Aug. 2018.

- [143] M. Zevin *et al.*, “Gravity Spy: integrating advanced LIGO detector characterization, machine learning, and citizen science,” *Classical and Quantum Gravity*, vol. 34, 1611.04596, p. 064003, Mar. 2017.
- [144] S. Bahaadini, V. Noroozi, N. Rohani, S. Coughlin, M. Zevin, J. Smith, V. Kalogera, and A. Katsaggelos, “Machine learning for gravity spy: Glitch classification and dataset,” *Information Sciences*, vol. 444, pp. 172–186, 5 2018.
- [145] E. Huerta, P. Kumar, S. T. McWilliams, R. O’Shaughnessy, and N. Yunes, “Accurate and efficient waveforms for compact binaries on eccentric orbits,” *Physical Review D*, vol. 90, p. 17, 08 2014.
- [146] E. A. Huerta, C. J. Moore, P. Kumar, D. George, A. J. K. Chua, R. Haas, E. Wessel, D. Johnson, D. Glennon, A. Rebei, A. M. Holgado, J. R. Gair, and H. P. Pfeiffer, “Eccentric, nonspinning, inspiral, Gaussian-process merger approximant for the detection and characterization of eccentric binary black hole mergers,” *Physical Review D*, vol. 97, 1711.06276, p. 024031, Jan. 2018.
- [147] I. Hinder, L. E. Kidder, and H. P. Pfeiffer, “An eccentric binary black hole inspiral-merger-ringdown gravitational waveform model from numerical relativity and post-Newtonian theory,” *ArXiv e-prints*, 1709.02007, Sept. 2017.
- [148] E. K. Porter and A. Sesana, “Eccentric Massive Black Hole Binaries in LISA I : The Detection Capabilities of Circular Templates,” *ArXiv e-prints*, 1005.5296, May 2010.
- [149] Z. Cao and W.-B. Han, “Waveform model for an eccentric binary black hole based on the effective-one-body-numerical-relativity formalism,” *Physical review D*, vol. 96, 1708.00166, p. 044028, Aug. 2017.
- [150] T. Hinderer and S. Babak, “Foundations of an effective-one-body model for coalescing binaries on eccentric orbits,” *Physical Review D*, vol. 96, 1707.08426, p. 104048, Nov. 2017.
- [151] I. Harry, J. C. Bustillo, and A. Nitz, “Searching for the full symphony of black hole binary mergers,” *Physical Review D*, vol. 97, 1709.09181, p. 023004, Jan. 2018.
- [152] M. Turner, “Gravitational radiation from point-masses in unbound orbits - Newtonian results,” *Astrophysical Journal*, vol. 216, pp. 610–619, Sept. 1977.
- [153] T. B. Littenberg, J. B. Kanner, N. J. Cornish, and M. Millhouse, “Enabling high confidence detections of gravitational-wave bursts,” *Physical Review D*, vol. 94, 1511.08752, p. 044050, Aug. 2016.
- [154] C. Moreno-Garrido, E. Mediavilla, and J. Buitrago, “Gravitational radiation from point masses in elliptical orbits: spectral analysis and orbital parameters,” *Monthly Notices of the Royal Astronomical Society*, vol. 274, pp. 115–126, May 1995.
- [155] H. Wang and B. Raj, “On the Origin of Deep Learning,” *ArXiv e-prints*, 1702.07800, Feb. 2017.
- [156] B. Müller, H.-T. Janka, and A. Heger, “New two-dimensional models of supernova explosions by the neutrino-heating mechanism: Evidence for different instability regimes in collapsing stellar cores,” *Astrophysical Journal*, vol. 761, no. 1, p. 72, 2012.
- [157] M. H. P. M. van Putten, “Proposed source of gravitational radiation from a torus around a black hole,” *Phys. Rev. Lett.*, vol. 87, p. 091101, Aug 2001.
- [158] M. Punturo *et al.*, “The Einstein telescope: a third-generation gravitational wave observatory,” *Classical and Quantum Gravity*, vol. 27, no. 19, 2010.
- [159] B. P. Abbott *et al.*, “Exploring the sensitivity of next generation gravitational wave detectors,” *Classical and Quantum Gravity*, vol. 34, 1607.08697, p. 044001, Feb. 2017.
- [160] P. Amaro-Seoane *et al.*, “Laser Interferometer Space Antenna,” *ArXiv e-prints*, 1702.00786, Feb. 2017.
- [161] M. Armano *et al.*, “Free-flight experiments in LISA Pathfinder,” in *Journal of Physics Conference Series*, vol. 610 of *Journal of Physics Conference Series*, p. 012006, May 2015, 1412.8384.
- [162] J. Ira Thorpe, C. Parvini, and J. Trigo-Rodriguez, “Detection and Characterization of Micrometeoroids with LISA Pathfinder,” *ArXiv e-prints*, 1510.06374, Oct. 2015.